AMERICAN UNIVERSITY OF BEIRUT

HIGH-RESOLUTION DYNAMIC DOWNSCALING TO ASSESS THE IMPACTS OF CLIMATE CHANGE IN REGIONS OF COMPLEX TOPOGRAPHY

by
RENALDA SAMIH EL-SAMRA

A dissertation
submitted in partial fulfillment of the requirements
for the degree of Doctor of Philosophy
to the Department of Civil and Environmental Engineering
of the Faculty of Engineering and Architecture
at the American University of Beirut

Beirut, Lebanon
August 2016

AMERICAN UNIVERSITY OF BEIRUT

HIGH-RESOLUTION DYNAMIC DOWNSCALING TO ASSESS THE IMPACTS OF CLIMATE CHANGE IN REGIONS OF COMPLEX TOPOGRAPHY

by
RENALDA SAMIH EL-SAMRA

Approved by:

_____
Dr. Mutasem El-Fadel, Professor   Advisor
Civil and Environmental Engineering, AUB

_____
Dr. Rami Zurayk, Professor   Committee Chair
Landscape Design & Ecosystem Management, AUB

_____
Dr. Majdi Abou Najm, Assistant Professor   Member of Committee
Civil and Environmental Engineering, AUB
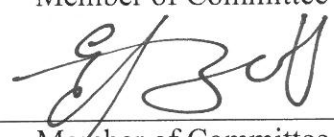
_____
Dr. Ibrahim Alameddine, Assistant Professor   Member of Committee
Civil and Environmental Engineering, AUB

_____
Dr. Jad Chaaban, Associate Professor   Member of Committee
Agriculture, AUB

_____
Dr. Elie Bou-Zeid, Associate Professor   Member of Committee
Civil and Environmental Engineering, Princeton University, USA (External)

_____
Dr. Georgiy Stenchikov, Professor   Member of Committee
Earth Sciences and Engineering Program, KAUST, KSA (External)

Date of dissertation defense: August 26, 2016

AMERICAN UNIVERSITY OF BEIRUT

THESIS, DISSERTATION, PROJECT RELEASE FORM

Student Name:
El-Samra   Renalda   Samih
_____   _____   _____
 Last   First   Middle

◯ Master's Thesis   ◯ Master's Project   ⊗ Doctoral Dissertation

☐   I authorize the American University of Beirut to: (a) reproduce hard or electronic copies of my thesis, dissertation, or project; (b) include such copies in the archives and digital repositories of the University; and (c) make freely available such copies to third parties for research or educational purposes.

☑   I authorize the American University of Beirut, to: (a) reproduce hard or electronic copies of it; (b) include such copies in the archives and digital repositories of the University; and (c) make freely available such copies to third parties for research or educational purposes after:

  One ---- year from the date of submission of my thesis, dissertation, or project.
  Two ---- years from the date of submission of my thesis, dissertation, or project.
  Three -- X -- years from the date of submission of my thesis, dissertation, or project.

_____

Signature   Date

This form is signed when submitting the thesis, dissertation, or project to the University Libraries

ACKNOWLEDGEMENTS

There are many people to thank for helping me through this process in one way or another. First, I would like to express my sincere gratitude to my advisor, Professor Mutassem El-Fadel, for the opportunity to pursue this research, and for his insights, support, patience and encouragements during the course of this work. I am very honored that I had the chance to work with him. I am equally indebted with gratitude to Dr. Elie Bou-Zeid, who was my mentor during the semester I spent at Princeton University, and for his diligent guidance and helpful comments ever since, and throughout my research. Through both Professor El-Fadel and Dr. Bou-Zeid, I have become a better writer, researcher, and learner.

I would like to thank my Ph.D. committee members, Professor Rami Zurayk for guiding me patiently through the agricultural aspects of my research, Professor Georgiy Stenchikov for his assistance through the many Skype calls, Dr. Majdi Abou Najm, Dr. Ibrahim Alameddine, and Dr. Jad Chaaban, for their constructive suggestions. I would like to thank Dr. Dan Li for teaching me how to use WRF, Dr. Young-Hee Ryu, Dr. Mary Lynn Baeck and Xiaofeng Hu for their technical support. A special thanks goes to Hamza Kunhu Bangalath at KAUST for his collaboration.

I would like to thank my late parents, who I lost during this work. My parents have always believed in me and gave me positive encouragement throughout my life. Their presence is terribly missed.

I am forever endebted to my very dear friend George Khalil for his unconditional support and tremendous sacrifice. Without him, I would have never made it through this endeavor.

Finally, I would like to thank my sister Rita, and all my friends for being my greatest support system especially Dr. Rania Maroun, Najate Mawad, Randa Makarem and Jocelyne Abi Aoun.

AN ABSTRACT OF THE DISSERTATION OF

Renalda Samih El-Samra   for   Doctor of Philosophy
                                Major: Environmental and Water Resources Engineering

Title: High-resolution dynamic downscaling to assess the impacts of climate change in regions of complex topography

High resolution dynamical downscalling is conducted for the past and the near future (untill 2050) climates under two Representative Concentration Pathways (RCP4.5 and RCP8.5) over a complex topographical terrain along the eastern Mediterranean, with a focus on Lebanon, using the Weather Research and Forecast (WRF) model forced by the High-Resolution Atmospheric Model (HiRAM). For this purpose, WRF performance for the study area was first evaluated by sequentially downscaling Global Forecast System (GFS) Reanalysis (resolution 1°) model results, for a mild and wet year and a hot and dry year, to three local horizontal resolutions of 9, 3 and 1 km. Simulated near-surface hydrometeorological variables were compared at different time scales against data from an observational network over the study area. The overall performance of WRF at 1 and 3 km horizontal resolution was very satisfactory, with significant improvement over the 9 km downscaling simulation. The findings therefore indicated that a 3km resolution is sufficient for the downscaling, especially that it would allow more years and scenarios to be investigated compared to the higher 1km resolution at the same computational effort.

Then, a set of ten downscaling simulations at 3 km resolution were performed using WRF driven with HiRAM, to generate future climate projections of annual and seasonal temperature and precipitation changes over Lebanon. Two past years (2003 and 2008), were simulated to evaluate the model and to serve as a baseline scenario. The downscaled data were in the range of recent observed climatic variability, and therefore corrected for the cold bias of HiRAM. Eight future years were then selected based on an anomaly score that relies on the mean annual temperature and accumulated precipitation to identify the worst year per decade from a water resources perspective. One year per decade, from 2011 to 2050, and per RCP was simulated. The results indicated that by the middle of the century, the study area might be exposed to a significant decrease in annual precipitation (rain and snow), reaching up to 30% relative to the current condition. The seasonal variability is forecasted to increase significantly, with colder winter and warmer summer conditions, and with notable increases in the annual occurrence of hot nights and heat wave events.

The simulations results were finally used as weather input to a soil-plant growth simulator (CropSyst) to characterize silage maize agricultural yield and water balance in a pilot area located in the semi-arid central inland region. Outcomes advised that the net effects of increasing atmospheric CO_2 and climate change would lower crop yields if existing management practices were not adjusted. Adaptation strategies were proposed and the most effective approach was earlier sowing by selecting the planting date based on seasonal forecasting. The selected dates ensure the absence of frost

temperatures and the occurrence of the baseline cutoff temperature of 10°C necessary for silage maize sowing. As a result, yield improvement was on the average 3% and 5% under RCP4.5 and RCP8.5 respectively, in comparison with 2008 baseline scenario. Other adaptation measures can be to adopt higher-yielding and heat resistant cultivars or sowing other plants that uses less water such as Sorghum and Millet and improve water conservation techniques.

CONTENTS

ILLUSTRATIONS

xiii

xiv

TABLES

ABBREVIATIONS

AM	Atmospheric Model
AREC	Advancing Research, Enabling Communities Center
AUB	American University of Beirut
BIA	Beirut International Airport
BIAS	Bias of the mean
CCM4	Community Climate System Model 4
CDD	Consecutive Dry Days
CDO	Climate Data Operators
CFD	Consecutive Frost Days
CI	Central Inland
CM	Central Mountain
CMIP5	Coupled Model Intercomparison Project phase 5
CO_2	Carbon Dioxide
COVAR	Covariance or Dispersion Error
CRM	Residual Mass Coefficient
CS	Central Coast
CSU	Consecutive Summer Days
CWD	Consecutive Wet Days
DJF	December, January and February
ET_0	Reference Evapotranspiration
ETCCDI	Expert Team on Climate Change Detection and Indices
FD	Frost Days

FNL	Final Analysis
GCM	Global Climate Model
GDD	Growing Degree Days
GFDL	Geophysical Fluid Dynamics Laboratory
GFS	Global Forecast System
GHG	Greenhouse Gas
HadGEM2-AO	Hadley Global Environment Model 2 –Atmosphere-Ocean
HAO	Haouch Al Omara
HD	Heating Degree Days
HiRAM	High Resolution Atmospheric Model
HWDI	Heat Wave Duration Index
HWFI	Heat Wave Frequency Index
IC	Initial Condition
INM-CM4	Institute for Numerical Mathematics Climate model 4
JJA	June, July and August
LARI	Lebanese Agricultural Research Institute
LBCs	Lateral Boundary Conditions
LM	Land Model
LNMS	Lebanese National Meteorological Services
LWP	Longest Wet Period
LW/SW	Long Wave and Short Wave
MAE	Mean Absolute Error
MBE	Mean Bias Error
MI	Maximum Rainfall Intensity

MJJA	May, June, July and August
MODIS	Moderate Resolution Imaging Spectroradiometer
MRI-CGCM3	Meteorological Research Institute-Global Climate Model 3
MYJ	Mellor-Yamada Janjic
NC	Northern Coast
NCAR	National Center for Atmospheric Research
NCEP	National Center for Enviromental Prediction
NI	Northern Inland
NM	Northern Mountain
NOAA	National Oceanic and Atmospheric Administration
NRD	Number of Rainy Days
PBIAS	Percentage Bias
PDF	Probability Density Function
PBL	Planetary Boundary Layer
R2	Coefficient of Determination
R10MM	Days of Heavy Rainfall
R20MM	Days of very Heavy Rainfall
RCM	Regional Climate Model
RCP	Representative Concentration Pathway
RMSE	Root Mean Square Error
RRTM	Rapid Radiative Transfer Model
RX1DAY	Maximum One Day Precipitation
SC	Southern Coast
SI	Southern Inland

SST	Sea Surface Temperature
SU	Summer Days
Tavg	Average Temperature
Tmax	Maximum Temperature
Tmin	Minimum Temperature
TN90p	Occurrence of warm nights
TX90p	Occurrence of warm days
TRP	Tripoli
USGS	United States Geological Survey
VAR	Variance or Standard Deviation
WI	Willmott Index of Agreement
WPS	WRF Preprocessing System
WRF	Weather Research and Forecast
WSM6	Single-Moment 6-Class Microphysics Scheme
YSU	Yonsei University

In memory of my late beloved parents
Samih and Clemence

CHAPTER 1

INTRODUCTION

1.1   Background

Weather and climate have significant societal, ecological, and economic impacts across all regions of the world (Easterling *et al*., 2000). Since the last century, increased greenhouse gases have caused many changes in the weather and climate. Of particular concern are increased occurences of heatwaves, floods, heavy precipitation events and droughts, that have led to the highest socio-economic impacts worldwide (Alexandratos and Bruinsma, 2012; Ahn *et al*., 2015). The importance of understanding these events is evident in a stationary climate, but the need becomes more pressing under climate change because of the additional stress that comes with finding the most suitable adaptation strategies at a local scale that can be used to guide policy and management decisions (Taplin, 2012).

The Middle East region, with most of its countries dominated by arid and semi-arid lands, is expected to experience a decrease in winter precipitation and an increase in temperature by the end of the 21th century (Giorgi *et al.*, 2001; Alpert *et al*., 2008; Kitoh *et al*., 2008; Evans, 2009; Sanchez-Gomez *et al*., 2009; El-Fadel, 2010; El-Fadel *et al.,* 2012). The resultant reduction in available water is likely to have adverse consequences for the people of the region—many of whom already live in conditions of water scarcity. The combination of a stressed fresh water resources and rapid population growth substantially increases the vulnerability of the region to future climate change (Evans, 2009).

Since the beginning of the century, many research projects analyzed and focused on global and regional climate simulations over the Mediterranean region (Bou-Zeid and El-Fadel, 2002; Weiss *et al.*, 2007; Giorgi and Lionello, 2008; Black *et al.*, 2010). Simulating the climate of the basin is a challenge for climate models (Evans *et al.*, 2004), due to the high natural inter-annual variability, the complex topography of the region which includes multiple mountain ranges and inland waters, and proximity to the Mediterranean Sea (Black *et al.*, 2010). While these simulations often capture the global-scale processes and trends well, their spatial resolution is too coarse to capture mesoscale and local systems that are important for regional climate. Recent improvements in model simulations relied on higher resolution in a few locations in the Mediterranean basin (Lebeaupin-Brossier *et al.*, 2011; Givati *et al.*, 2012); however these locations remain sparse. In this context, vulnerability assessment to climate change constitutes the cornerstone of current research needs in the region particularly at a downscaled level from global circulation models (GCMs), which tend to have a relatively large resolution that prevents them from capturing local impacts accurately.

This research aims to fill this gap in fine-scale climate change impact and adpatation information, and targets the country of Lebanon, located in the eastern Meditteranean basin. Particular emphasis is placed on two sectors: water and agriculture, with with an aim to assess the impacts and reduce the country's vulnerability and strengthen its adaptive capacity. Vulnerability assessments in Lebanon are mostly part of national communications to the United Nations Framework Convention on Climate Change (Lebanon FNC, 1999 and SNC, 2011) in which attempts for downscaling climate simulations generated by GCMs to regional levels have been initiated or are in the planning process. However, evaluation of downscaling

methods revealed significant limitations mainly due to the inability of GCMs to capture small scale events, thus calling for alternative methods.

1.2   Research Objectives

The proposed research targets the following objectives:

1.   Dynamically downscale global climate predictions to a local scale using the Weather Research and Forecasting (WRF) model (Skamarock *et al*., 2008) forced by High Resolution Atmospheric Model (HiRAM) (Zhao *et al*., 2009a) for the past and the future. The simulations provided information on the spatial variability of vulnerability that was absent from climate simulations such as the areas that will be mostly affected by drought during future extreme dry years.

2.   Analyze silage maize agricultural yield and irrigation water demand in a pilot area based on climate simulations using the Soil-Water-Vegetation Cropping Systems Simulation (CropSyst) Model (Stöckle *et al.*, 1994). This pilot area is the Agriculture Research and Education Center (AREC) of the American University of Beirut (AUB). Future climate predictions were relied upon to define the probability of occurrence of adverse hydro-meteorological and climatic conditions that resulted in poor agricultural yields and irrigation deficits, and how this probability changed as the larger climatic patterns are altered. In practical terms, the analysis allowed us to determine if a X % reduction in rainfall and/or a Y ℃ increase in air temperature (observed during a given year) were acceptable or catastrophic for agricultural production. As a result, different adaptive managements strategies were investigated and assessed in order to advise on the most convenient adaptation measure for the specific pilot area condition.

1.3　Research Innovation

While research on global and regional climate simulations have been conducted in the Mediterranean basin, studies addressing dynamic downscaling of global climate simulations for Lebanon are inexistent. The proposed research is innovative because it is the first to use high resolution (3km) WRF model to dynamically downscale HiRAM model over Lebanon for the past (year 2003 and 2008) and for the future (from 2011-2050) under two Representative Concentration Pathways (RCP) 4.5 and 8.5. It is the first time WRF is forced by HiRAM and for this purpose a generic data conversion method was developed. Moreover, the inner domain grid size (3 km) used in the simulations (covering Lebanon) is significant and computationally intensive, but the high computational effort for this region is justified since this country contains a large population that may be affected by climate change. The high resolution is also needed given the complex topography of the region; in that regard, a primary innovation of the thesis was the evaluation of the significant increased forecasting skill that higher resolution models allow over complex terrain, relative to global models. In addition, this study will be the first to use the output of WRF climate simulations to parameterize CropSyst in order to define the possible changes in crop yield in the project area in order to define suitable adapatation strategies.

1.4　Dissertation structure

The dissertation consists of seven chapters that can be grouped into three parts besides the introduction (Chapter 1) and the conclusion (Chapter 7). The first part, consisting of Chapters 2 and 3, presents the evaluation of WRF model driven by the Global Forecast System (GFS) Reanalysis (resolution 1°) for the past baseline

conditions (a wet and cold year, along with a dry and hot year) and the selection of the most appropriate model resolution to be used for the future simulations. The second part consists of Chapters 4 and 5 where a set of ten downscaling simulations at high spatial resolution (3 km horizontally) were performed using WRF, using the model set-up established in Chapters 2 and 3, to generate future climate projections of annual and seasonal temperature and precipitation changes over Lebanon. In these simulations, WRF was forced with the High Resolution Atmospheric Model (HiRAM), running over the whole globe at a resolution of 25 km, under the conditions of two RCPs (4.5 and 8.5). Two past years (2003 and 2008) were simulated to evaluate the model and to serve as a baseline scenario, and eight future years with particularly adverse conditions were selected, one year per decade per scenario from 2011 to 2050, and simulated to quantify the changes. The third part is presented in Chapter 6, and it focuses on the potential impacts of climate change on silage maize agricultural yield in a pilot area in the central inland region using Cropsyst model along with WRF simulations outputs from Chapters 4 and 5.

CHAPTER 2

WHAT MODEL RESOLUTION IS REQUIRED IN CLIMATOLOGICAL DOWNSCALING OVER A COMPLEX TERRAIN?

2.1   Introduction

The climate is warming due to increased radiative forcing produced by anthropogenic emissions of greenhouse gases (GHGs). Regardless of the future emission scenario adopted, this warming is likely to exacerbate water scarcity in many regions of the world and lead to various other adverse impacts on human socio-economic activities and well-being. Since preparing for these variations is the wise course of action, an understanding of climate change impacts at small temporal and spatial scales is imperative to guide policy and management decisions. This motive fuelled a dramatic progress in weather forecasting and climate modelling over the past 50 years, involving a multidisciplinary top-down approach whereby an emission scenario is postulated to force a Global Climate Model (GCM) simulation, also known as General Circulation Model, which is then downscaled using dynamical (via a Regional Climate Model (RCM)) or statistical methods (Lynch, 2008; Quintana Seguí *et al.*, 2010). While GCMs simulate several facets of the climate system and corresponding interactions (Murphy *et al*., 2004), they are constrained by computational limitations to horizontal grid spacing on the order of hundreds of kilometers. This coarse resolution produces serious truncation errors in the numerical solution of the governing differential equations (Lynch, 2008). Other factors that downgrade the results of GCMs include processes that are not explicitly simulated at these resolutions, like

convection, clouds and precipitation, heterogeneity of surface fluxes, and planetary

boundary layer (PBL) turbulence. These subgrid-scale processes are "parameterized"

instead, using a physical understanding of the underlying physics, or semi-empirical

relations (Giorgi and Mearns, 1991). Hence, the coarse grids of GCMs preclude the

accurate representation of a range of processes that are important to the

hydrometeorological projections used in climate-change impact studies at the regional

to local levels. Examples of these projections are extreme weather events (floods,

droughts, heat waves) that have significantly influenced the global community in the

last decade. In 2015, 10 weather and climate catastrophic events occurred with damages

exceeding $1 billion each in the United States alone (NCDC, 2016). More than 30,000

deaths were attributed to the 2003 European heat wave (Robine *et al.*, 2008), while

nearly 55,000 deaths were caused by the Russian heat wave in 2010 (Katsafados *et al.*,

2013). Since these extremes are of utmost importance when climate change impacts are

being assessed, coarse resolution GCM results are downscaled by RCMs to (1) add high

resolution element to resolve regional scale constraints (e.g. topography, coastal lines,

and land use/land cover) that interact with the larger-scale atmospheric circulations

(Giorgi, 2006), and (2) resolve some small scale processes that are parameterized in

GCMs (such as convection). Downscaling using RCMs, referred to as dynamical

downscaling, has been reported to represent regional climate characteristics more

accurately than GCM simulations (Giorgi and Mearns, 1991; Wang *et al*., 2004;

Argüeso *et al*., 2012; Berg *et al*., 2013, Mohan and Sati, 2016), and therefore is more

reliable to force impact models (for example, crop and hydrological models) and

develop adaptation and mitigation strategies. However, various gaps remain in our

understanding of the forecasting skill and optimal setup of such downscaling

simulations, especially over complex terrain (Salameh *et al.*, 2009; Di Luca *et al.*, 2015). Two particularly critical open questions are: What model resolution is required in climatological downscaling over a complex terrain? And how does the downscaling skill vary among the main hydrometeorological variables of interest: temperature, precipitation, and wind speed?

In this chapter, we aim to address these questions using the Weather Research and Forecasting (WRF) model during a hot and dry year, which represents the most adverse conditions under future climate change scenarios, as well as a mild and wet year. While the performance of the WRF model as a regional climate model has been widely tested (see Appendix A), assessments of its skill in hydrometeorological downscaling during extreme years and over a complex terrain remain very limited and insufficient to answer our motivating questions. However, establishing this skill is needed to support downscaling simulations for future years.

2.2   Data and Methods

2.2.1   *Model Domain: Pilot Study Area*

The country of Lebanon, which is located in the northern temperate zone along the eastern Mediterranean (Fig. 2.1a), represents a compelling example of the need for high-resolution climatology due to its geomorphological complexity as well as large climate gradients (Fig. 2.1b). It was selected as the testing domain, with several observational stations (Fig. 2.1c) for validation.
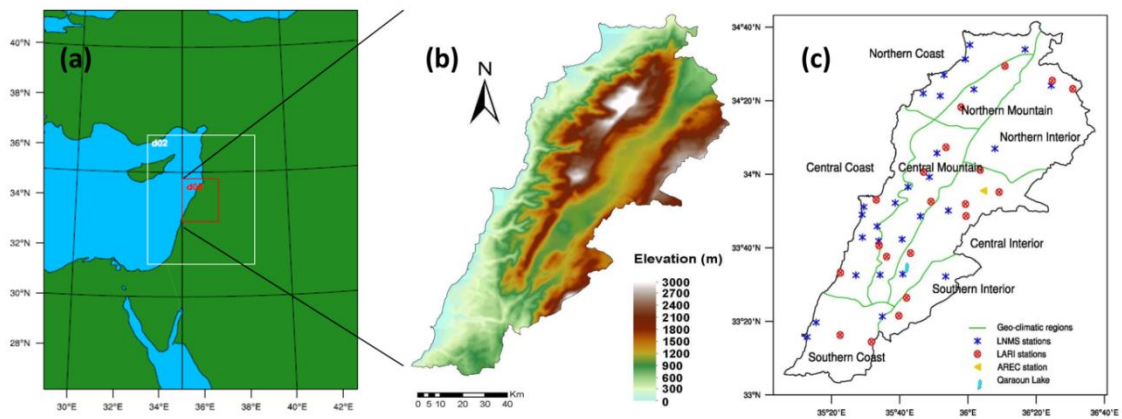
Fig. 2.1. (a) Eastern Mediterranean basin showing WRF's 3 domains (9:3:1 km) configuration, (b) topographic features of the study area, (c) smallest WRF domain d03 (1 km) configuration depicting the observational stations with available data for 2003 and 2010 by geo-climatic region (43 rain, 2 wind and 31 temperature stations with records of both daily average and/or daily maximum and minimum temperatures)

2.2.2   Model Description

The Weather Research and Forecasting (WRF) is a three-dimensional mesoscale meteorology model, which is suitable for operational forecasting and atmospheric research needs (Heikkilä *et al*., 2011). It has a wide range of options for parameterizing physical processes, as well as various schemes for the numerical discretization of the governing equations (Skamarock *et al*., 2008). The model can directly extract, from several databases, information and data on terrain elevation, land cover and land use from the United States Geological Survey (USGS) and the Moderate Resolution Imaging Spectroradiometer (MODIS) (Friedl *et al*., 2001) at various resolutions that cover the entire globe. The finest resolution of these global data is 30 seconds in both latitudinal and longitudinal directions, which corresponds to about 1 km in length at mid-latitudes.

2.2.3 Model Configuration

A regional high resolution is achieved in the current simulations by using three one-way nested domains (Fig. 2.1a), with 9, 3 and 1km horizontal resolutions. The outer integration domain covers 1350 km × 1700km to guarantee that synoptic-to-mesoscale systems that affect the coast are resolved in WRF. The inner domain extends over 154 km×193km (Fig. 2.1c), covering the entire study area. MODIS (2001) (Friedl *et al.*, 2001) land use data was adopted with 21 land categories and Lambert Conformal projection, which is the most convenient for mid-latitude regions and provides homogeneous grid spacing, unlike latitude-longitude coordinates. A 30 seconds time step was used for the smallest domain. For the base cases, all domains had 35 vertical levels (with a vertically-stretched grid) arranged according to terrain-following hydrostatic pressure coordinates.

The National Center for Atmospheric Research-National Center for Environmental Prediction Final Analysis Data (NCAR/NCEP, 2000), which are global atmospheric fields with a 1-degree resolution and 26 pressure levels (1000-10hPa), were used for initial, and boundary conditions. The time interval of the boundary data is 6 hours, while the sea surface temperature (SST) was updated once monthly. No nudging was adopted during the simulation to avoid biasing the validation (since in future downscaling, nudging data are not available) by "pulling" the model towards the observed conditions, and making it difficult to assess whether WRF can describe features like air-mass formation that build within the domain (Paimazumder *et al.*, 2012). All the WRF one month-simulations were initialized on the first of each month of years 2003 and 2010 to prevent the regional model from drifting far from the observed weather by reinitializing it from the driving reanalysis data on a monthly basis.

This method has the additional benefit of allowing simultaneous simulations for several months, significantly reducing the wall-clock simulation time (Pan *et al*., 1999; Caldwell *et al*., 2009). The best practice for model spin up under such conditions is still debated (Pan *et al*., 1999; Ferreira *et al*., 2014): spin up could under various conditions produce surface states that have more discrepancies compared to actual states if the modeling system does not assimilate observed data while the initialization product does. In this study, we opted not to include spin-up periods in the monthly simulations because (i) the NCAR/NCEP (2000) surface initialization contains data assimilation for soil moisture and temperature and spin up is not required to set the surface state, (ii) analyses of various spinup periods generally show that they have a limited impact on meteorological fields (Ryu *et al*., 2016), and (iii) the effect of spin up would only affect the first few days of our monethly runs and will thus have a limited impact on the model evaluation we presente later.

While the year 2010 was a relatively hot and dry year that is used here as an example of an extreme period, we also compare the modeling results to a mild and wet year, 2003. The years 2003 and 2010 were selected precisely to have extreme hydrometeorological events such as heat waves, strong storms, or drought periods that pose particular challenges in dynamic modeling. The selection was based on continuous daily data spanning the period from 2001 till 2010. WRF simulations of historically wet and dry years also allow "measuring" the sensitivity of complex topographical regions to climate extremes, which are good proxies for the conditions expected in the future as the climate means shift.

The parameterization schemes adopted include the Single-Moment 6-Class Microphysics Scheme (WSM6) (Hong and Lim, 2006), Monin-Obukhov and Mellor-

Yamada Janjic (Eta) for surface layer and PBL physics (Mellor and Yamada, 1974; Janjic, 2001) (we also evaluated the YSU scheme, as we will detail later), Dudhia Long Wave and Short Wave (LW/SW) for radiative processes (Dudhia, 1989), Rapid Radiative Transfer Model (RRTM) (Mlawer *et al*., 1997) and the Noah Land Surface Model for surface processes (Chen and Dudhia, 2001). The choices are motivated by previous WRF tests detailed in Talbot *et al*. (2012) and Li *et al*. (2013), and various other studies that examined the influence of the choice of parameterizations on WRF's performance (Bukovsky and Karoly, 2009; Ruiz *et al*., 2010; Argüeso *et al*., 2011; Remesan *et al*., 2015).

2.2.4   *Observational Data*

The duration, quality, and exhaustiveness of several climatic data sources (Atlas Climatique du Liban; NOAA's National Climatic Data Center, Lebanese National Meteorological Services (LNMS), Lebanese Agricultural Research Institute (LARI), American University of Beirut Advancing Research Enabling Communities Center (AREC)) were assessed to identify the spatial and temporal climatic data that can be relied upon. Based on long-term trends of weather parameters including temperature, relative humidity, precipitation, and wind, the Lebanese National Meteorological Services (LNMS) divides the study area into three broad climatic regions: the coastal, the mountainous and the inland. These are further subdivided into sub-regions making up a total of eight geoclimatic regions (Fig. 2.1c):

- The coastal strip, which includes the northern (NC), central (CS) and southern coasts (SC);

- The mountainous area, which is divided into the northern (NM) and central mountains (CM);

- The inland region, which is divided into the northern (NI), central (CI) and southern (SI) areas.

The analysis of climatic records from weather stations in the study area (Fig. 2.1c) indicated variation in span and quality. The availability of continuous observations was a hindrance since we could get complete daily data for a limited number of stations for the various geoclimatic regions. We selected only the stations from which 70% or more of the daily and/or monthly precipitation, temperature and wind measurements were available during 2003 and/or 2010 (see Appendix B), which required the exclusion from WRF's output analysis of the periods with missing data for each selected station before model evaluation statistics were carried out. Comparisons between simulated and observed 2m temperatures, precipitation, and 10m wind, were then performed to answer the driving question of this chapter.

2.2.5   *Data Handling and Analysis*

Model simulations from WRF in its three resolutions (9, 3 and 1km) were compared with observations at various stations throughout the inner domain. While model validation is imperative, there is no agreement on an ideal evaluation technique. Traditionally, RCMs evaluation procedures rely on gridded data or reanalysis (Argüeso *et al*., 2011; Berg *et al*., 2013). However, these datasets are sometimes created using a rather small number of stations, and the resulting interpolation can lead to excessively smoothed precipitation and temperature values that do not capture the extremes (Hofstra *et al*., 2009).

In this chapter, several statistics were used to evaluate model performance using observational datasets such as the mean bias error (MBE), mean absolute error (MAE), percentage bias (PBIAS), root mean square error (RMSE), percentage RMSE, and coefficient of determination R2 (Willmott, 1982; Kobayashi and Salam, 2000). Assessment of the contribution to the RMSE of (i) the bias of the mean (referred to as BIAS), (ii) the variance or standard deviation (referred to as VAR) and (iii) the covariance or dispersion error (referred to as COVAR) are also conducted following the approaches of Murphy (1988) and Horvath *et al*. (2012) as expressed in equations 1a and 1b:.

$$MSE = \frac{1}{MN} \sum_{k=1}^{M} \sum_{i=1}^{N} (x_{i,k} - y_{i,k})^2 \qquad (1a)$$

$$MSE = \frac{1}{M} \sum_{k=1}^{M} (\bar{x}_k - \bar{y}_k)^2 + [\sigma_k(x) - \sigma_k(y)]^2 + 2\sigma_k(x)\sigma_k(y)[1 - r_k(x,y)] \qquad (1b)$$

where MSE is the mean square error, x and y are respectively the simulated and observed data, k and i are indices denoting various points in space and time, M is the number of stations per geo-climatic region, N is the number of points in the time series being compared, σ is the standard deviation, r is the correlation coefficient between simulated and observed data, and bars indicate time-averages. In this equation, the first term on the right hand side is the BIAS that denotes errors related to differences in the means between observations and model outputs, the second is the VAR that reflects errors resulting from the differences in variability between the two, while the third is the COVAR that is related to the synchronization errors between observation and simulated time series.

A regional statistical analysis was performed on the limited number of stations corresponding to every geo-climatic zone. Depiction of extreme events is through the probability density functions (PDFs) of the temperature and precipitation. Comparisons concentrated on daily average, maximum and minimum temperatures (Tavg, Tmax and Tmin) and accumulated total precipitation (daily, monthly and yearly). The daily average, maximum and minimum statistics are derived from the WRF simulations (hourly data) to assess the value of WRF downscaling. The simulated values are taken at the center of the grid cell for temperature and precipitation. Interpolation to match the exact observational location would result in minor differences in the simulated values derived from the smallest grids (WRF 1km and 3km), which are the focus of this study. For the same reason, no lapse rate correction was applied to temperature at the fine grid resolutions. Furthermore, since the lapse rate over complex topographical terrain does not depend only on altitude but is also a function of other aspects such as buoyancy, mountain width, moisture (Barstad and Smith, 2005) and wind (Esteban and Chen, 2008), estimating an altitude correction confidently is challenging. The use of a uniform and constant lapse rate of 6–6.5°C/km is reportedly not illustrative of real surface environments over complex topographic terrains based on the use of temperature sensors (Bolstad *et al*., 1998; Rolland, 2003; Tang and Fang, 2006; Blandford *et al*., 2008; Gardner *et al*., 2009; Minder *et al*., 2010). Such observational studies report that the average surface lapse rate varies considerably from the 6–6.5°C/km values often used to correct for altitude discrepancies between grid centers and observational points, displaying noticeable seasonal changes beyond 2°C/km, diurnal erraticism and spatial fluctuations linked to the topography or position with respect to valleys (Minder *et al*., 2010). In light of the above, we opted not to apply a lapse rate correction to the 9km

15

domain either since it is highly uncertain whether such a correction improves or degrades the results.

In the case of wind, the model evaluation is more complex since altitude as well as small local topographic features around the station can influence the model validation. Moreover, only 1 station recorded hourly wind speed and direction in the central coast sub-region, while 2 stations on the northern coast and the central interior zone recorded these data on a 3-hour interval. After testing whether the wind data at these stations follow a Weibull probability distribution (Di Piazza *et al.*, 2010), which is expected if the stations are not influenced by local obstacles or very location-specific features, the central coast station failed the test and only the last 2 stations were retained for wind evaluation for 2003 and 2010. While it is possible to have wind statistics at some locations that do not follow the Weibull probability distribution, the fact that two stations in the study region followed it while one did not, casts doubts on the wind data quality at that central coast station, and thus it was excluded from the analysis.

2.3   Results and Discussion

2.3.1   *Temperature*

2.3.1.1 Average Temperature (Tavg)

The simulated impact of topography and altitude on the spatial patterns of yearly-averaged 2m temperature, and the clear distinction between Tavg in wet and cool (2003) versus dry and hot (2010) years in all three WRF resolutions, are depicted in Fig. 2.2. The coast is the warmest region, followed by a small zone of the mid-mountain ranges, and the majority of the area of the inland central and northern regions. WRF reproduced the expected average temperature drop at high elevations of the mountain

ranges and in the southern inland regions with higher spatial detail as the resolution is

made finer from 9 to 1km. The average temperature of the coast varied between 18 and

22°C, which are consistent with reported values of 20°C (Atlas Climatique du Liban,

1977; Lebanon SNC, 2011). Over the coast and in interior regions, average temperatures

in 2010 (18°C) are only slightly higher than in 2003 (17°C).
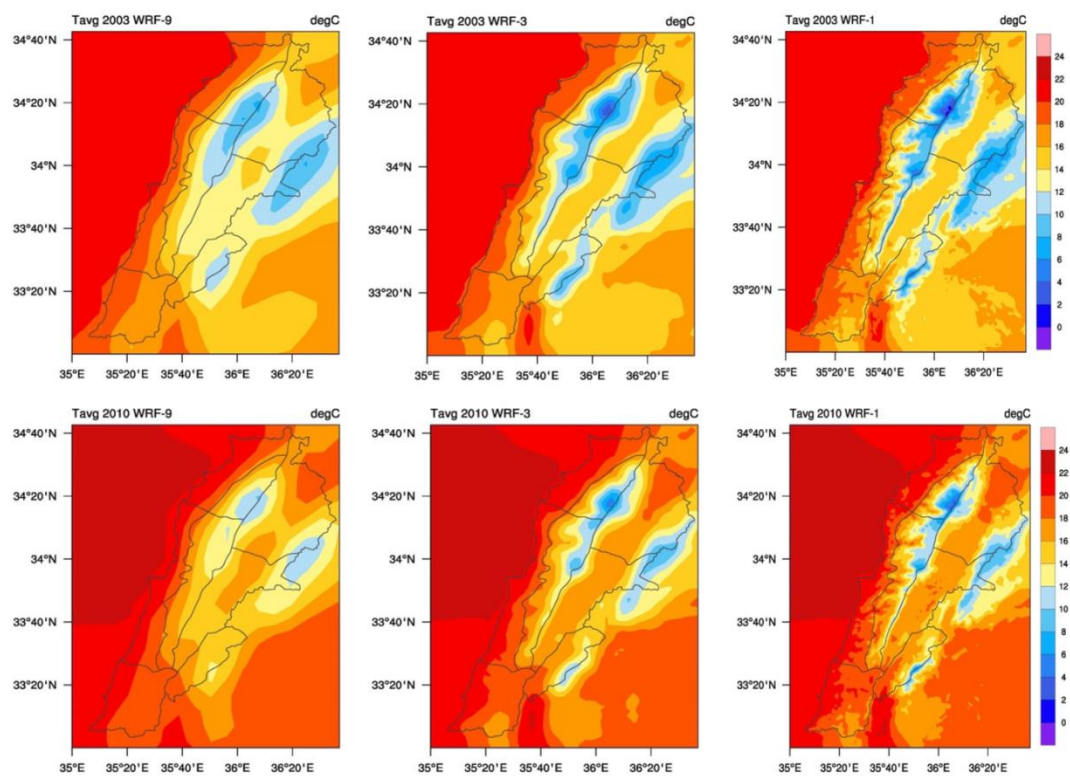
Fig. 2.2. Average 2m temperature from WRF-9, 3 & 1 simulations for 2003 and 2010

Since the study area has an extended and narrow form in addition to its

complex topographical features, local variations tend to be large. Therefore, the model

performance over individual sub-regions is more informative than its countrywide

performance. The number of weather stations measuring Tavg in each of the eight geo-

climatic regions varies from 0 to 4, since most stations for 2003 have records only for

Tmax and Tmin (refer to Appendix B). In order to compute the regional averages, the stations that report Tavg in each climate zone were grouped and then averaged (WRF results are also taken at the station locations only, and then averaged). The MAE of the daily-averaged 2m temperature for the different geo-climatic regions, categorized during various seasons of 2003 and 2010, is improved as WRF's grid is refined down to 1km (Table 2.1 and Table 2.2) (DJF: December, January, February; MAM: March, April, May; JJA: June, July, August; SON: September, October, December). They confirm that higher resolution leads to higher coefficients of determination and smaller absolute errors.

Table 2.1. MAE (°C) and R^2 for seasonally Tavg in 2003, lowest errors are in bold*

Region	WRF-1				WRF-3				WRF-9			
	DJF	MA	JJ	SO	DJF	MA	JJ	SO	DJ	MA	JJA	SO
NC	**1.1**	**1.5**	**1.3**	**1.2**	1.2	1.7	1.7	1.3	1.4	1.7	1.4	1.4
CC	**0.7**	2.0	**2.5**	**0.7**	**0.7**	**1.8**	2.6	0.8	0.9	2.0	2.8	0.9
CI	**1.4**	**1.4**	**1.3**	**1.4**	1.8	1.7	1.5	1.8	2.0	2.3	2.7	2.5
Study Area	**1.1**	**1.6**	**1.7**	**1.1**	1.2	1.7	1.9	1.3	1.4	2.0	2.3	1.6
R^2	**0.75**	**0.91**	**0.7**	**0.90**	0.74	0.90	0.7	0.88	0.7	0.89	0.83	0.86

No stations recorded Tavg in SC, NM, CM, NI and SI regions

Table 2.2. MAE (°C) and R^2 for seasonally Tavg in 2010, lowest errors are in bold

Region	WRF-1				WRF-3				WRF-9			
	DJ	MA	JJA	SO	DJF	MA	JJ	SO	DJ	MA	JJA	SO
NC	**1.7**	**1.4**	**2.0**	**1.6**	1.7	1.6	2.3	1.6	1.9	1.5	2.2	1.7
CC	**0.8**	**1.5**	**3.1**	**1.0**	**0.8**	1.6	**3.1**	1.1	1.2	1.8	3.4	1.4
SC	**1.3**	1.0	1.7	**1.3**	1.3	**0.8**	**1.5**	1.3	1.5	1.1	1.7	1.4
NM	**0.7**	**0.7**	**0.9**	**0.8**	1.2	0.8	1.0	1.3	1.7	1.3	1.2	1.9
CM	**1.1**	**1.0**	**1.2**	**1.2**	1.8	1.4	1.3	1.7	1.6	1.5	1.3	1.7
NI	**1.4**	**1.3**	**1.2**	**1.2**	1.4	1.4	1.2	1.3	2.4	1.6	1.4	1.7
CI	1.7	1.6	1.6	1.5	**1.7**	**1.5**	**1.5**	**1.3**	1.8	1.9	2.1	1.5
SI	**0.7**	**0.7**	1.2	**0.8**	0.7	0.8	**1.2**	0.9	1.0	1.3	1.8	1.3
Study Area	**1.2**	**1.1**	**1.6**	**1.2**	1.3	1.2	1.7	1.3	1.6	1.5	1.9	1.6
R^2	**0.82**	**0.87**	**0.7**	**0.88**	0.81	0.86	0.7	0.86	0.78	0.85	0.7	0.84

Fig. 2.3. illustrates that the WRF simulation with 1km resolution also outperformed the 9km resolution in all regions, resulting in an average reduction in the RMSE of 0.47°C for 2003 and 0.41°C for 2010. WRF 1km errors were also smaller than those of WRF 3km, but the differences were less significant with only 0.16 and 0.12°C improvement in the RMSE for 2003 and 2010, respectively. In most regions and seasons, the largest part of the RMSE error was due to the covariance term in all WRF resolutions, with few exceptions in the CC during MAM, CI during MAM, JJA and SON. This indicates that weather systems in WRF are arriving too early or too late compared to observations (note that since these are daily values, timing errors of less than one day cannot be detected). The BIAS was the second largest contributor to the error overall. On the other hand, the smallest part of the error is due to the variance (standard deviation) in all regions during all seasons, implying that the observed time variability (variance) is reproduced well by WRF. We are showing the decomposition of RMSE errors of WRF-1 only (Fig. 2.3) since the remaining resolutions follow the same trend.

The PDFs of the daily-averaged temperatures from the observations, and from the 9, 3 and 1km WRF simulations, for all four seasons of 2003 and 2010, were computed for all stations combined, and for conciseness only the best and worst seasonal performance of WRF (based on differences between WRF-1 simulated and observed Tavg) are presented in Fig. 2.4. The general trends of the distribution of WRF in its 3 resolutions match observations reasonably well, with WRF's finest resolution in general yielding PDFs closer to observations for all seasons. The satisfactory reproduction of these PDFs, particularly their tails, is a positive indication of WRF's ability to reproduce extremes.
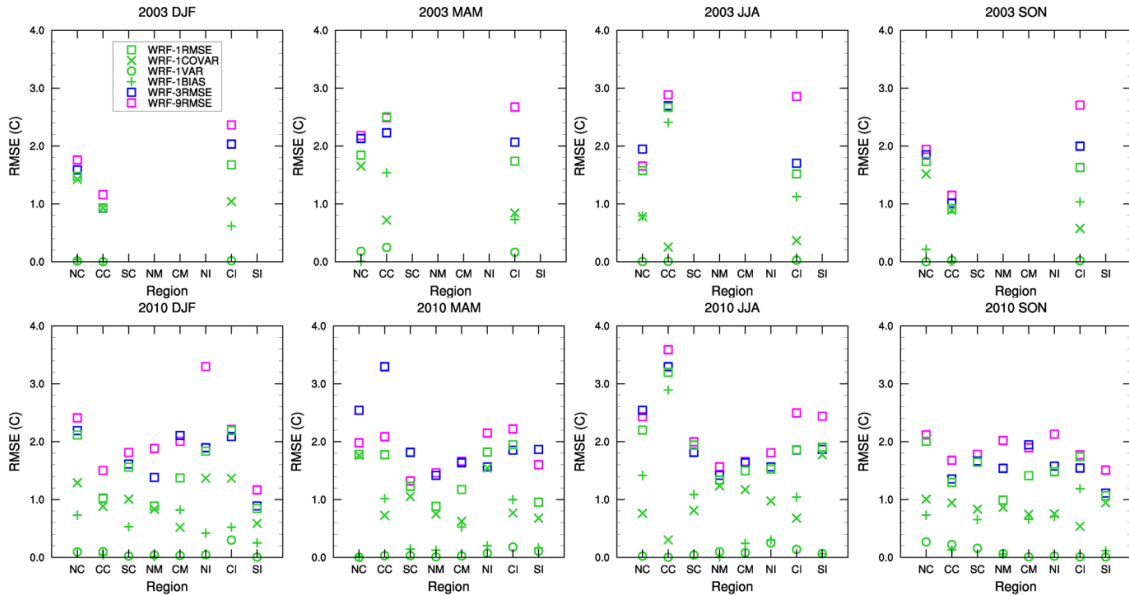
Fig. 2.3. Regional and seasonal RMSE for daily average 2 m temperatures for years 2003 and 2010, with decomposition of RMSE for WRF 1
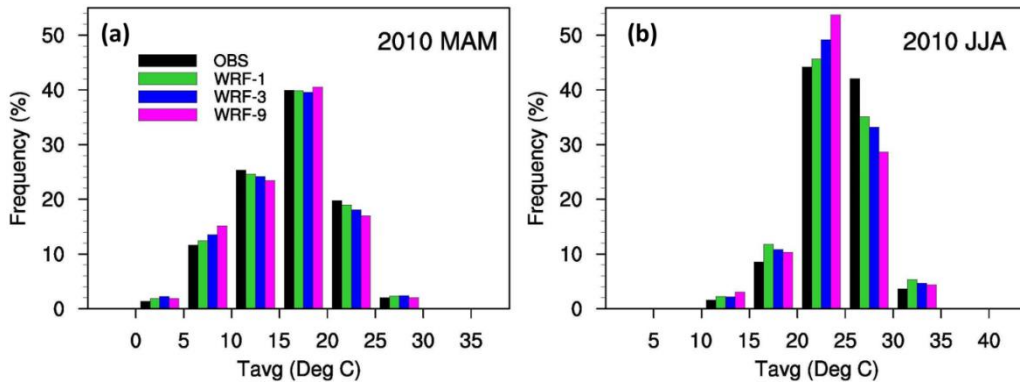
Fig. 2.4. PDFs of the daily average 2m temperature (a) best WRF fit (b) worst WRF fit

2.3.1.2 Maximum Temperatures Tmax

Seasonal and regional MAE analyses for the summer season for maximum 2m temperatures, along with the correlation coefficients are depicted in Table 2.3. MAEs for WRF 1 and 3 km are lowest in all regions, except in CM during 2003 and NM

20

during 2010. The coefficients of determination are closely comparable among the 3

WRF resolutions.

Table 2.3. MAE (°C) and R^2 for the summer season Tmax in 2003 & 2010,
lowest errors are in bold

	2003			2010		
Region	WRF-1	WRF-3	WRF-9	WRF-1	WRF-3	WRF-9
NC	**2.1**	2.5	2.7	**2.7**	3.1	3.4
CC	3.2	**2.9**	3.9	**4.0**	**4.0**	5.6
SC	**5.0**	5.6	5.6	**2.2**	2.4	2.7
NM	**3.4**	5.8	5.8	1.9	**1.7**	**1.7**
CM	2.8	2.9	**2.7**	**2.1**	2.4	2.5
NI	**3.1**	3.6	4.4	1.3	**1.2**	2.2
CI	**1.9**	2.9	4.4	**1.6**	2.6	4.0
SI	**3.6**	4.7	4.8	**1.8**	2.1	3.3
Study Area	**3.1**	3.9	4.3	**2.2**	2.4	3.2
R^2	0.66	**0.68**	**0.68**	**0.75**	**0.75**	0.74

In addition, the RMSEs of Tmax for years 2003 and 2010 were computed from

differences in the daily maximum values between WRF and station observations

(Fig. 2.5), but we will only consider the warm summer month since this is the critical

periods for high temperatures. In both years, WRF-1 is yielding smaller errors in all

regions except the central mountains in 2003. WRF-3 is also markedly better than

WRF-9 in all regions for both years. Interestingly, WRF-3 outperforms WRF-1 biases in

the northern mountain and northern inland regions in 2010, and the differences between

these two finest resolutions remain limited. Regarding the decomposition of the RMSE

in time and space, the 3 model resolutions exhibited similar trends. For clarity, we are

showing only the decomposition of RMSE related to WRF 1 in Fig. 2.5. Once again, the

errors related to the variance (standard deviation) are minimal in all regions during both

years. Interestingly, and unlike the mean temperature, the largest contribution to the RMSE came from the bias of the mean during 2003 and most of 2010, with the exception of the mountainous regions (NM and CM) and northern and southern inland regions (NI and SI) where the contribution of the covariance error is the greatest. This implies that WRF errors in underpredicting or overpredicting the maximum temperatures are overall more significant than the errors in the timing of these extremes (again the minimal time error that can be detected is 1 day).
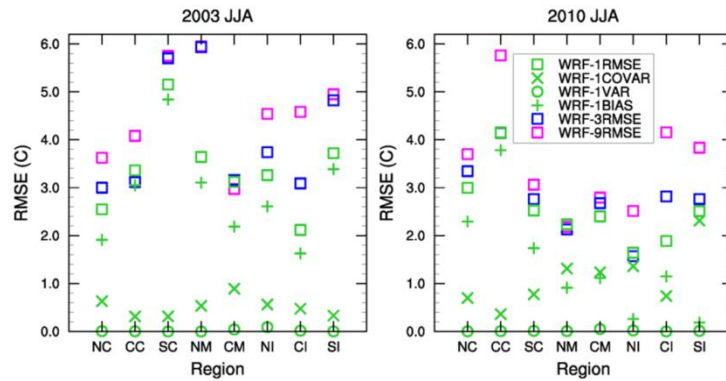
Fig. 2.5. Regional and seasonal RMSE for the summer season daily maximum 2m temperatures, with decomposition of RMSE for WRF-1

The PDFs of daily maximum temperatures for the 2003 and 2010 summer season, comparing WRF simulations to observations, are presented in Fig. 6. The summer season is normally defined as June, July and August (JJA), but for the computation of these PDFs we opted to include the month of May (M) in the summer season: early in May the Khamsin wind blows up the Levantine coast from the Sahara Desert and could yield high Tmax values. The temperature of the wind might exceed 40°C, conveying a heat wave over the study area (Blanchet, 1965). The added value of

finer resolutions (WRF-1 and WRF-3) can be detected in the PDFs of MJJA of 2003 and 2010, although WRF tends to overestimate the frequency of Tmax<30°C, and underestimate the frequency of Tmax>30°C (particularly in 2003). A significant underestimation is noted in bins between 30°C and 35°C. Higher WRF resolutions can only mitigate some of this misrepresentation: WRF-1 and WRF-3 captured the observed hot season PDF of 2010 well, while WRF-9 continued to exhibit an underestimation between 35°C and 40°C bins. In general, the match between the simulated and observed PDFs of Tmax is inferior to the match for Tavg.
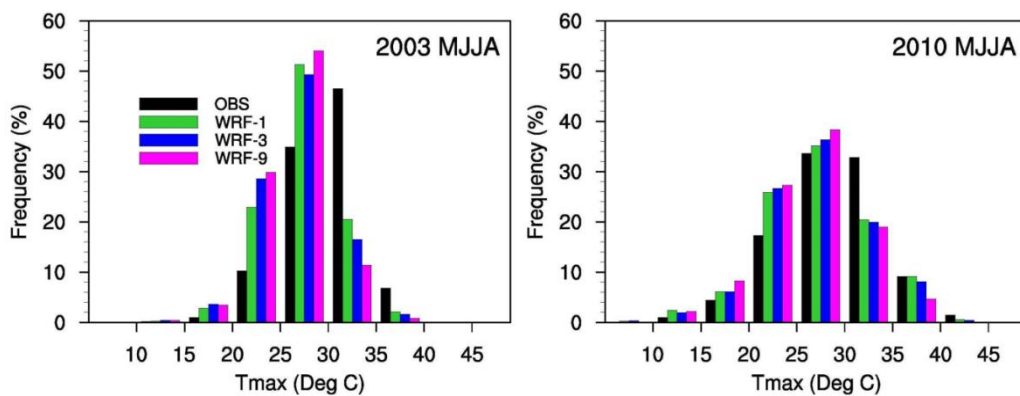
Fig. 2.6. Probability density plots of the daily maximum 2m temperature

2.3.1.3 Minimum Temperatures

A summary of the regional MAE analysis is shown in Table 2.4 for Tmin. MAE values indicate a good representation of Tmin by the WRF-1 during both years. In most regions, the error is improved by WRF-1 by ~0.4°C during 2003 and by 1.0°C during 2010, when compared with WRF-9; WRF-3 is also better than WRF-9 in most regions by ~0.2°C during 2003 and by 0.7°C during 2010. The RMSE of winter daily Tmin at a regional and a seasonal scale are presented in Fig. 2.7. The good skill of

WRF-1 in capturing Tmin is noticeable in most regions, except in the central mountain (CM) in 2003 and central inland (CI) in 2010 where WRF-1 yields the largest errors of all three resolutions. WRF-3 also yields lower errors than WRF-1 in the central coast (CC) 2003 and southern inland (SI) in 2010. Regarding the decomposition of the RMSE, Tmin follows the same trend as Tavg (rather than Tmax) in all of WRF 3 resolutions (only WRF 1km is shown in Fig. 2.7). The errors related to the variance (standard deviation) are minimal (except in NI during 2003) and the highest contributions to the RMSE were from the covariance error in most regions during both years with a few exceptions.

Table 2.4. MAE (°C) and R^2 for the winter season Tmin in 2003 & 2010, lowest errors are in bold

Region	2003			2010		
	WRF-1	WRF-3	WRF-9	WRF-1	WRF-3	WRF-9
NC	**1.4**	1.6	2.0	**3.0**	3.1	4.2
CC	1.5	**1.3**	1.8	**1.6**	1.7	3.0
SC	2.0	1.4	**1.0**	**2.3**	2.8	3.1
NM	**1.3**	1.6	1.6	**1.4**	2.2	2.7
CM	3.8	**3.3**	3.4	**1.1**	1.3	1.6
NI	**2.3**	2.6	2.6	**2.1**	2.3	3.7
CI	**1.7**	1.9	1.9	3.5	3.6	**3.4**
SI	**1.9**	2.4	2.8	1.3	**1.2**	1.3
Study Area	**2.0**	2.0	2.1	**2.0**	2.3	2.9
R^2	**0.61**	0.60	0.59	**0.64**	0.63	0.57

The coefficients of determination of Tmin between observations and WRF simulations are always lower than those of Tmax (Table 2.3 and Table 2.4). A possible cause that could account for these differences is that night-time temperature minima in the diurnal cycle are difficult to capture: this is a limitation with atmospheric models

such as WRF that has often been reported before (Paimazumder *et al*., 2012; Talbot *et al*., 2012). It is related to the difficulty in parameterizing PBL turbulence under stable night-time conditions (Huang and Bou-Zeid, 2013; Huang *et al*., 2013; Shah and Bou-Zeid, 2014), compared to unstable/mixed daytime conditions. In an attempt to reduce the nighttime errors, a change from Mellor-Yamada Janjic (Eta) to Yonsei University (YSU) PBL scheme was tested for a 4-months simulation period (February and November 2003, August and December 2010). There was not much improvement in the night temperatures, while an increase in the precipitation bias was noted. Subsequently, the original Mellor-Yamada Janjic (Eta) PBL parameterization scheme was retained in the WRF model set-up.
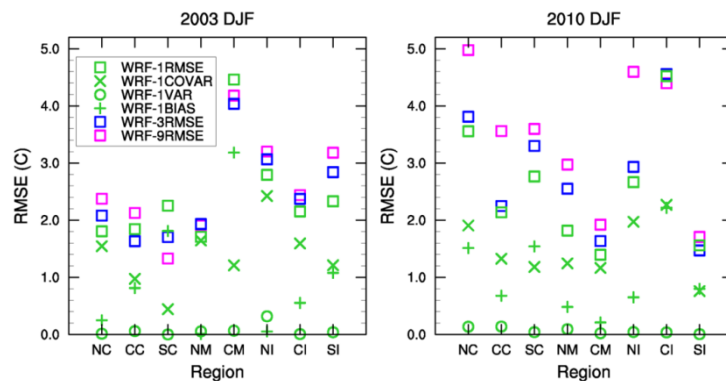
Fig. 2.7. Regional and seasonal RMSE for winter season daily minimum 2m temperatures, with decomposition of RMSE for WRF-1

The frequency distributions of Tmin, shown in Fig. 2.8, illustrate in a different way the seasonal dependence of the model's performance in capturing daily variability and extremes. Generally, the agreement between WRF-1 and observed minimums is satisfactory in the winter of 2003. In the winter of 2010, WRF-1 is close to observations

in more than half of the bins. The WRF-1 simulated distribution of minimum temperatures is skewed to the right in DFJ 2010, where the model is predicting higher Tmin, and hence underpredicting the probability of occurrence of very cold minima. Along with Tmax simulations, these results point to the fact that WRF tends to underestimate the severity of extreme temperatures in general (it produces milder temperatures), although not excessive, this bias should be taken into account when downscaling future climate scenarios.
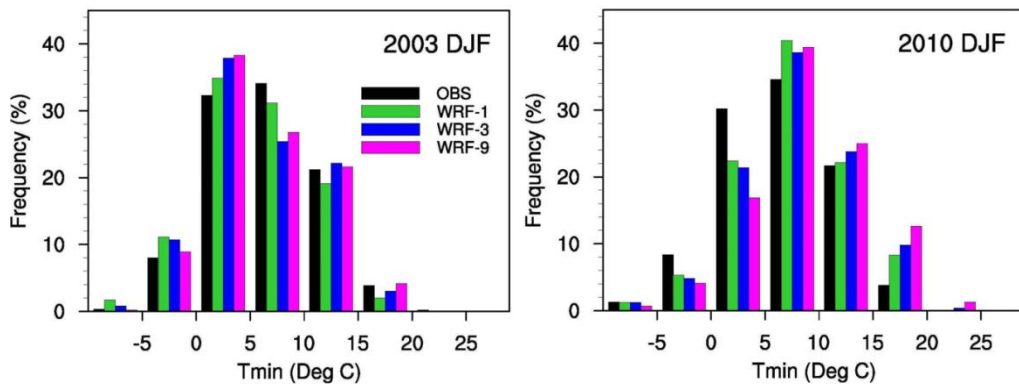
Fig. 2.8. Probability density plots of the winter season daily minimum 2m temperature

2.3.2   *Precipitation*

The various climatic references for the study area report an average annual rainfall along the coastal zones between 700 and 1000 mm, with an increase from South to North due to the increase in the mountain heights producing the orographic precipitation as shown in Appendix C (MOA/UNDP/GTZ, 2003), which depicts a multi-year average precipitation map. The West Mountains range forms a barrier against inland moisture movement, and the precipitation it generates on the upwind western slopes can reach more than 1400 mm per annum (there are no snowfall measurements in

the study area, hence the term precipitation used here is indicative of rainfall only for both observed and simulated values). This dries up the air masses flowing east, and rainfall decreases rapidly on the eastern slopes of the west mountain range and registers only 600 mm inland. Rainfall inland varies between 800 mm (central inland, leeward of the lowest mountains) and 200 mm (northern inland, leeward of the highest mountains). As for the East Mountains chain along the eastern border of the study area, rainfall is about 600 mm and increases up to more than 1000 mm at high elevations. Precipitation in dry years can be as low as 50 percent of the average. Coastal regions receive between 50 and 80 days of precipitation (Atlas Climatique du Liban, 1977; MOA/UNDP/GTZ, 2003, UNDP/GEF and MPWT/DGU, 2005; Lebanon SNC, 2011).

The cumulative annual precipitation from WRF 9, 3 and 1km for 2003 and 2010 is illustrated in Fig. 2.9, depicting a coherent pattern corresponding to the topography and matching the sub-regional divisions remarkably well (Atlas Climatique du Liban, 1977, MOA/UNDP/GTZ, 2003). The spatial distribution in WRF-1 clearly captures the broad tendency towards decreased precipitation at the northern coast (which matches observations) in comparison to the other coastal zones (partially due to the wider coastal plains upwind of the west mountain range as depicted in Fig. 2.9). Additionally, WRF-1 captures the maxima along the west mountain range and the minima further inland, as well as the peak in the coastal zone and the southern inland region. WRF-3 captures most of these spatial patterns and tendencies, while WRF-9 seems to blur the precipitation contours significantly. Interestingly, the 3km resolution was adopted in similar topographies by Trapero *et al*. (2013) to examine the effect of the orography on heavy precipitation events in the Eastern Pyrenees. The difference in

the rainfall between the wet 2003 and the drier 2010 is significant, and is also captured by WRF.
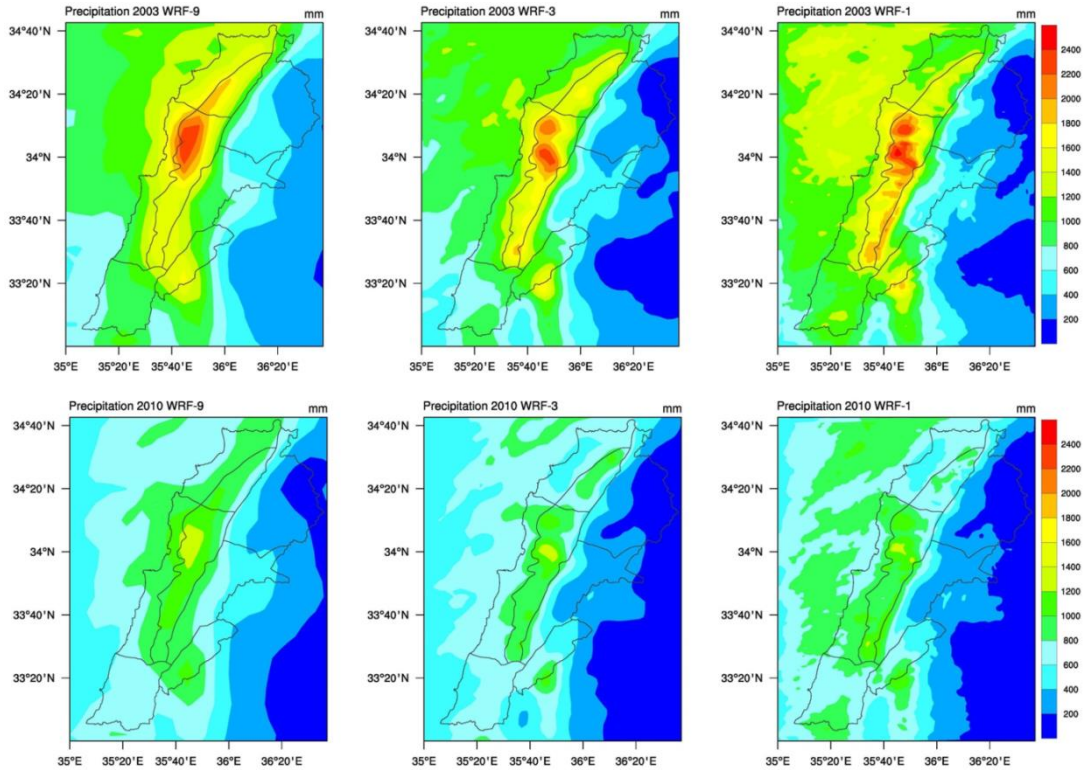
Fig. 2.9. Annual precipitation from WRF-9, 3 and 1km simulation for 2003 and 2010

For every station, total monthly precipitation was calculated and the process was repeated for the closest WRF grid point, then the bias was computed as a percentage difference between the simulated and observed total yearly precipitation for every station independently, and then averaged for each region, and then over the whole study area (Table 2.5). The study area bias and coefficient of determination between WRF and the observational data were calculated by pooling all individual stations together without regionalization. This approach was adopted because the interest is primarily in the overall water budget of the region and due to the fact that the temporal

and spatial locations of precipitation events are exceedingly difficult to reproduce accurately (Li *et al*., 2013; Ryu *et al*., 2016). In individual sub-regions, particularly the Northern Mountains and Northern Inland regions, biases can reach about 50%. However, with respect to the overall study area, which is of most importance from a water resources management perspective, the biases of WRF 1km and 3km are very acceptable, and they perform better than WRF 9 km, especially in the dry year 2010.

Note that in an attempt to reduce the bias, a change in model configuration from 35 to 56 vertical levels was tested for a 2-months period (February 2003, August 2010). In parallel, the same period was also configured based on 26 vertical levels. An increase in the precipitation bias was noticeable as the number of levels increased with a concurrent decrease in the temperature bias. Subsequently, the original 35 vertical levels configuration was retained in the WRF model set-up since precipitation is more critical for our future applications, but for application where temperature is the more important metric, a higher number of vertical levels might be useful.

Table 2.5. Percentage MBE and R^2 for yearly precipitation in 2003 and 2010, lowest errors are in bold

	2003			2010		
Region	**WRF-1**	**WRF-3**	**WRF 9**	**WRF-1**	**WRF-3**	**WRF 9**
NC	-7.2%	-42.5%	**0.6%**	16.1%	**15.1%**	38.4%
CC	19.4%	**3.9%**	24.3%	14.1%	**6.0%**	15.4%
SC	**-2.3%**	-15.7%	-9.3%	14.0%	-3.4%	**0.2%**
NM	**37.8%**	46.2%	49.7%	**26.0%**	52.9%	47.7%
CM	10.9%	**-3.9%**	-11.1%	4.7%	**4.6%**	6.3%
NI	-49.2%	-54.5%	**-43.1%**	-37.4%	-37.8%	**-8.4%**
CI	-18.3%	-27.9%	**-6.0%**	21.4%	**16.4%**	64.2%
SI	**19.7%**	37.1%	25.5%	9.3%	**5.4%**	40.0%
Study Area	**-2.01%**	-9.75%	2.16%	6.8%	**3.8%**	17.6%
R^2	0.64	0.60	**0.66**	**0.70**	0.64	0.57

Fig. 2.10. shows the RMSE for annual accumulated precipitation of WRF 9, 3 and 1km along with the decomposition of the RMSE of WRF 1km. The performance of WRF 1 and 3km was inferior to that of WRF 9km during 2003, confirming the results obtained for the MBE for that year (Table 2.5). Results for 2010 yield an improvement of WRF 1 over WRF 3 and 9km. Interestingly, the major source of error for precipitation seems to vary regionally and between years, with no strong dominance of the BIAS, VAR, or COVAR terms.
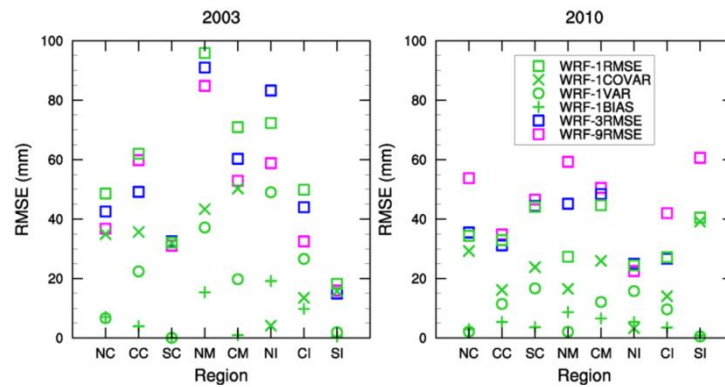
Fig. 2.10. Regional RMSE (mm) for rainy season precipitation, with decomposition of RMSE for WRF-1

One important aspect in the evaluation of a model is its competence in reproducing the strength and occurrence of separate precipitation events. Precipitation in the study area happens mostly as short time rainfall events and displays a clear annual cycle with very dry summers. The high precipitation events in the study area are often connected with adverse hydrological consequences such as road and channel floods and landslides. Consequently, simulating the higher ends of the precipitations PDFs is a necessary skill for WRF. To account for the rainy season extreme events, we applied a

filter so that dry days from May to September at all localities are removed, keeping only the days with precipitation strictly greater than 0 mm/day. Fig. 2.11 shows a representative selection of the resulting simulated PDFs of the mean daily precipitation simulated compared with the observations for the eight regions of the rainy season (October to May), and for both 2003 and 2010, the complete PDFs for all regions are shown in Appendix D. Given the challenges related to the simulation of precipitation the match between observed and simulated PDFs is in fact surprisingly good. During both years, WRF overestimates the occurrence of rainy days with less than 0.2mm of accumulation in all regions (Fig. 2.11 and Appendix D). This might be due either to light rainfall formation in WRF (e.g. as dew) or to the low resolution of rainfall gages (typically tipping buckets are used) that prevents them from detecting light rainfall events. It also overestimates the prevalence of days with rainfall accumulation between 0.2 and 1mm along the coast (Fig. 2.11a and Appendix 4) while it underestimates the occurrence of days with rainfall between 5 and 10mm in the mountains (Fig. 2.11b and Appendix D) as well as along the northern and central coast (Fig. 2.11a and Appendix D). The PDF is better reproduced for the higher rainfall rates, which are more relevant. The overall distribution of rainfall is simulated particularly well in the central and southern inland (Fig. 2.11c and Appendix D), albeit with a tendency to overestimate the probability of moderate precipitation (days of rainfall between 1 and 5mm); the overestimation is reduced by WRF-1. Likewise, WRF-1 is generally capable of simulating topographic impacts on extremes (days of rainfall beyond 5mm), especially over mountainous regions (Fig. 2.11b and Appendix D) during the wet year 2003, with WRF-9 overestimating the probability of intense rainfall more than the finer resolutions.

31

The change in the results with increasing resolution is in general smaller when going

from WRF-1 to WRF-3, compared to going from WRF-3 to WRF-9.
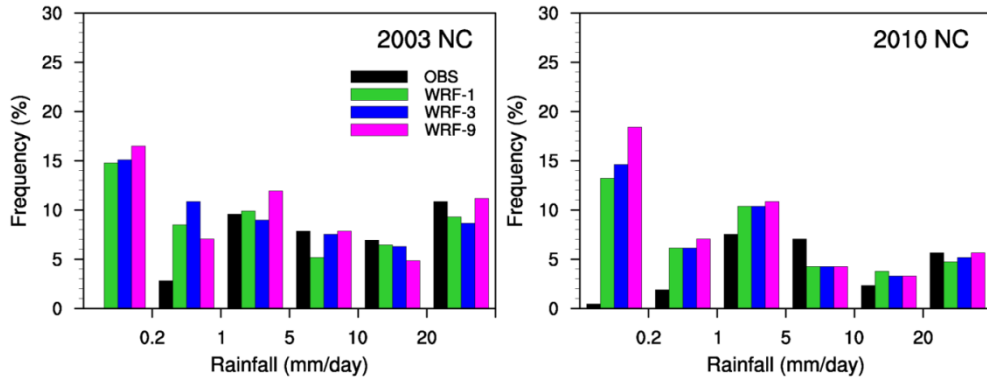
a. Northern coastal regions
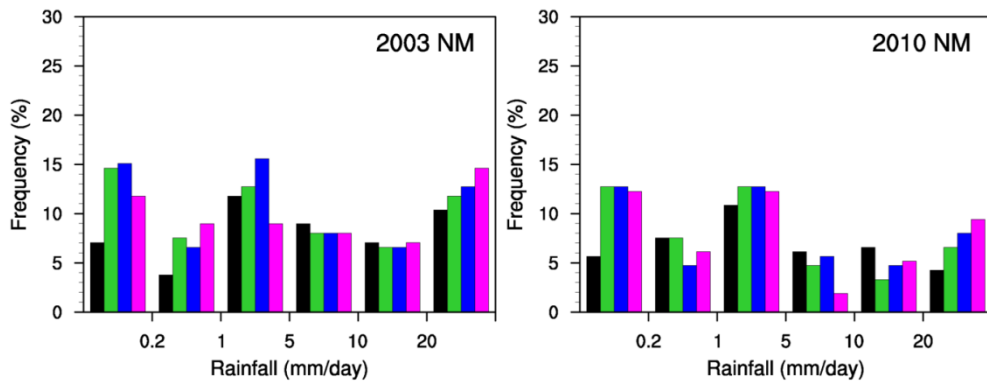
b. Northern moutainous regions
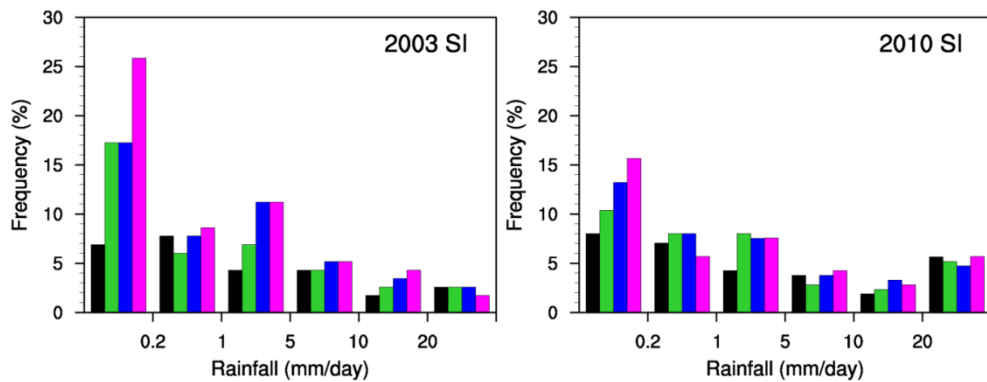
c. Southern inland regions

Fig. 2.11. Probability density of averaged daily precipitation for 2003 and 2010 in
northern coast (NC), northern mountainous (NM), and southern inland (SI) regions

2.3.3 *Wind*

The wind data in the study area is not as comprehensive as the temperature or precipitation data. Humid maritime air is gusted from the sea during the rainy season (October to May) and produces snow at high altitudes when mixed with continental dry and cold air from the Caucasus and the Balkans entering the study area through the northeast and the southern inland region. During the summer season, very humid and warm air blows also from the littoral after passage over the sea, but the higher temperature reduces the relative humidity, which eliminates rainfall occurrence (UNDP/GEF and MPWT/DGU, 2005).

As stated in Section 2.2.5, two stations were used for the wind evaluation: one (TRP) located along the northern coast and the second (HAO) situated in the central inland. The predominant wind directions experienced during 2010 are displayed in Fig. 2.12 in a series of wind roses for the observed (at 3 hours interval) and corresponding simulated WRF-1 speeds and directions. The wind roses for 2003 follow the same direction and hence are shown in Appendix E. The number of periods with wind blowing from a particular direction is indicated by the radius of the wedge extending toward that direction, while the colors denote ranges of wind speeds. The average mean wind direction for both stations exhibited a consistent bias during both years of +16° for HAO and –22° for TRP, which is also apparent in the wind roses (the roses align better if bias correction is made). The persistence of the bias with similar values for both years at each station is more suggestive of errors related to the alignment of the wind vanes than model errors. Wind vanes should be oriented to the geographic North, which is often identified using a compass that indicates magnetic North. Accurate correction for this discrepancy is not always performed; in addition, potential

human errors in reading the compass and aligning the vane correctly could also lead to a consistent bias. The magnetic declination angle in the project area is about 12 degrees west, which would explain most of the inland station bias, but would exacerbate the northern coast station bias. This bias explains why at the inland station, while most of the observed wind blows from the West and South-West with a significantly lower frequency for the wind from the North-West direction, the occurrence of wind blowing from the North-West direction in WRF is more common. In addition, WRF overestimates the wind speed consistently from all directions. The same observed wind rose shows that the wind rarely blows from the South East direction at the inland station, a fact mirrored by WRF-1. At the coastal station, the dominant observed wind direction is from the West, followed by weak winds from the South-West and South-East directions, and a minor fraction of slightly higher speed winds blowing from the West-North-West direction. WRF-1 intensifies the speed of winds blowing in all directions (as in the inland station), and its bias of $-22°$ diminishes the occurrence of westerly winds and increases the occurrence of south-westerly winds.
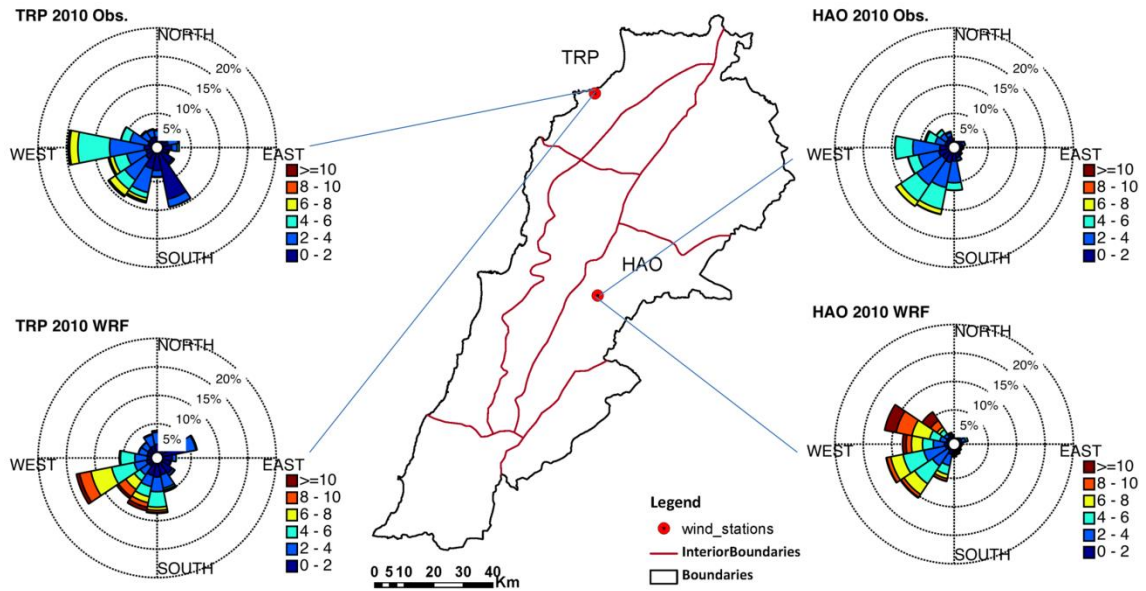
Fig. 2.12. Wind roses for available stations for 2010

The observed average daily wind speed at these stations varies from 0.5 to 6.6m/s inland, while it increases in the simulations up to 12.6m/s at the northern coast. The wind speeds are generally more overpredicted (about 50%) on the coast than inland (around 40%) in the three model resolutions (not shown). Concerning the statistical errors, Table 2.6 points out an important improvement in the MAE added by WRF 3km which in general performs better then the 1km, and some deterioration for the WRF 9km. However, the highest coefficient of determination achieved by WRF 1km. Fig. 2.13 shows that the largest part of the RMSE for WRF 1km was due to covariance error at both stations during both years. The average statistics confirm that all resolutions have analogous results and that increasing the grid resolution to 1km does not generally result in a significant improvement. These results clearly reflect what was expected: as the terrain complexity increases, the model struggles to simulate accurately the wind regime, especially the wind speed.

35

Table 2.6. MAE (m/s) and R^2 for the yearly average wind speed in 2003 & 2010, lowest errors are in bold

Station	2003			2010		
	WRF-1	WRF-3	WRF 9	WRF-1	WRF-3	WRF 9
HAO	1.13	**0.85**	1.14	1.22	**0.94**	1.06
TRP	1.11	1.10	**1.10**	1.03	1.00	**0.94**
Study Area	1.12	**0.98**	1.12	1.13	**0.97**	1.00
R^2	**0.53**	0.51	0.46	**0.46**	**0.46**	0.38
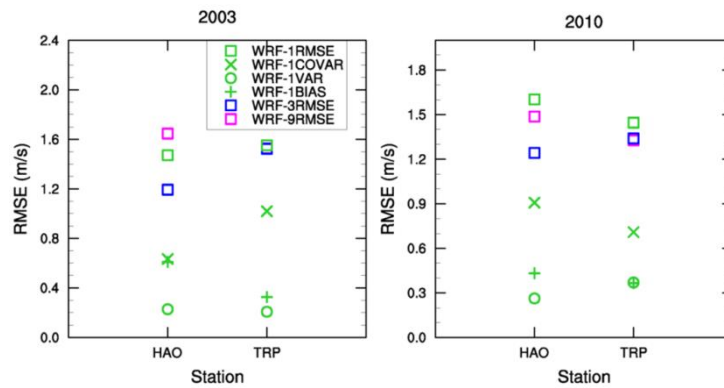
Fig. 2.13. Regional RMSE (m/s) for annual wind speed at the considered stations, with decomposition of RMSE for WRF-1

Regarding the wind speed extremes, a comparison from the seasonal PDFs of the two stations for 2003 in Fig. 2.14 illustrates that WRF underestimates the low winds (less than 4m/s) and overemphasizes the moderate winds (5-10m/s) during all seasons in both years. The same trend is observed during 2010, as shown in Appendix F. The error for the wind speed may be aggravated by measurement errors if the cup anemometers, which have errors that are typically higher than other anemometers, do not start registering wind speeds until a minimum speed is reached (usually around 0.5 m/s, which are a common shortcoming of mechanical anemometers). If that is the case, wind

speeds less than this cutoff will be registered as zero, erroneously decreasing the

observed averages.
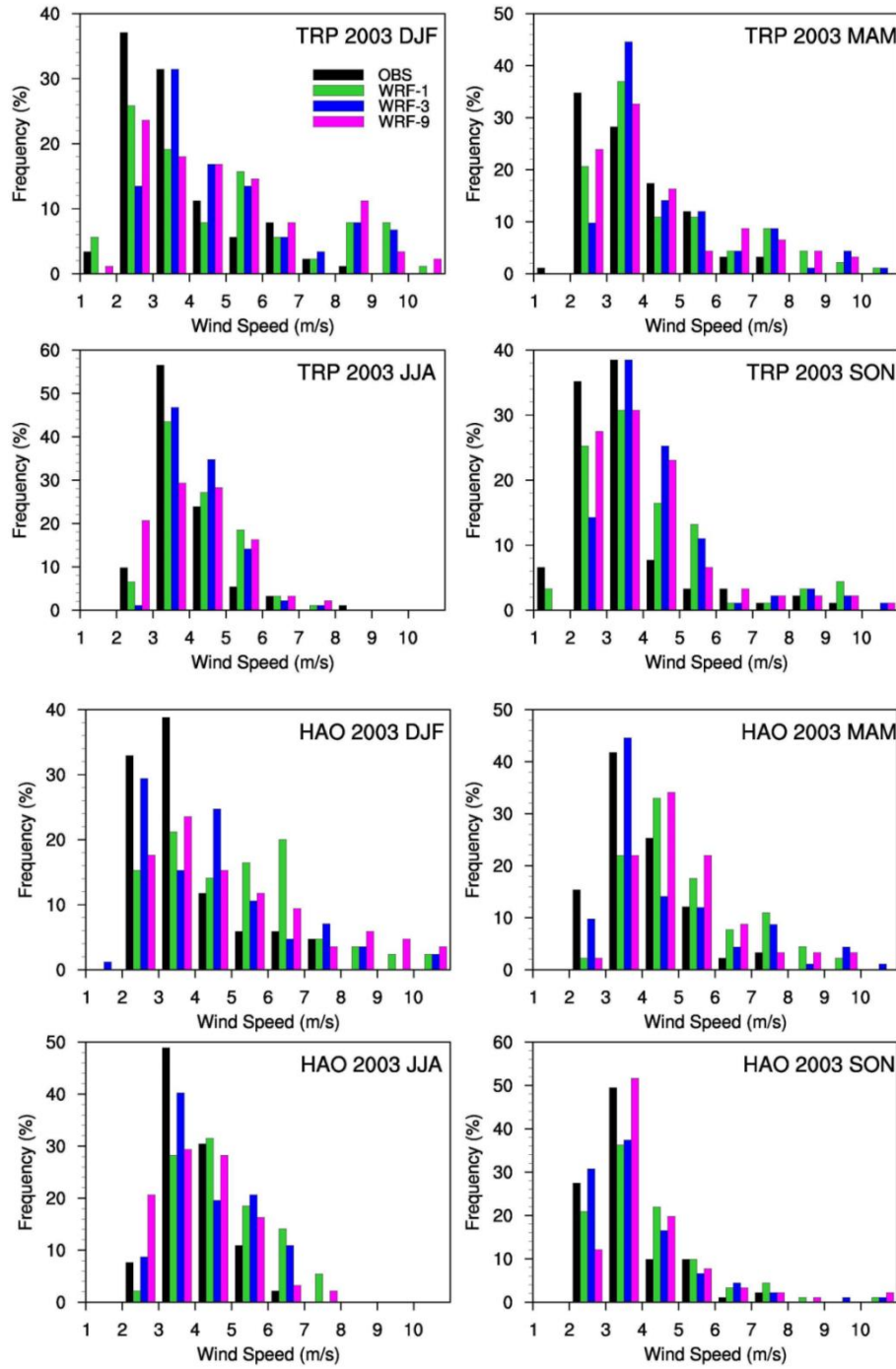
Fig. 2.14. Wind speed seasonal PDF of coastal (TRP) and inland stations (HAO) for
2003

2.4   Summary and Conclusion

This chapter presents an evaluation of WRF simulations over a complex topography domain along the Eastern Mediterranean for a wet year (2003) and a dry / hot year (2010) to examine its skill as a tool for climatological downscaling and its capability to capture the climatology of extreme events. The study area covers ≈ 30,000km^2, but is characterized by strong spatial heterogeneity of the precipitation fields associated with its complex topography and coastal effects, and a large inter-annual variability typical of the Mediterranean climate. These attributes make it an excellent candidate for assessing the skill of WRF over complex terrain.

Overall, WRF performance was satisfactory. It captured the complex spatial and seasonal variability that characterizes the observed climate of the study area and reproduced the differences between the mild, wet year and the hot, dry year well. The reduction in errors gained from the increase in WRF resolution was noticeable for maximum temperatures, which are central to climate change impact studies. Accumulated yearly rainfall, another key parameter in impact studies, was reproduced very well by WRF. These conclusions hold for the 1km resolution domain but also for the 3km resolution run, the performance of which was overall quite similar to the finer domain. At a resolution of 9km, deterioration in the simulated temperature and precipitation fields was clear, indicating that a 3km resolution is necessary and sufficient for downscaling climate fields over complex terrain if year-long simulations are to be performed (1km might be a better option for shorter periods). The wind speed and direction were more challenging for the model to reproduce at all resolutions.

Given that omitting the 1km domain (which has to be run with a shorter time step) reduces the computational cost of the simulation by about 70%, allowing the

downscaling of more future years to represent better the climatic extremes, limiting the finest resolution for downscaling to 3km is advisable. In addition, the MYJ PBL scheme yielded better precipitation than the YSU PBL schemes in our tests, but the comparison to other schemes and over other domains would be required to develop better guidance regarding the role and influence of the land and PBL schemes.

CHAPTER 3

CAN HIGH RESOLUTION DYNAMICAL DOWNSCALING IMPROVE THE REPRESENTATION OF CLIMATIC EXTREMES OVER COMPLEX TERRAIN?

3.1   Introduction

The resolution of the contemporary global climate models (GCMs) remains deficient in resolving mesoscale atmospheric circulations, such as those forced by complex topography and small scale surface irregularities.. Since climate impact studies require small-scale information that can only be obtained from high resolution models, methods for downscaling output from coarse grid GCMs are increasingly used (particularly over the last decade). One such technique is the one-way nesting, also known as a dynamical downscaling technique (in contrast to statistical downscaling techniques that establishes empirical relationships between large-scale climate and local climate based upon statistical methods). With this method, the downscaling is realized over a designated region by nesting (most frequently offline, after the GCM runs are completed) a high-resolution atmospheric regional-climate model (RCM) within a GCM (Giorgi and Mearns, 1991; Antic *et al.*, 2004; Laprise, 2008). Dynamical downscaling has been studied since the early 1990s (Giorgi, 1990; Leung *et al*., 1996) using RCMs with spatial resolutions of 50–60 km and evolved down to a finer spatial resolution on the order of 1 km (Caldwell *et al*., 2009; Gao *et al*., 2012; Li *et al*., 2013; Talbot *et al*., 2012).

Since RCMs are limited area models used as a climate downscaling technique to generate an accurateregional climate, they have to be forced by meteorological and

surface initial conditions (ICs) and lateral boundary conditions (LBCs) at the periphery

of the regional domain (Davies, 1976). As such, the starting point of dynamical

downscaling is typically a set of coarse-resolution large-scale fields either from GCMs

or from global reanalysis, which are used to provide the ICs and LBCs to the nested

RCM. Typical reanalysis data that can be used for the representation of the synoptic

weather systems is the 1 degree National Centers for Environment Prediction (NCEP)

Final Analysis (FNL) derived from the Global Forecast System (GFS) reanalysis data

(NCAR/NCEP, 2000). Since reanalysis simulations assimilate a large suite of global

historic observations to force the GCM to match the actual weather realization in a

deterministic sense, downscaling based on reanalysis-driven simulations is only feasible

for historic periods and excludes GCM errors induced by the chaotic atmospheric

dynamics at various scales, as well as other GCM errors that could result in bias in the

forecasted climate. Reanalysis downscaling thus provides a lower bound on the

uncertainty involved in downscaling-regional climate predictions or GCMs in the future

where assimilation is not possible. Hence, reanalysis tests serve primarily to measure

the downscaling model's ability to simulate atmospheric dynamics, with minimal initial

and boundary conditions forcing errors. Moreover, RCM simulations are not designed

to modify the large-scale circulation of the GCM, but are rather envisioned to enhance

regional detail in response to regional scale forcing (e.g. topography, coastlines, and

land use/land cover) and mesoscale atmospheric processes (e.g. clouds, convection,

secondary circulations) as they interact with the larger-scale atmospheric circulations

(Giorgi, 2006). As such, RCMs could reduce even further the reanalysis errors, but the

degree of this enhancement over complex terrain remains poorly characterized. The

driving questions of this chapter is therefore "can high resolution dynamical

downscaling improve the representation of climatic extremes over complex terrain?", or its reverse "will the RCM simply inherit and downscale the errors of its parent/driving model?"

In this chapter, we intend to answer this question using the Weather Research and Forecasting (WRF) model (Skamarock *et al.,* 2008) at 3km grid resolution. We examine how realistically this model can simulate the spatiotemporal variability and extremes of the temperature and precipitation fields, in comparison with NCAR/NCEP FNL 1 degree data used to drive WRF. Since the focus is on extremes, we select one historic wet and cold year (2003) and one historic dry and hot year (2010) and compare the modelled data to observations. Extreme conditions over complex terrain distinguish this study, and provide further support for the use of WRF as a regional/local downscaling model. In chapter 2, the role of WRF resolution was assessed by comparing the results from simulations at horizontal resolutions of 9, 3 and 1 km against observational data. The 3 km resolution was adopted as optimal since its accuracy was comparable to the finer 1 km simulations, but at a much more advantageous computational time.

3.2   Methods and Data

3.2.1   *Model Domain: Pilot Study Area*

The country of Lebanon, located on the eastern shores of the Mediterranean (Fig. 3.1a), extends over a total area of 10,452 km^2 most of it being mountainous terrain. The two mountain ranges run parallel to the sea, separated from each other by the inland plain (Fig. 3.1b). Lebanon's mountainous terrain, small area and proximity to the sea and the Syrian desert in the north result in large climate gradients that validate its need

for high resolution climatology. The two west and east mountain chains produce a climatic variability over very short distances whereby a 50 km west-east cross section yields significant climate disparities: a subtropical climate along the coast, followed at by a characteristically Mediterranean climate at low altitudes, the cold weather occurs at higher elevations which are covered with snow during the winter and helps in sustaining a base yield for about 2000 springs during the dry period, in contrast to a relatively dry semi-desert inland plain. This variability causes substantial challenges for climate models aiming to reproduce this abundant diversity in ecosystems over a rather small surface area.
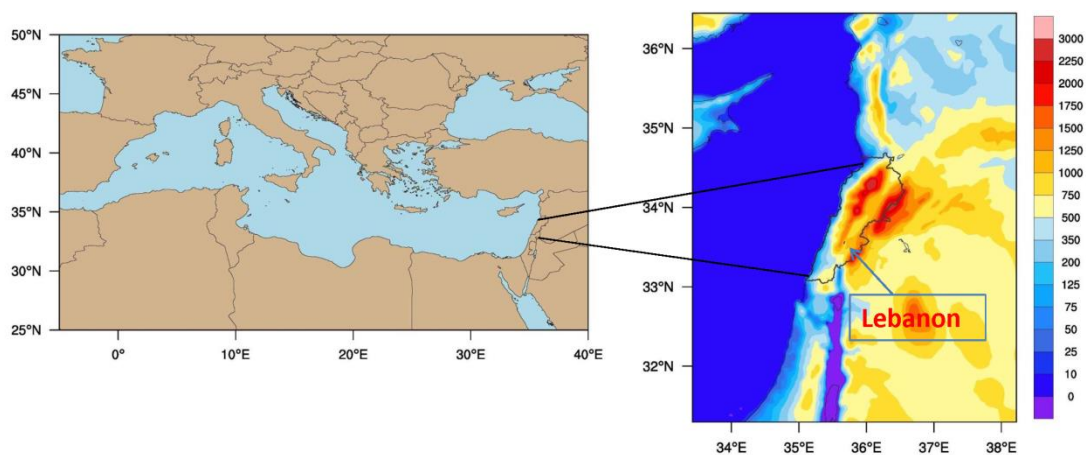
Fig. 3.1. (a) Eastern Mediterranean basin,
(b) Inner WRF 3km domain with terrain height of the study area

3.2.2   Model Setup

The present study used the WRF model (v. 3.4.1) which is a non-hydrostatic model, appropriate for simulating a large range of scales, from thousands of kilometers to a few meters (Skamarock *et al*., 2008; Soares *et al*., 2012). In this study, WRF was

setup with two nested grids, the first at 9 km (WRF9) and a second at 3 km (WRF3) horizontal resolution, using one-way nesting. Both grids are centered in the study area and the inner domain WRF3, the focus of our analyses (referred to simply as WRF in the remainder of this chapter), has 154×193×35 grid points, covering the area shown in Fig. 3.1b. The largest domain was intended to cover a relatively large sea area, minimizing spurious boundary effects in the smaller domain. MODIS (2001) land use data was adopted with 21 land categories and Lambert Conformal projection, which is most convenient for mid-latitude regions and provides homogeneous grid spacing, unlike latitude-longitude coordinates. The time step used was 30 seconds for the smallest domain, and, the 35 vertical levels were vertically-stretched and arranged according to terrain-following hydrostatic pressure coordinates.

The model is initialized by initial and boundary conditions using NCAR-NCEP's GFS Final Analysis (FNL) data (NCEP-ds083.2), with a resolution of 1°x 1° (111km x 111km). The time interval of the boundary data is 6 hours, while the sea surface temperature (SST) was updated once monthly. No nudging was applied during the simulations. All the WRF runs started at 0000UTC at the beginning of each month of years 2003 and 2010 to prevent the model from drifting far from the observed weather by reinitializing it with the reanalysis data. This method has the additional benefit of allowing simultaneous simulations for several months, significantly reducing the wall-clock simulation time (Pan *et al*., 1999; Caldwell *et al*., 2009). While the year 2010 was a very hot and dry year that is used here as an example of an extreme period, we also compare the modeling results to a relatively cold and wet year, 2003.

The selected physical parameterizations comprise the microphysics WSM 6 class single-moment scheme by Hong and Lim (2006), the planetary boundary layer

scheme of Monin Obukhov and Mellor-Yamada-Janjic (Mellor and Yamada, 1974; Janjic, 2001), Rapid Radiative Transfer Model (RRTM) (Mlawer *et al*., 1997) and Dudhia Long Wave and Short Wave (LW/SW) for radiative processes (Dudhia, 1989), and the Noah Land Surface Model (LSM) (Chen and Dudhia, 2001) for surface processes. These choices are supported by our previous WRF studies for mesoscale applications (Talbot *et al*., 2012 ; Li *et al*., 2013).

3.2.3   *Observational Data*

The study uses observational data of daily precipitation, as well as average, maximum and minimum 2 m temperatures. The observations are obtained from several climatic data sources (Atlas Climatique du Liban, 1977; NOAA's National Climatic Data Center (NCDC)[1], Lebanese National Meteorological Services (LNMS), Lebanese Agricultural Research Institute (LARI), American University of Beirut Advancing Research Enabling Communities Center (AREC), and individual researchers). These sources indicate that the climate of the study area can be further characterized as an oceanic climate during winter and a sub-tropical climate during summer. The National Meteorological Service had defined eight climatic zones which can be grouped into three main climatic trends (Fig. 3.2a): (1) the coast (northern (NC), central (CS) and southern coasts (SC)), (2) the mountains (northern (NM) and central mountains (CM)) and (3) the inland region (northern (NI), central (CI) and southern (SI) inland).

All the available observations were checked for reliability and continuousness during the simulation periods under consideration (Soares *et al*., 2012), retaining 31

---

[1]

http://hurricane.ncdc.noaa.gov/pls/plclimprod/poemain.accessrouter?datasetabbv=DS3505&countryabbv=&georegionabbv

temperature and 43 precipitation stations for this assessment (Chapter 2). Fig. 3.2b

presents the distribution of precipitation stations, and Fig. 3.2c shows the distribution of

temperature weather stations.
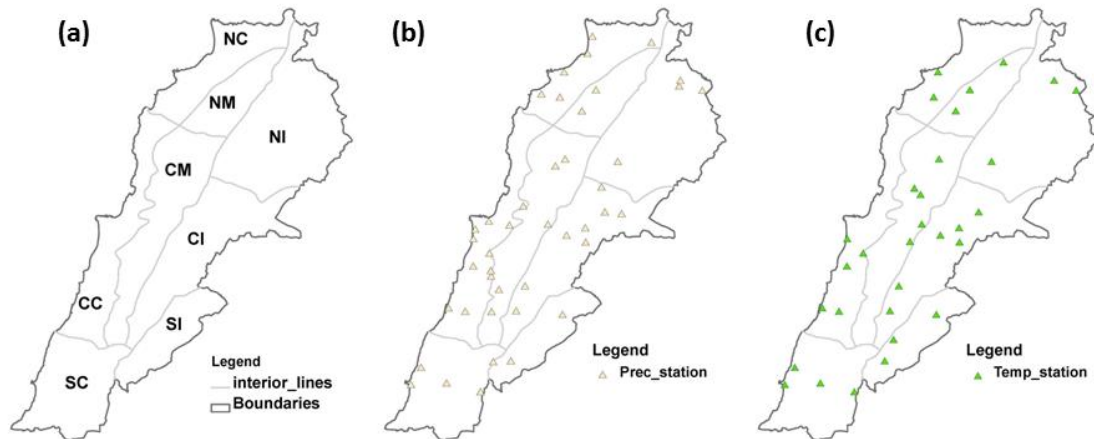
Fig. 3.2. (a) Study area geoclimatic regions, (b) 43 rain gauges locations,
(c) 31 temperature stations locations with records of both daily average and/or
maximum and minimum temperatures, per geoclimatic region

3.2.4   Data Handling and Analysis

The 3km WRF resolution simulation results and GFS reanalysis are matched

with local observational data using the nearest grid point of WRF and GFS. GFS was

interpolated to a 1° spatial resolution grid. The 2-hours WRF provided the 2m daily

average, maximum and minimum temperatures. For GFS, average, minimum and

maximum temperatures at 2 meters are found from the 6-hourly data by post-processing

of model output. No lapse rate correction was applied to temperature due to our fine

grid resolution (3 km), and since the environmental lapse rate over complex

topographical terrain would depend on several factors such as mountain width,

buoyancy, moisture fields (Smith and Barstad, 2004) and winds (Esteban and Chen,

2008) and would be difficult to estimate for the correction. Note that the reanalysis dataset did not include precipitation records for 2003 and 2010 for the domain under consideration. Hence, statistical comparisons for precipitation were confined to WRF simulations versus observations.

Several statistics were used to evaluate model performance using observational datasets such as the mean bias error (MBE), root mean square error (RMSE), and coefficient of determination R^2 (Willmott, 1982; Kobayashi and Salam, 2000). An additional regional statistical analysis was performed on the limited number of stations corresponding to each climatic zone. Extreme weather events are represented by the probability density functions (PDFs) of the temperature and percentiles of precipitation, and by an analysis of climate indices such as summer days, hot days, frost days, rainy days, rainfall intensity and length of wet period. These climate indices are established by the World Meteorological Organization working group, the Expert Team on Climate Change Detection and Indices (ETCCDI; Persson *et al*., 2007; Antic *et al*., 2004). Certain indices were modified to be more relevant to the study area. For instance, the ETCCDI hot-days (HD) index is the yearly count of days on which temperatures exceed 25°C, which is representative of an average summer day temperature, rather than an extreme (Shaban, 2011). Therefore, we used this threshold as characteristic of a summer day, while the hot days index threshold was modified to 35°C (Abdul-Rahman *et al*., 2011; Karmalkar *et al*., 2012).

3.3   Results and Analyses

3.3.1   Temperature

3.3.1.1 <u>Average Temperature (Tavg)</u>

The spatial distribution of the 2 m temperature RMSE (°C) calculated from the daily-averaged values at each station for years 2003 and 2010 are illustrated in Fig. 3.3. On average, WRF reduces the RMSE (computed from the 2-hourly values) by about 1°C for both years which is a significant improvement over GFS. The local error reduction is even larger in some regions, particularly in the NC, NI and CI regions. The coefficients of determination calculated from the daily mean values are high in both cases (GFS: 0.91, WRF: 0.94), partly due to the dominance of the seasonal cycle for this coefficient, to the fact that it does not capture mean bias (Fig. 3.4), and to the averaging out of diurnal cycle errors. Both models yield warm biases over the country in both years, (2003: GFS MBE= -1.89°C, WRF3 MBE= -1.08°C; 2010: GFS MBE=-0.56°C, WRF3 MBE= -0.09°C), with lower biases for WRF. Furthermore, the average statistics of the GFS-Reanalysis and WRF3 simulation show that there is a 1.17°C and 0.94°C inter-simulation disagreement between the two models for 2003 and 2010, respectively. The comparison between WRF simulations and the driving GFS-Reanalysis data reveals that WRF seems to generate spatial patterns and dynamics that are somewhat independent of the driving model and is able to maintain a small RMSE in the different regions, despite larger errors in the driving reanalysis. This can be attributed to the large domain size used for the coarser WRF simulation, which allowed WRF to modulate the synoptic features provided by GFS and correct some of their errors. This is usually a gain in areas where the climate change signal is sturdily influenced by advective

methods (Heikkila *et al*., 2011). Such a setup will intensify the independence of the

RCM from the driving GCM.
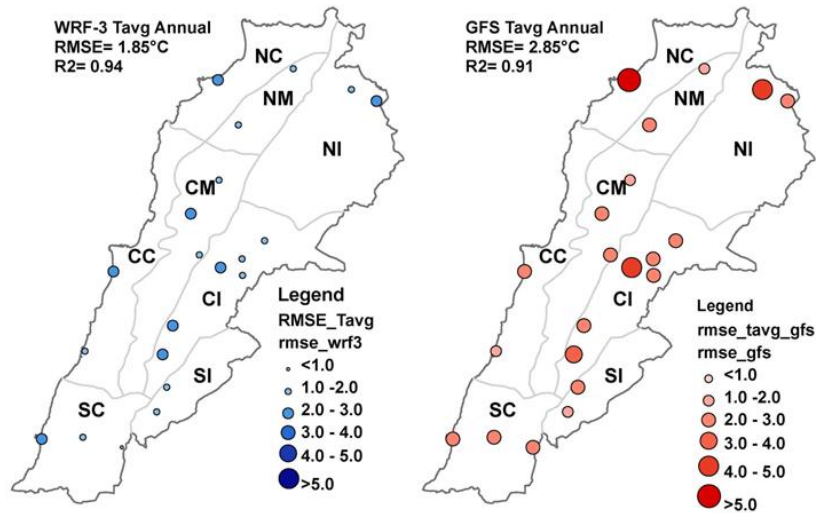
Fig. 3.3. Regional yearly distribution RMSE (ºC) for daily average 2m temperatures for years 2003 and 2010 combined. The values provided in the top-left corners are combined for all stations.

In comparison to GFS-Reanalysis, WRF shows improvements in the

reproduction of the annual cycle of the average daily temperature as shown in Fig. 3.4.

WRF is able to partially correct the largest biases in GFS, for example between days

150 and 270 in 2003. Also in 2010, WRF captures the higher extremes of the average

daily temperature that are underestimated by GFS. Average minimum temperatures are

also captured more accurately by WRF (not shown here) over the study area; although

WRF tends to produce cold-biased average temperatures during the summer, it is still an

improvement over GFS.
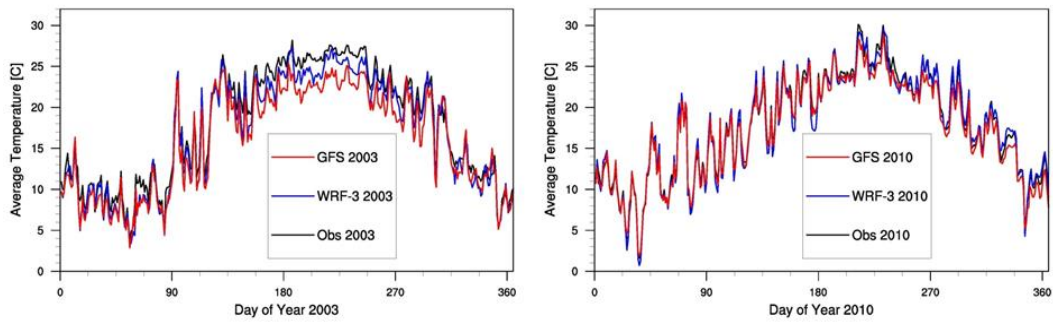
Fig. 3.4. Daily-averaged 2m temperature from WRF and GFS simulation for years 2003 and 2010

3.3.1.2 Maximum Temperatures Tmax

Annual daily maximum temperature from WRF simulations for 2003 and 2010 are presented in Fig. 3.5 differentiating the coastal effects and localized orographic features that include the clear signature of the two mountain chains in the east and west as well as the warmer regions at low altitudes and inland. A strong gradient of more than 12°C in Tmax exists between the highest west mountain range and the coastal and inland regions. Again, a significant increase in Tmax is observed in 2010 compared to 2003, particularly along the southern coast and inland. Also notice the drastic increase in Tmax to the east of the study area (in Syria) in 2010 compared to 2003.
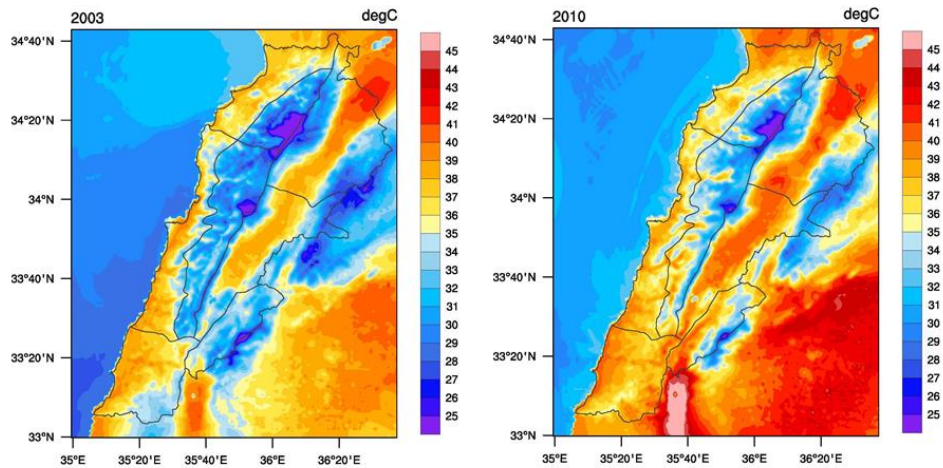
Fig. 3.5. Maximum 2m temperature from WRF simulation for 2003 and 2010

The spatial distributions of RMSE based on Tmax for the summer season (June-July-August JJA) of years 2003 and 2010, calculated from the daily differences between GFS and WRF and observational data, are depicted in Fig. 3.6. On average, WRF yields significantly smaller RMSEs than the GFS, with the majority of the RMSE values slightly over 5°C, while the RMSEs of GFS-Reanalysis exceed 9°C in one station (HAO) in CI region. The geographical pattern of Tmax RMSE for both 2003 and 2010 reveals GFS lacks in the portrayal of Tmax, and the improved performance of WRF, where the driving model RMSE is greatly reduced by the downscaling. GFS has high biases for some regions for both 2003 (eg. MBE for NC is -5.75°C) and 2010 (MBE for NC is -6.14°C), while WRF is significantly reducing these error statistics to less than 2.5°C for both simulation periods (2003: MBE for NC is -2.25°C, and 2010: MBE for NC is -1.63°C).
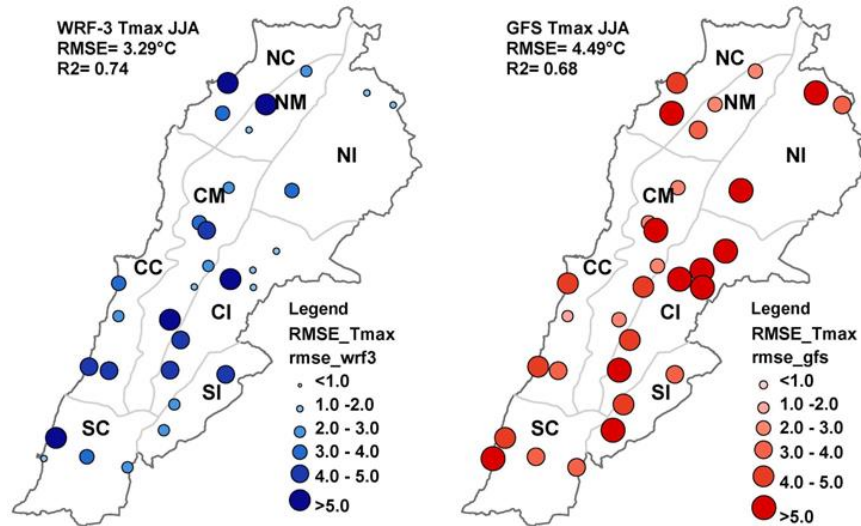
Fig. 3.6. Regional distribution of RMSE (ºC) for summer season daily maximum 2m temperatures for 2003 and 2010 combined. The values provided in the top-left corners are combined for all stations.

The PDFs of daily maximum temperatures for the 2003 and 2010 summer season, comparing WRF and GFS simulations to observations, are depicted in Fig. 3.7. The summer season is normally defined as JJA, but for the computation of these PDFs we opted to include the month of May (M) in the summer season because early in May the Khamsin wind blows up the Levantine coast from the Sahara Desert and could yield high Tmax values. The temperature of the wind can sometimes exceed 40°C, bringing a heat wave over the study area (Blanchet,1965). The added value of WRF can be easily detected in the PDFs of MJJA of 2003 and 2010, where WRF is closer to observations than GFS. During this hot season, the Tmax frequency between 18 and 30°C is overestimated by GFS resulting in underestimation in the hotter bins over 30°C.This misrepresentation is reduced by WRF at the higher resolution whereby the observed hot season PDF is better captured.
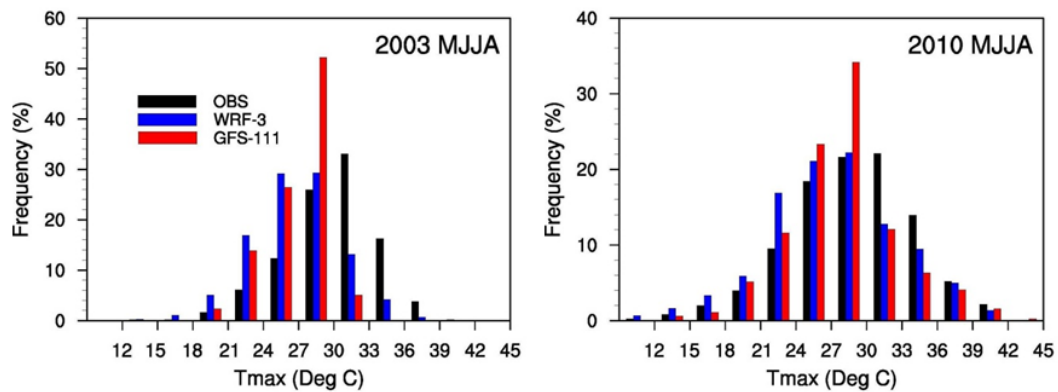
Fig. 3.7. Probability density plots of the daily maximum 2m temperature.

A regional illustration of climate indices is presented in Table 3.1 and Table 3.2 where observed and simulated summer and hot days are summarized for the 8 regions. Both GFS and WRF under-predict the number of summer days for all regions in 2003, but WRF yields much closer numbers to observations in general. In 2010, the predicted summer days in WRF were close to observations in all regions except the central mountain, where GFS performed better and under-predicted the number of summer days by only 4%. As for the hot days, WRF outperformed GFS in both years: the latter practically missed these records for 2003, whereas in 2010 it over-predicted this number by more than two folds in the inland regions. Also the observations reveal a large frequency of hot days inland (CI, NI and SI) during 2003 and 2010; this frequency was clearly captured by WRF but misrepresented in GFS. Another trend that is revealed by these tables is that both models performed significantly better in capturing high temperature extremes during the hot year (2010) compared to the colder year (2003).

Table 3.1. Number of Summer Days (Tmax >25°C) for 2003 and 2010

Region	2003			2010		
	Obs.	WRF-3	GFS-111	Obs.	WRF-3	GFS-111
NC	191	168	131	208	174	108
CC	205	156	144	206	168	155
SC	213	159	161	162	146	153
NM	163	43	131	83	61	108
CM	139	44	131	134	74	108
NI	188	159	131	188	186	192
CI	186	168	131	215	168	124
SI	164	74	129	194	159	219

Table 3.2. Number of Hot Days (Tmax >35°C) for 2003 and 2010

Region	2003			2010		
	Obs.	WRF-3	GFS-111	Obs.	WRF-3	GFS-111
NC	9	3	0	5	1	0
CC	6	2	0	2	0	0
SC	10	4	0	3	0	0
NM	0	0	0	5	0	0
CM	0	0	0	6	0	0
NI	60	10	0	41	51	67
CI	24	10	0	56	33	0
SI	1	0	0	18	8	56

3.3.1.3 Minimum Temperatures

Annual daily minimum temperature from WRF simulations for 2003 and 2010 are presented in Fig. 3.8. The most noticeable contrasts are related to the coastal effects and the mountains where Tmin ranges from a few ºC above zero on the littoral, to −5°C inland and up to −15°C in the high mountains. The difference between Tmin in 2003 and 2010 is most visible in the mountainous areas, while the coastal zones have average minimal temperatures closer to 5°C in both years. Interestingly, the minimum

temperatures are lower in 2010 despite the fact that it was the hotter year on average but had a much wider inter-seasonal variability than 2003.
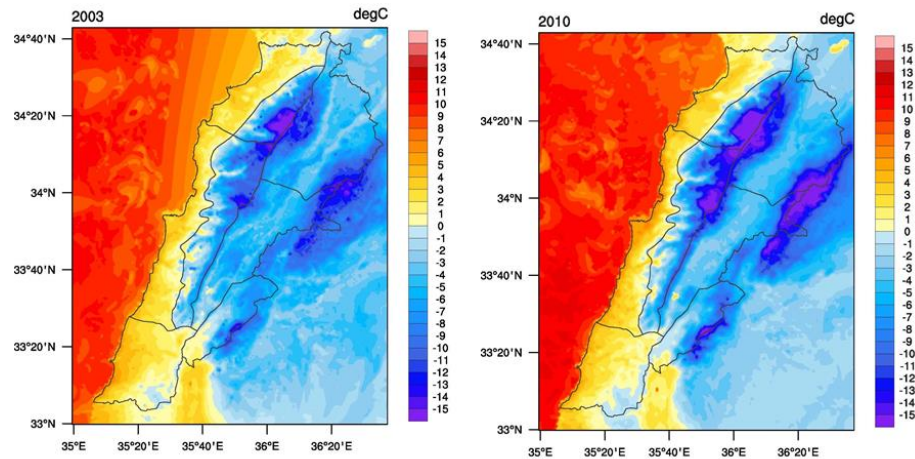
Fig. 3.8. Minimum 2m temperature from WRF runs for 2003 and 2010.

The spatial distributions of Tmin RMSE for the winter season (December-January-February DJF) of years 2003 and 2010 were computed from the daily minimum values between model simulations (GFS and WRF) and point observations (Fig. 3.9). At the yearly level, the degree of agreement of WRF with surface observations is satisfactory, giving an RMSE of 2.61°C for WRF in 2003 against 3.68°C for the GFS and a modest improvement in 2010 from an RMSE of 3.39°C for GFS to a 2.93°C for WRF. WRF reduces the errors in 2003 at all stations except one in the central mountain, the same station that resulted in large discrepancies in the Tmax analysis for 2003, which might indicate errors in temperature measurement although we cannot ascertain this.
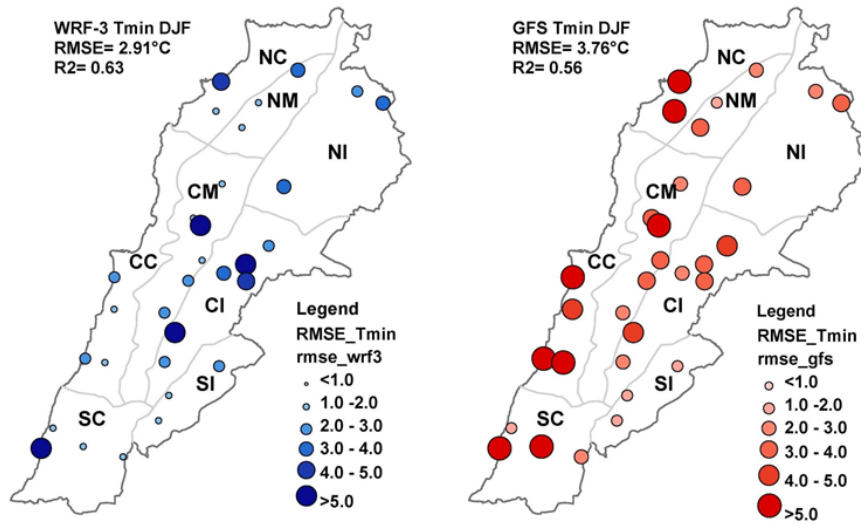
Fig. 3.9. Regional distribution of RMSE (ºC) for winter season daily minimum 2m temperatures for 2003 and 2010 combined. The values provided in the top-left corners are combined for all stations.

Table 3.3 presents the number frost days (FD) from models and observations for the different regions for both years. Observations confirm that the areas with the most FD are concentrated in the mountains and inland. Overall, GFS has difficulties in capturing this climate index, while WRF is yielding better predictions in almost all remaining regions (except SI in 2010). WRF represents the spatial extent of FD reasonably well around all regions in 2003, but the index is generally under-predicted. The improvement associated with the higher-resolution WRF simulations allows for more accurate representation of the local conditions contributing to frost conditions, such as topography, as clearly seen for 2010.

Table 3.3. Number of Frost Days for 2003 and 2010

Region	2003			2010		
	Obs.	WRF-3	GFS-111	Obs.	WRF-3	GFS-111
NC	0	0	4	0	0	5
CC	0	0	0	0	0	0
SC	0	0	0	1	1	1
NM	0	5	4	12	9	10
CM	43	51	4	20	14	6
NI	32	26	4	7	8	6
CI	31	21	4	33	8	6
SI	3	6	0	5	5	1

The assessment of daily variability and extremes are shown in Fig. 10 with the frequency distributions of Tmin. Generally, the agreement between WRF and observed minimums is satisfying in the winter of 2003 and marks an improvements compared to GFS. In the winter of 2010, WRF was closer to observations than GFS in more than half the bins. The WRF simulated distribution of minimum temperatures is skewed to the right in DFJ 2010, showing that the model is overestimating the temperature of the daily minima and thus underestimating the probability of colder minima. GFS overestimates the occurrence of the most likely minimum temperatures of the winter season (5 <Tmin ≤10°C). The correlation values are lower than those of maximum temperatures, a finding that is consistent with similar regional climate simulations (Zhang *et al*., 2009; Soares *et al*., 2012, Andrys *et al*., 2015).
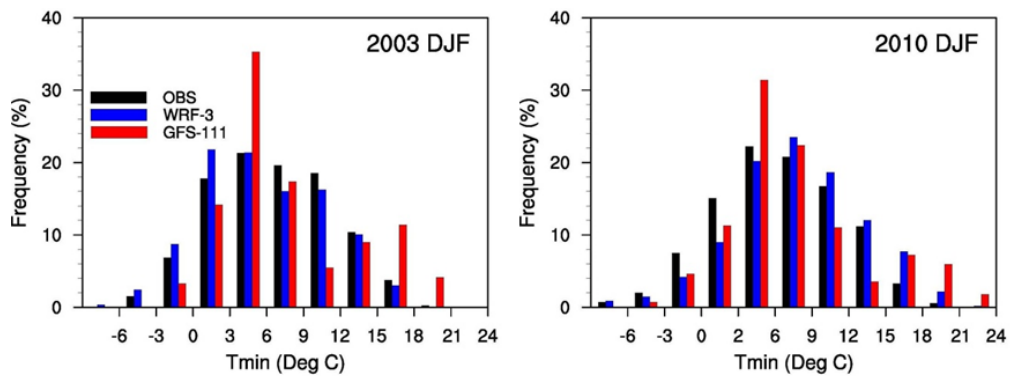
Fig. 3.10. Probability density plots of the winter season daily minimum 2m temperature

3.3.2 *Precipitation*

The average annual rainfall on the coastal zones varies between 700 and 1000 mm and increases from South to North due to the increase in the mountain heights producing the orographic precipitation (Atlas Climatique du Liban, 1977). The West Mountain range forms a barrier against the rain movement and the precipitations in that region can reach more than 1400 mm per annum (the majority of which is snow) on the western slopes. This dries up the air masses flowing east, and rainfall decreases rapidly on the eastern slopes of the West Mountain range and registers only 600 mm inland. Rainfall inland varies between 800 mm (southern inland SI) and 200 mm (extreme north-east inland). As for the East Mountain range, rainfall is around 600 mm and can increase up to more than 1000 mm in high altitudes. In dry years, precipitation can be as little as 50 percent of the average. As for the number of rainy days, they vary from 80 to 90 days a year, mostly between October and April (AQUASTAT, no date).

Cumulative monthly precipitation was computed for every station and its nearest WRF grid point (Argüeso *et al*., 2012), the bias was then computed as a percentage difference between the simulated and observed yearly total accumulated

precipitation for each station separately, and then averaged over the whole study area (Fig. 3.11) for both years 2003 and 2010. The computation of the bias and the temporal averaging are necessary for rainfall due to the chaotic dynamics of precipitating storms: it is very challenging to capture the spatial and temporal dynamics of rainfall events exactly (Li *et al.*, 2013), but the total rainfall should be reproduced accurately if the thermodynamic state of the atmosphere over a given location is captured well by the model. We reiterate the precipitation data from GFS were not available. The overall bias and coefficient of determination between WRF and the observational data were calculated by pooling all stations together without regionalization. With respect to the overall study area, the adopted 3km fine resolution yields small biases, especially in the dry year 2010. Biases of the 9km domain were much larger (Chapter 2), which suggests that WRF produces improved results compared to coarser GCMs when used for predicting dry conditions for future climate change impact studies. More fundamentally, GCMs will face difficulties in reproducing orographic precipitation over such complex terrain since they cannot capture the orography well to start with. Annual differences in precipitation provide an idea of the areas where rainfall is generally over- or underestimated. WRF tends to perform quite well except for over-prediction in regions of high topography in the northern and central mountains and some coastal (CC) and interior regions (SI), although the error here is actually rather small. The coefficient of determination reflects the phase of the precipitation events, and the representation of these events by WRF in 2010 is better than 2003, although the difference in R^2 is minimal (0.02).
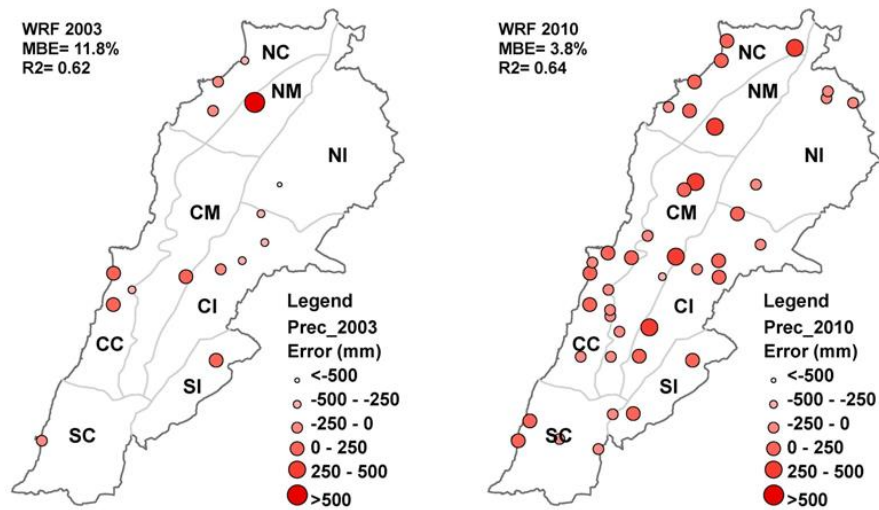
Fig. 3.11. Annual precipitation from WRF-1 for 2003 and 2010

The precipitation in the study area is mainly concentrated in short rain events
and shows an explicit annual cycle with very dry summers. Hence, it is imperative for
the WRF simulations to reproduce the higher end of the precipitation quantiles that
might lead to floods and droughts. To account for the rainy season extreme events, we
apply a filter so that dry days from May to September at all locations are removed,
retaining only those days when the precipitation was larger than a minimum threshold
of 0.2mm/day as defined by the local National Meteorological Service. Fig. 3.12 shows
the resulting quantiles from 50 to 95 percent of the daily mean precipitation simulated
with WRF and compared with the observations for the eight regions for the rainy season
(October to May) of years 2003 and 2010. During both years, the quantiles emphasize
the ability of WRF to capture extreme precipitation events, both in values and high
ranking quantiles, indicating that fine scale parameterizations set in the RCM can reduce
the potentially large biases in the forcing model. WRF overestimates the occurrence of
high quantiles in the coastal zones (Fig. 3.12a) as well as on the mountainous area

(Fig. 3.12b), while it underestimates their prevalence inland (Fig. 3.12c). The overall

distribution of rainfall quantiles is simulated well inland (NI and CI) (Fig. 3.12c), albeit

with a tendency to underestimate their probability at most ranks (50% to 95%).

Likewise, WRF is largely able to capture topographic effects on ranks (days of rainfall

with 95%), particularly over mountainous regions (Fig. 3.12b). This feature distinctly

demonstrates the advantages of using high resolution RCMs, primarily in terms of

precipitation extremes.
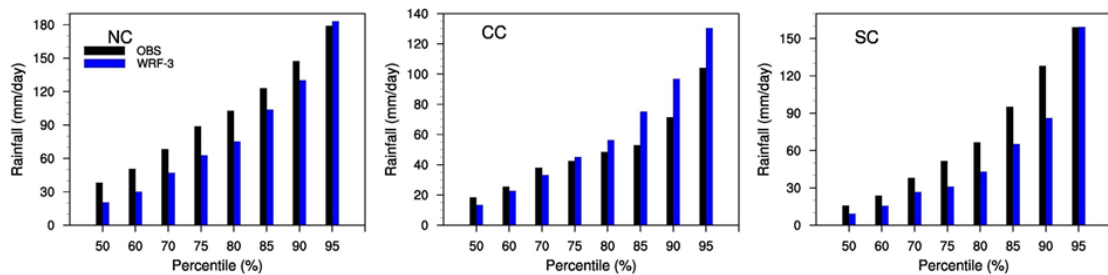
a. Northern, central and southern coastal regions
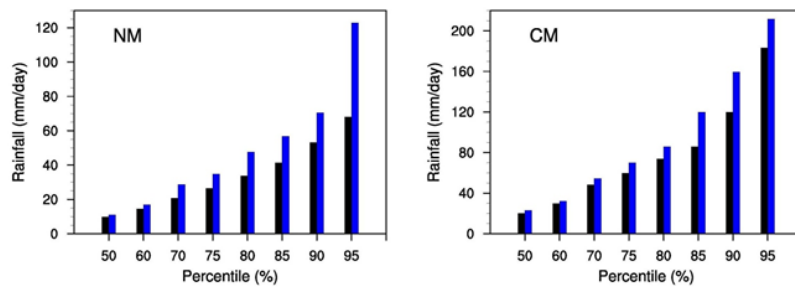
b. Northern and central mountainous
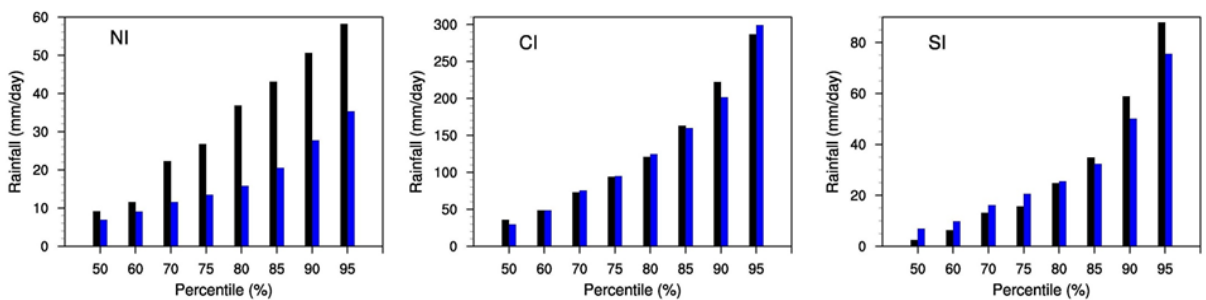
c. Northern, central and southern inland regions

Fig. 3.12. Quantiles of averaged daily precipitation for 2003 and 2010

Most rain events in the study area are sparse convective or orographic events of limited spatial extent, and this type of Mediterranean climate precipitation has been found to be challenging for WRF to simulate well (Soares *et al*., 2012; Andrys *et al*., 2015). The skill of WRF in simulating the number of rainy days (NRD) (>0.2 mm/day), the maximum rainfall intensity (MI), and the longest wet period (LWP) of successive rainy days for the different regions was therefore examined (Table 3.4). Data for the number of rainy days would suggest that WRF compares better in 2010 than in 2003. However, the differences are minor and within the range of observational uncertainty and the two years yield very similar results.

Table 3.4. Precipitation indices for years 2003 and 2010

Region	2003 Obs.			2003 WRF			2010 Obs.			2010 WRF		
	NRD (days)	MI mm/hr	LWP (days)	NRD (days)	MI mm/hr	LWP (days)	NRD (days)	MI mm/hr	LWP (days)	NRD (days)	MI mm/hr	LWP (days)
NC	98	3.75	17	105	0.34	21	55	1.63	5	71	1.10	6
CC	125	2.70	14	111	2.50	10	44	2.18	5	77	2.45	5
SC	60	2.43	10	96	1.28	10	108	3.44	10	91	1.19	10
NM	112	2.79	12	134	4.15	21	100	2.88	10	105	2.04	9
CM	214	3.43	12	124	5.17	10	75	3.66	12	98	1.89	11
NI	68	2.17	17	69	0.66	6	69	1.14	5	45	0.12	7
CI	154	2.20	53[*]	81	0.94	10	85	2.53	11	59	0.98	9
SI	41	1.66	5	101	3.62	10	84	3.23	10	68	5.58	6
Avg	109			103			78			77		

[*] *This observed LWP number is unrealistic for the CI region or any region, and must be due to an observation error.*

Generally, WRF is able to capture the number of rainy days in each year quite well, as well as the large differences in the number of rainy days between 2003 and 2010. In what concerns the distribution of rainfall maximum intensity, WRF underestimates the intensity in the coastal areas as well as in the northern and central

inlands, but magnifies it in the southern inland region. As before, the topography plays an important role in these distributions. Orography plays also a significant role in mountainous regions that cannot be captured by coarse GCMs, where WRF is exhibiting opposing trends with overestimates of the intensity in 2003 and underestimates in 2010. The longest wet periods are also captured by WRF reasonably well; we note that the large error in the longest wet period in 2003 in central inland is highly likely due to observational errors since the number of 53 consecutive rainy days seems unrealistic for that region.

3.4   Summary and Conclusion

Temperature and precipitation represent the most important elements for climate applications, and are usually required at high spatial and temporal resolution when evaluating the environmental and socio-economic impacts of climate change. Dependable information at high resolution cannot be directly obtained via global climate hence model data is first downscaled to be correctly applied for impact mitigation endeavors. In this chapter, we sought to answer the question: Can high resolution dynamical downscaling improve the representation of climatic extremes over a complex terrain? To that end, an assessment of WRF as an RCM forced by the GFS-Reanalysis was conducted over a complex topography domain along the Eastern Mediterranean for a wet year (2003) and a dry and hot year (2010) to examine its capability, compared to its driving global model, to capture the temperature and precipitation of extreme events as a prerequisite to the preparation of high-resolution climate impact scenarios.

The serial and spatial spreading of the average temperature over the study area were well captured in the WRF simulations, compared to the driving GFS-Reanalysis, due to the improved resolution of the topography that generated more accurate mesoscale patterns at higher horizontal model resolution. Extreme temperature indices were simulated well by WRF, which was able to represent the magnitude as well as the spatial and temporal distribution of summer and hot days. Summer season RMSEs for the maximum 2m temperature are enhanced by WRF by more than 1°C when related with GFS-Reanalysis. Regarding minimum temperatures, the performance of WRF is better in 2003 than in 2010, where the reduction in RMSE compared to GFS-Reanalysis is smaller. As for the frost days (FD) extreme index, GFS-Reanalysis has difficulties to skilfully describe this climate index, while WRF exhibits significantly lower error.

The overall distribution of rainfall is simulated well, and the matching of the higher-ranking quantiles as well as the observed frequency of wet days is satisfactory. While GFS rainfall data was not available for comparison, GCMs such as the one GFS is based on will face difficulties in reproducing precipitation over a complex terrain since they cannot capture the important role of orography.

In closure, the answer to the motivating question of this paper is that dynamic downscaling (at least using WRF) improves the predictions of the driving model over complex terrain even though it cannot completely correct some of its biases. This improvements apply to the averages, as well as to the extremes that are critical for assessing climate change impacts since they affect ecohydrolgical systems as well as many socio-economic sectors such as water and agriculture.

CHAPTER 4

FUTURE INTENSIFICATION OF HYDRO-METEOROLOGICAL EXTREMES: DOWNSCALING USING THE WEATHER RESEARCH AND FORECAST MODEL

4.1   Introduction

In recent years, various regions have witnessed seasonal weather changes that were associated with negative environmental impacts and that led to socio-economic burdens across many countries. In addition, recent research indicates potentially greater changes in regional weather under future climate conditions (Sun *et al*., 2007; Brown *et al*., 2008; IPCC, 2013). In particular, climate change has been reported to intervene with the frequency and intensity of extreme events (Christidis *et al*, 2005). Examples of such events are heatwaves, droughts, and floods that have adverse effects on important aspects of our society and economy, such as water resources, crop yield, and human health (Seneviratne *et al*., 2014). Therefore, understanding the vulnerability to climate change, and corresponding mitigation measures and adaptation strategies to potential negative impacts, became imperative at both regional and local levels. This is particularly important in order to capture extremes that are highly variable in space and time and are not adequately simulated by global climate models (GCMs). This necessitates the use of regional climate models (RCMs) to downscale the large-scale forecasts from GCMs (Barrera-Escoda *et al*., 2014). Downscaling is particularly needed in regions with complex topographies that cannot be resolved by coarse GCMs.

Downscaling can be conducted through various techniques that can be mainly categorized into two groups known as dynamic and statistical downscaling (Evans *et al*., 2012). The latter generates semi-empirical relationships between local and large-scale climate based on statistical methods (Wilby *et al*., 1998; Flaounas *et al*., 2013b). It requires less computational power but is constrained by the hypothesis of stationarity in the associations between local observations and simulated climate, which are developed for the present and then applied in a future variable climate (Diaz-Nieto and Wilby, 2005). Dynamic downscaling, used in this study, consists of driving an RCM at high resolution by the output of an atmospheric high resolution GCM for the region of interest (Wang *et al*., 2004). They produce an accurate regional climate with fine-scale topographies that are lacking in the GCMs (Antic *et al*., 2004). Dynamic downscaling is computationally demanding and needs substantial implementation effort, but a crucial appeal of the technique is the reliance on physical processes rather than statistical relationships, relaxing the need for assuming stationarity (Fowler *et al*., 2007). The high resolution over a limited region permits improved depiction of basic surface forcings such as topography, shorelines, inland water or land-surface features and heterogeneity (Giorgi and Mearns, 1991).

Some recent RCM downscaling studies attempted to examine the change in the mean and extreme climate variables (temperature, precipitation, etc.) (Cardoso *et al*., 2012; Gao *et al*., 2012; Warrach-Sagi *et al*., 2013). These parameters can be highly affected by regional variability, especially in regions with complex topography. The use of high-resolution RCMs in such intricate domains usually improves the average annual precipitation and mean temperatures fields in comparison with the driving GCM when simulations are conducted over a time span of multiple consecutive years (Salathé *et al*.,

2008; Caldwell *et al*., 2009), but their added value for capturing extremes is not well documented. In addition, when the grids of RCMs become finer than 10km, which is needed over complex terrain but necessitate smaller time–steps, the simulations become very demanding computationally with little to no feasibility to perform downscaling for multiple decades that are usually simulated by GCMs. Therefore, increased spatial resolution invariably comes with the caveat of reduced temporal (as well as spatial) coverage. If the aim is to understand the vulnerability of a region to climate change, one must therefore judiciously select future periods to downscale using RCMs. These two challenges, namely the complex topography requiring dynamic downscaling and the need to select carefully future periods to downscale, frame the scope of this chapter. Such challenges are eminently represented in the eastern Mediterranean basin where temperature and precipitation are sensitive to orographic elevation changes that occur at spatial scales much smaller than the grid scale of a GCM. Furthermore, weather and climate variability on weekly to yearly scales implies that severe adverse impacts of climate change are localized in time, which implies that the periods when such impacts occur need to be identified for downscaling based on GCM data.

This chapter aims to assess the value, and investigate the challenges, of regional dynamic downscaling in topographical complex regions during extreme periods. As a pilot area, we selected the country of Lebanon. With its location in the temperate zone along the eastern Mediterranean and its complex topography where two mountain ranges run parallel to the coast and amplify the impact of the Mediterranean Sea on the climatology of the coastal and interior regions (Atlas Climatique du Liban, 1977). It is a representative example of a location where dynamic downscaling is expected to be challenging, yet valuable. The objectives of this chapter are (1) to

propose a method whereby only extreme years are identified and selected for downscaling to gage the worst-case impacts (in this chapter we focus on dry and hot years) of climate change; (2) to dynamically downscale global climate predictions for these extreme years to a local scale using the Weather Research and Forecasting (WRF) model (Skamarock *et al*., 2008) forced by the High Resolution Atmospheric Model (HiRAM) (Zhao *et al*., 2009; Jiang *et al*., 2012) for the past (as a reference) and the future; and (3) to generate information on the small-scale spatial variability of vulnerability that cannot be captured by coarse GCM simulations. The novelty of the contribution centers on 1) the selection of "crucial-periods" for targeted downscaling using anomaly scores that can be defined to reflect any variable of interest, and 2) the focus on the value of downscaling for capturing extremes and corresponding statistics as proxies for the magnitude of the most severe climate change impacts. Beyond methodological contributions, the implications of the results on water resources are valuable given that the overall region is already water stressed and continues to suffer from socio-political conflicts coupled with a lack of integrated water management policies (Bou-Zeid and El-Fadel, 2002).

4.2   Methods and Data

4.2.1   Global Model

HiRAM is a global atmospheric model that was developed by the Geophysical Fluid Dynamics Laboratory (GFDL) to be applicable to a broad range of resolutions (Chen and Lin, 2011). It was developed based on the standard version of GFDL atmospheric GCM (AM2) (Zhao *et al*., 2009) with 32 vertical levels (instead of the 24 levels in AM2) to provide refined vertical resolution particularly near the tropopause

(Jiang *et al*., 2012). HiRAM also uses a cubed-sphere application of a finite-volume dynamic core and is linked to GFDLS's new land model (LM3) (Donner *et al*., 2011).

The model has been used in studies of hurricane inter-annual variability, multi-decadal trends, responses to 21st-century warming, and seasonal hurricane predictions for the North Atlantic and East Pacific (Zhao and Held, 2010; Zhao *et al*., 2010; Jiang *et al*., 2012). Gall *et al*., (2011) investigated its potential as a forecasting tool for the near-term and for intra-seasonal hindcasting of tropical cyclones in the Atlantic basin from 2006 to 2009, demonstrating skilled near-term forecasts of cyclones track and intensity about their respective benchmarks. Another study by Chen and Lin (2011) used HiRAM to predict the tropical cyclone activity in the North Atlantic basin at 25 km resolution and reported a high correlation coefficient (R2) of 0.96 between observed and simulated hurricane counts for the 2000-2010 seasons.

In this study, HiRAM is used at a horizontal grid spacing of 25 km (Bangalath and Stenchikov, 2015) to simulate historic (1975-2004) and future (2007-2050) stages using both Representative Concentration Pathways (RCP) 4.5 and 8.5 scenarios[2]. The Sea Surface Temperatures, completed for the International Panel for Climate Change Assessment Report AR5 project, were adopted from the GFDL Earth System Model runs as the bottom boundary conditions over water surfaces. Recommended time-varying greenhouse gas and stratospheric/tropospheric aerosol distribution datasets were used to reproduce the observed radiative forcing in the model (Bangalath and Stenchikov, 2015).

---

[2] RCP 4.5 reflects a stabilization scenario where total radiative forcing plateaus before 2100 by the utilization of a variety of technologies and strategies for reducing GHG emissions (Clarke et al. 2006). As for RCP 8.5, it is characterized by increasing GHG emissions over time, leading to high GHG concentrations (IPCC 2013).

To evaluate the selected driving GCM (HiRAM), data from five other global models selected to have a range of resolutions (Table 4.1) forced by RCP4.5 and 8.5 were obtained from the Coupled Model Intercomparison Project phase 5 (CMIP5) archive (https://pcmdi9.llnl.gov/projects/esgf-llnl/) (Taylor *et al*., 2012). Then, yearly median temperature and annual accumulated precipitation time series over Lebanon (which is smaller than one grid cell in all models except HiRAM) were generated for each GCM for the period 2007-2050 to compare their simulated average decadal climatology in the study region for both scenarios. The median, minimum and maximum values for each decade GCM of the yearly averaged temperature and yearly accumulated precipitation are compared in Fig. 4.1. HiRAM has the highest resolution (25km) of all models used and its predicted precipitation for the past period 2007-2010 is the closest to the average annual precipitation of 700 to 800mm in the study area (Atlas Climatique du Liban, 1977). The decreasing precipitation trend in HIRAM for the future is more pronounced than the other models. The lower resolution models produce lower rainfall for 2007-2010, which might be expected given their limitation in resolving the complex topography in the study area that plays a significant role in inducing orographic precipitation. On the other hand, HIRAM has a cold bias for the median annual temperature (for 2007-2010) for both RCPs, whereas HadGEM2-AO and CCSM4 produce the ≈20°C mean temperature over the study area (Atlas Climatique du Liban, 1977) more accurately. We opted for HiRAM forcing to drive WRF in this study because 1) our simulations suggest that WRF can correct some of the temperature biases it inherits from its forcing model (Chapter 3) and therfore the cold bias of HiRAM is less of a concern, 2) the focus is primarily on precipitation and on the hydrologic impacts of climate change that are captured well by HiRAM, and 3) the high resolution

of HiRAM allows a start with a coarse grid of 9 km in WRF (rather than 27 km for example). However, we note that demonstrating a higher performance of a GCM in simulating present-day climate may not be a sufficient indicator of the performance for future climate (Christetin and Christenin, 2007); this is a limitation that cannot be overcome. Moreover, to further reduce the impact of GCM bias on climatic trends, we select the historic baseline for the hot and dry year from the RCP4.5 simulation of HiRAM to assess future climates trends, instead of relying on observations or reanalyses.

Table 4.1. Global climate models assessed, in order of decreasing resolution.
Note that the area of the study area is 10,452 km^2, which implies that HiRAM is the only GCM that has more than one grid cell over the country

Model Name	Institution	Horizontal Grid	Reference
GFDL-HiRAM-C360	NOAA Geophysical Fluid Dynamics Laboratory	25km × 25km	Delworth *et al.*, 2006; Donner *et al.*, 2011
CCSM4	US National Centre for Atmospheric Research	100km × 117km	Gent *et al.*, 2011
HadGEM2-AO	National Institute of Meteorological Research/ Korea Meteorological Administration	208km × 117km	Collins *et al.*, 2011; Martin *et al.*, 2011
INM-CM4	Russian Institute for Numerical Mathematics	222km × 140km	Volodin *et al.*, 2010
MRI-CGCM3	Meteorological Research Institute	320km × 160km	Yukimoto *et al.*, 2011
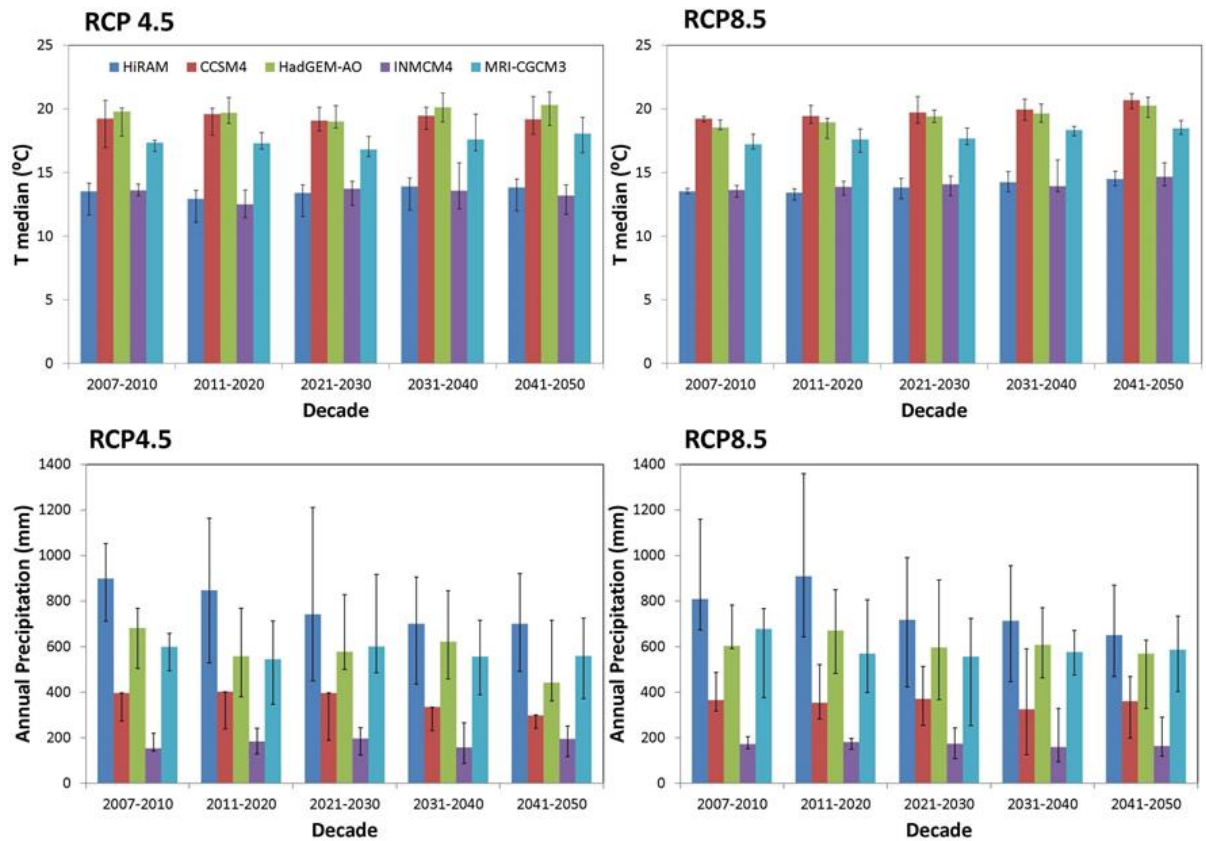
Fig. 4.1. Average decadal climatology over study area from five GCMs.
(up: yearly median, minimum and maximum temperature for every GCM during each
decade; down: yearly accumulated, minimum and maximum precipitation for every
GCM during each decade)

4.2.2 *Regional Model*

The regional model used for this study is WRF, with the Advanced Research
(ARW) dynamics solver, version 3.4.1 (Skamarock *et al*., 2008). WRF is a non-
hydrostatic three-dimensional atmospheric model suitable for both operational
forecasting and atmospheric research applications (Heikkila *et al*., 2011). It accesses
various databases directly to obtain information on terrain elevation, land cover and land
use from the United States Geological Survey (USGS) and from the Moderate
Resolution Imaging Spectroradiometer (MODIS) (Friedl *et al*., 2001) at various
resolutions. These data cover the whole earth surface at a finest resolution of 30 seconds

in both latitudinal and longitudinal directions, which corresponds to about 1 km at mid-latitudes.

WRF as an RCM was recently evaluated in several studies, which documented very good skill in simulating regional weather and climate (Lo *et al*., 2008; Bukovsky and Karoly, 2009; Caldwell *et al*., 2009; Qian *et al*., 2010; Lebeaupin Brossier *et al*., 2011; Cardoso *et al*., 2012; Talbot *et al*., 2012; Flaounas *et al*., 2013a & b; Warrach-Sagi *et al*., 2013; Ramamurthy *et al*.. 2016). A regional high resolution is achieved in the current simulations by using two one-way nested domains (Fig. 4.2a), with 9 and 3 km horizontal resolutions. The highest resolution of 3km was shown to be sufficient in previous tests comparing historic WRF simulations over the study area to a wide array of ground observations; no significant improvement was noted when the resolution was further increased to 1 km (Chapter 2). The outer integration domain covers 1350 km $\times$ 1700 km encompassing the eastern Mediterranean, to guarantee that synoptic-to-mesoscale systems that affect the coast of the study area are resolved in WRF. The inner domain extends over 462 km$\times$579 km. MODIS (for the year 2001) land use data was used with 21 land categories and Lambert Conformal projection (most convenient for mid-latitude regions since it yields a nearly uniform grid spacing). The time step used was 30 seconds for the largest domain, and all domains had 28 vertical levels (with a vertically-stretched grid) arranged according to terrain following hydrostatic pressure coordinates. The number of vertical levels is also based on the tests for historic periods conducted in Chapter 2.
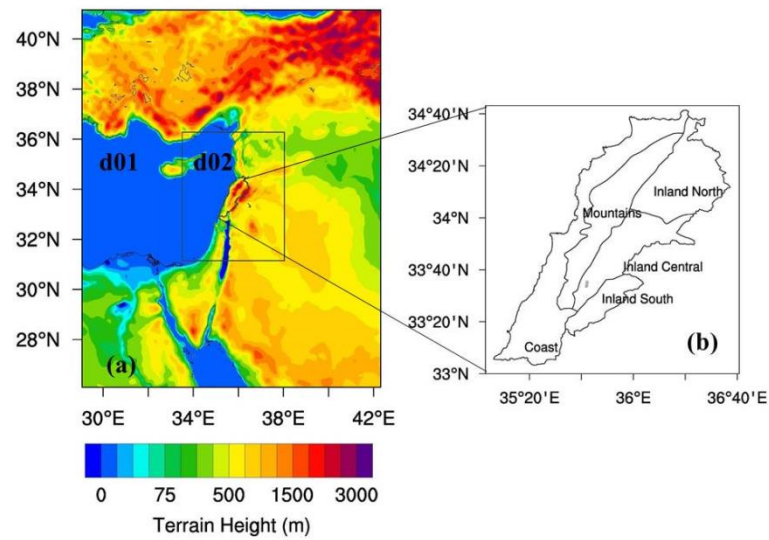
Fig. 4.2. (a) WRF's two domains (9:3km) configuration with a color map of terrain height above sea level (ASL) (m), (b) study area divided into five geo-climatic regions

Initial and boundary conditions were obtained from HiRAM's past and future simulations. The time interval of the boundary data is 6 hours, and the sea surface temperature (SST) was updated every 6 hours. WRF Preprocessing System (WPS) was used to interpolate HiRAM's output into WRF domains. Eight yearly simulations were performed to generate extreme future climate projections over the project area, four from RCP 4.5 and four from RCP 8.5 (one year per decade from each scenario from 2011 to 2050). In addition, two past years (2003 and 2008) forced by HiRAM were also simulated and employed as a baseline scenario to allow for comparison and quantification of changes. Each simulation covered a 13-months physical period, initialized on the first of December of the year preceding the year of interest to allow a one month spin-up period (which was discarded) before the analysed simulation periods, January to December of the year of interest (Zhang *et al*., 2009; Gao *et al*., 2012; Soares *et al*., 2012).

Another key step in the model setup involves selecting the parameterization schemes. In this work, the parameterizations schemes were adopted are: WRF Single-Moment 6-Class Microphysics Scheme (WSM6) (Hong and Lim, 2006), Monin Obukhov and Mellor Yamada Janjic (Eta) for surface layer and PBL physics (Mellor and Yamada, 1974, Janjic, 2001), Rapid Radiative Transfer Model (RRTM) (Mlawer *et al.*, 1997) and Dudhia Long Wave and Short Wave (LW/SW) for radiative processes (Dudhia, 1989), and Noah Land Surface Model (LSM) (Chen and Dudhia, 2001) for surface processes. The selection is based on our previous WRF tests as detailed in Talbot *et al.* (2012) and Li *et al.* (2013). The same WRF configuration used here also performed well in historic simulations over the study area forced by reanalyses data from GFS (Chapters 2 and 3). We modified the atmospheric equivalent CO_2 concentration in each simulated year of WRF to match the respective scenarios RCP4.5 and RCP8.5 and to be consistent with HIRAM. This alters the radiative balance of the simulations slightly but has a minor impact on the relatively short-term regional simulations we conduct with WRF (this was verified by comparing to simulations with current CO_2 concentration).

4.2.3   *Selection of Downscaling Periods*

The influence of global warming on the project area can be assessed by comparing past and future statistics of various meteorological fields from years selected to have extreme hydro-meteorological events such as heat waves, intense storms, or drought periods. Such events pose particular challenges for dynamic models and significant hazards for the affected areas. Therefore, our downscaling simulations do not aim to reproduce decadal-means or average climatological conditions, the trends of

which are reasonably captured by GCM outputs despite their shortcomings. Our focus is rather on extreme years where the impacts are the largest. Since these extreme years will be the tail of the decadal probability distribution functions (PDFs) for the various variables, a pertinent question is how representative are these tails of the general changes in these distributions. To address this question we plot in Fig. 4.3 the PDFs of 2m air temperature at a coastal location near the capital Beirut simulated by HiRAM, for each decade separately. The PDFs depict a consistent monotonic decrease in the frequency of low and intermediate temperatures, and an increase in the frequency of the highest (≥ 25ºC) temperatures. We also computed the mean and standard deviations for all decades and this shift seems to emanate from a shift in the mean, rather than a change in the variance. The figure also indicates that the PDFs, computed based on a decade of daily data, are sufficiently converged so that the changes at the tails are not random, but rather consistent and representative of overall changes in the PDF. This indicates that investigating the tails is justified and indeed beneficial for our purposes since we intend to focus on extreme events.
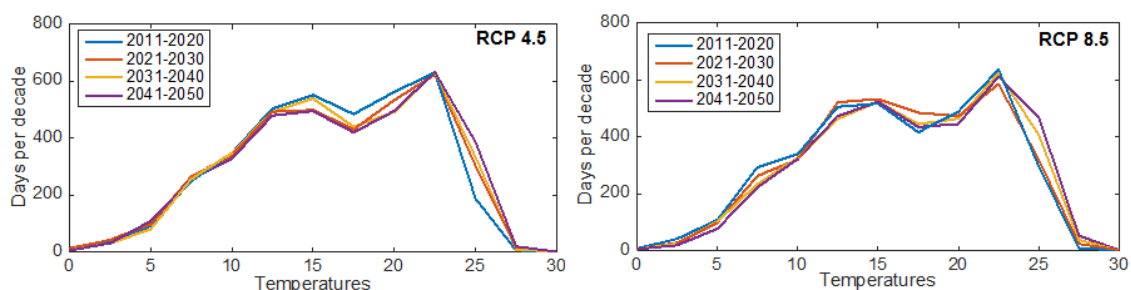
Fig. 4.3. Probability density functions of air temperatures (ºC) at a coastal location near the city of Beirut (BIA station, detailed in section 4.2.4) from the time series of HiRAM, for the 4 future decades.

To identify such extreme years, the following procedure is adopted:

- Analyze HiRAM temperature and precipitation output time series for the "past" (2000-2010) and for the "future" (2011-2050 for RCP 4.5 and 8.5) (Fig. 4.4)

- Quantify the average annual precipitation and the median temperatures for each year from 2000 till 2050.

- Select the two extreme years for the past (a cold and wet year, and a hot and dry year) and eight years in the future (one hot and dry year per scenario per decade) based on the following anomaly score:

$$Anomaly\ Score = \frac{1}{2}\left(\frac{P_i - \langle P_i \rangle}{\max(P_i - \langle P_i \rangle)} + \frac{-(T_i - \langle T_i \rangle)}{\max(T_i - \langle T_i \rangle)}\right),$$

where P_i is the cumulative precipitation for year i (averaged over the domain of interest); $\langle P_i \rangle$ is the decadal-average (e.g. from 2021 to 2030) of the yearly precipitations P_i; T_i is the yearly median temperature (over the domain of interest); and $\langle T_i \rangle$ the decadal-average of the median temperatures T_i.

The domain of interest here was taken as an area of 28917 km^2, spanning multiple HiRAM grid cells and fully containing the country of Lebanon. The resulting minimum negative score will correspond to the critical/worst year of the decade. WRF simulations of historical very wet and very dry years are performed to "measure" the sensitivity of complex regions like the study area to extreme climate variability, although the future simulations focus on hot and dry conditions that will have a more adverse impact in this region.

The above process resulted in the selection of the following years: (1) 2003 as past cold and wet year and 2008 as past hot and dry year; (2) 2020, 2029, 2040 and 2050 as future dry and hot years from RCP4.5; and (3) 2017, 2023, 2035 and 2050 as future dry and hot years from RCP8.5. Fig. 4.4 indicates that the precipitation variability

is larger than the median temperature variability and thus dominated the anomaly score. Another formulation can be adopted (with weight) but in this study we focus on precipitation extremes and as such this score is well suited. It is worthwhile to mention that the anomaly score gave years 2011 in RCP4.5 and 2015 in RCP8.5 as the extreme years for the decade 2011-2020, but we opted not to simulate any additional past or current years other than 2003 and 2008 (although 2011 and 2015 are future years in the HIRAM simulation). Hence, we selected the second worst extreme years (2020 in RCP4.5 and 2017 in RCP8.5). This had some influence on the trends we will show later, but does not alter the conclusions we make.

It is notheworthy that the simulated weather is a possible future realization, and unlikely to be the actual one that is going to occur. Hence, the driest year forecasted by a GCM for the 2030-2040 decade, for example, might not be the actual driest year that will happen in that decade, but should be statistically representative of the actual driest year given that the PDFs seem reasonable converged as illustrated in Fig. 4.3.
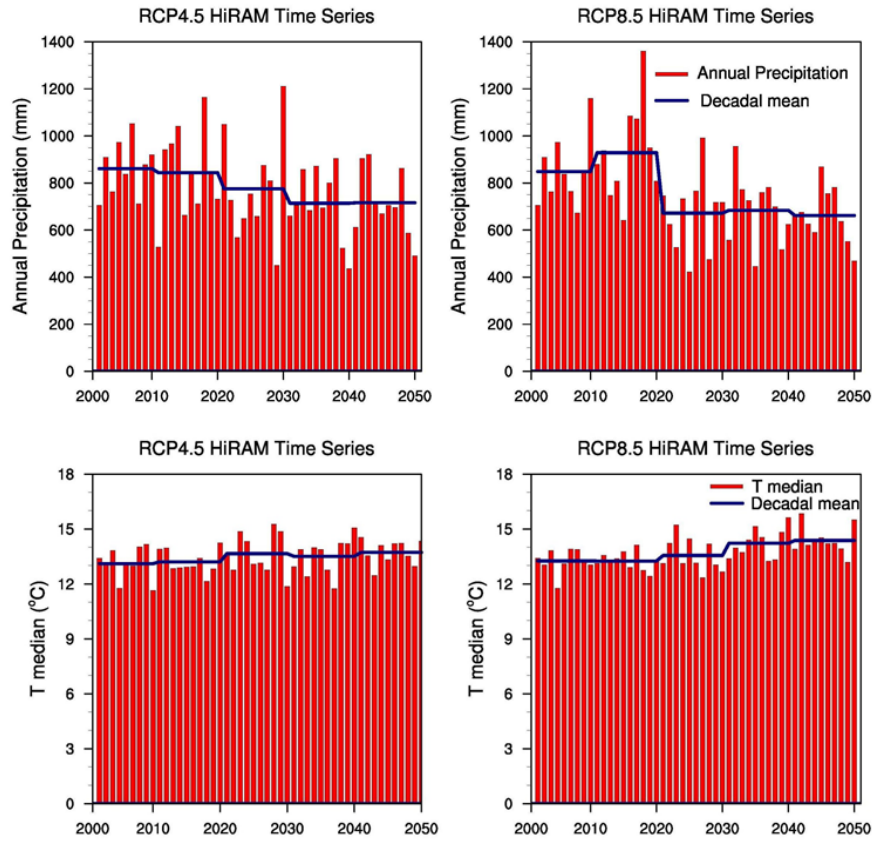
Fig. 4.4. HiRAM RCP4.5 and 8.5 annual cumulative precipitation (mm) and median temperature (^{0} C) time series (2007-2050) over the study area (Lebanon)

4.3 Observational Data

Before using any RCMs or mesoscale models for high-resolution future projections, it is critical that model outputs be assessed against historical observational data to evaluate their consistency in predicting spatial and temporal distributions (Laprise 2008). We assessed the use of WRF forced by meteorological reanalyses from the same region (Chapters 2 and 3), with very satisfactory results. We also perform a limited assessment of HiRAM/WRF in this chapter. To that end, comparisons between simulated and observed 2m temperatures and rainfall climatologies were conducted. WRF dynamical downscaling monthly results for rainfall and temperature from past simulations (2003 and 2008, the two extreme years for that decade according to

HiRAM) are compared with monthly observational datasets from weather stations that have continuous data for the decade of 2000-2010 across the project area. These tests will show if the dominant temporal features (magnitude, spatial pattern, and monthly variations) of rainfall and temperature, and their ranges, are well captured by HiRAM/WRF runs at various spatial locations, and will guarantee that the HiRAM/WRF extreme variability is within the observed variability for historical periods.

To identify the spatial and temporal climatic data that can be used, a review and assessment of the quality, comprehensiveness and span of several climatic data sources was undertaken. Based on a long-term trend of weather parameters including temperature, relative humidity, rainfall and wind, the Atlas Climatique du Liban (1977) divides the project area into three broad climatic trends: the coastal, the mountainous, and the inland, each of which is further subdivided into sub-regions. We found that the subregional divisions are only significant in the present analyses for the inland zone, which is partitioned into the north, central and south sub-regions based on the difference in annual precipitation (Fig. 4.2b). Continuous observations with complete monthly data were assessed from available stations for the five geo-climatic regions. Data were available through the website TuTiempo.net[3]., which compiles and stores data from meteorological stations around the world. Only three stations were found to have continuous daily data for temperature and rainfall for the period 2000-2010, two (BIA and TRP) located along the coastal zone and one located in the central inland region (HAO). Moreover, the anomaly score in equation (1) was used to determine the two past extreme years (wet/cold and dry/hot) in the observational data during the period 2000-

---

[3] http://en.tutiempo.net/climate/lebanon.html

2010 at each of the three stations (BIA, TRP and HAO). The monthly outputs of WRF

and HiRAM are then compared to the observed yearly-averaged temperature and yearly-

accumulated precipitation statistics (average over the decade, minimum, and

maximum), as well as to the same observed variables in the two observational extreme

years. Note that the evaluation did not cover snow fall because no records were

available for this variable in the study area.

4.4   Results and Discussion

The possible influence of climate change on precipitation events in the study

area is inferred by comparing past and future WRF simulations driven by HiRAM. The

climate change signals of the mean values and the seasonal cycles of rainy-season

precipitation will be compared. Finally, we reiterate that in the case of presence of

biases in precipitation from WRF runs, which can originate both from HiRAM and

WRF simulations, one can expect the biases to have a moderate influence on the

difference fields (the trends) since they would be comparable to past and future

HIRAM/WRF runs.

4.4.1   Temperature for Recent Historic Extreme Years (2003 and 2008)

Fig. 4.5 illustrates the annual mean temperature maps during 2003 and 2008 for

the study area resulting from HiRAM and WRF simulations. HiRAM alone identifies

the large-scale distribution of mean annual temperature but misses to reproduce the

local topographies well. The figure obviously replicates the close relationship between

altitude and temperature and shows that the finer resolution WRF simulations are

superior in capturing the temperature changes related to elevation in the mountain

ranges, alongside the coast and in the inland regions. For instance, the northern inland semi-arid region located between two mountain ranges is delineated very well by WRF, while HiRAM's coarse resolution completely misses it. In addition, HiRAM missed many regional details such as the low temperature in the west mountain ranges: the minimum temperature is simulated approximately 0.8° to the east compared to WRF. WRF reproduces the spatial configuration of temperature variability skilfully, as well as the gradient of the temperature variability that is higher at high altitude and lower near sea levels. Therefore, WRF captures the regional temperature differences between the cold (2003) (Fig. 4.5b) and hot (2008) (Fig. 4.5d) simulated extreme years reasonably well.

In order to evaluate the model's skill in capturing the temperature variability over the study area, we calculated the simulated average monthly temperatures (T) (and Precipitations (P) in the next subsection) during 2003 and 2008 for the three weather stations considered, where the model data at the location of each station was used (Fig. 4.5). For observation data of each station, the mean values for each month were averaged over the 11 available years (each month separately, from 2000 till 2010) for observed temperature and accumulated precipitation. The average over a given month across all years, as well as the average for the whole 11 years, were then also calculated. In addition to the monthly average over all years, the maximum and minimum monthly-mean values of T and P were computed for each month over the 11 years from the observations for the whole decade (e.g. hottest July in these 11 years). The simulated monthly mean temperature for 2003 and 2008 were then compared to observed ranges to check if WRF outputs are within these ranges for T and P. As previously noted, the observational data were for the observed extreme years (wet/cold and dry/hot)

determined from the application of the anomaly score to the observational time series

from 2000 to 2010. It is worthwhile to mention that the anomaly score resulted in the

same past observed extreme years at both coastal stations (BIA and TRP) (2009 as

wet/cold year and 2010 as dry/hot year); however, these years were different at the

inland station (HAO) (2002 as wet/cold year and 2008 as dry/hot year).
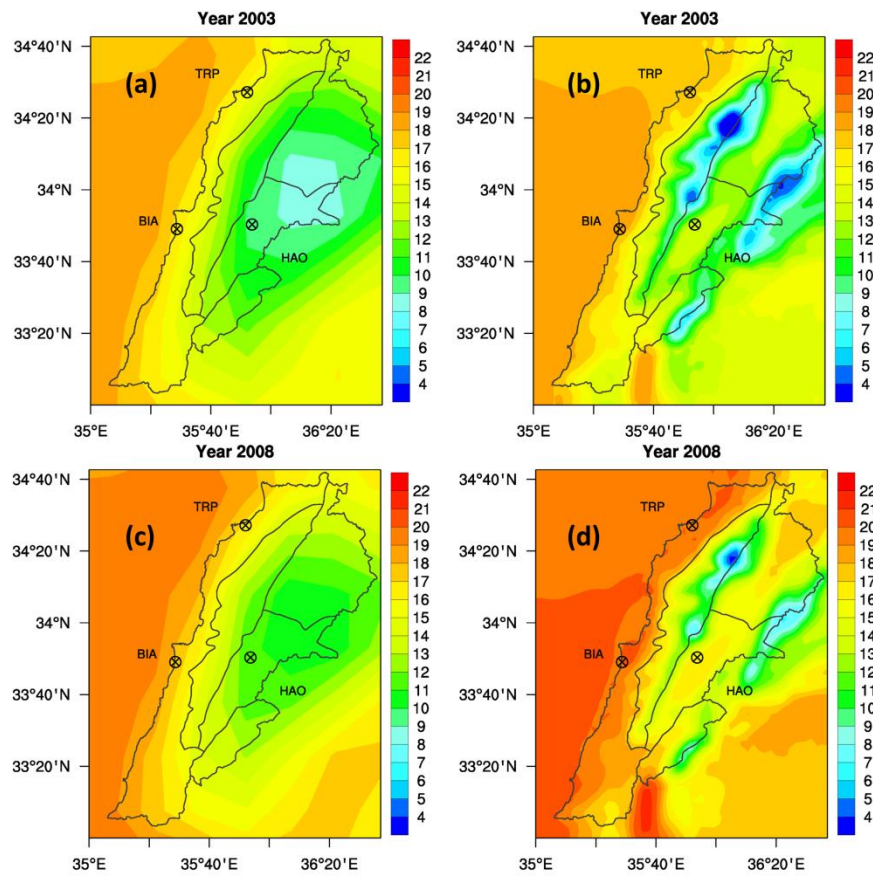
Fig. 4.5. Average yearly 2m temperature (a) 2003 HIRAM;
(b) 2003 WRF3 km resolution; (c) 2008 HiRAM; (d) 2008 WRF 3km resolution
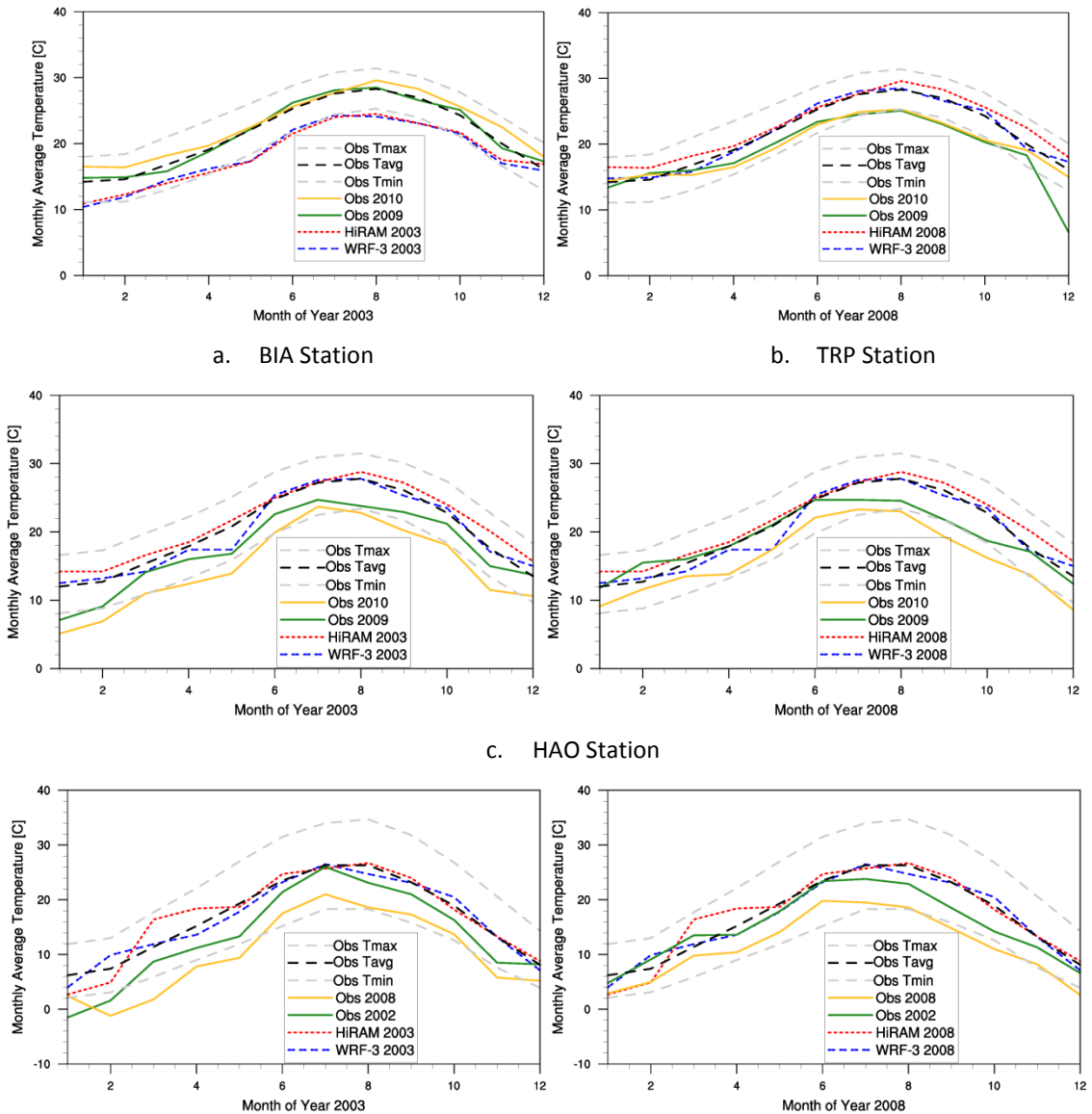
Fig. 4.6. Simulated (WRF-3 and HiRAM) monthly average 2m temperature (°C) for years 2003 and 2008 in comparison to observed decadal monthly average, maximum and minimum (2000-2010) and observed monthly average values for the extreme years 2009 and 2010 for BIA and TRP, and 2002 and 2008 for HAO.

Based on the evaluation for the three stations for the years 2003 and 2008 (Fig. 4.6), we found that the average temperate outputs of WRF 2003 and 2008 fall in the observed climatological ranges better than HiRAM's monthly simulated temperatures. Except for BIA, which is influenced by the proximity to the sea (recall the sea surface temperature is the same in WRF and HiRAM), WRF produces warmer

84

temperatures than HiRAM, and is closer to the observed averaged temperatures. The downscaling thus corrects some of the cold bias it inherits from HiRAM. However, some cold-bias persists; for example, both models indicate low average monthly temperatures for January at all three stations that are below the observed Tmin (which represents the coldest observed January for 2000-2010) by 1 to 3°C. These biases underline the difficulties for temperature simulations over complex topographical regions, even for the high-resolution WRF simulations. For other months, however, the WRF simulations are within the range of observations, indicating that the simulations are reasonable depictions of the climate. This might suggest that the bias in January in WRF is related to the 1-month warm-up, and potentially with a longer initialization from HiRAM, better results could be obtained. The variability at the sub-yearly time scale (differences between the hottest and coldest month) are captured well. The inter-annual variability, on the other hand, cannot be assessed since we would need to simulate all 11 years with WRF to attain the same level of variability. The selection of 2003 and 2008 based on our anomaly score, which is also influenced by precipitation, does not guarantee that they represent the hottest and coldest years to capture the inter-annual variability.

4.4.2   Precipitation

4.4.2.1 Recent Historic Extreme Years (2003 and 2008)

The wet season in the study area takes place primarily between the months of November and April with interspersed wet days through September-October and May, when precipitation is influenced by the influx of humid air from the Mediterranean sea. The orographic features control precipitation: when this moist air reaches the coast from

the west, it is uplifted by the mountains and then cools and condenses. Precipitation upsurges on the windward slopes and diminishes on the leeward inclines (since the air starts warming as it descends and the relative humidity decreases), creating a band of high annual precipitation parallel to the seaward slope of the west mountain range and along the coastal area. The average annual rainfall in the coastal zone ranges between 500 and 1100 mm, whereas the average annual precipitation over the mountainous region varies between 900 and 1850 mm (Atlas Climatique du Liban, 1977; Akadan, 2008).

The high spatial resolution of the RCM is central to simulating mesoscale phenomena and adding value to the GCM. For instance, Leung and Qian (2003) revealed considerable enhancement in the simulation of precipitation for the Pacific Northwest following the decrease in grid cell size of an RCM. As mentionaed above, the present model set-up is able to resolve the high resolution structure of storms and their impacts on precipitation in complex topographies, and this is illustrated for both wet (2003) and hot (2008) extreme years in Fig. 4.7. WRF reproduces the very high precipitation over the western mountains and the high precipitation over the coast while the GCM misses most of the fine-scale details due to its coarse resolution.

The monthly rainfall comparison for the three observational weather stations shows that WRF provides more realistic simulations of recent climatology than HiRAM (Fig. 4.8). For all stations considered, WRF shows a good representation of seasonal and geographic distribution of rainfall: the effect of the main geographical features (coastal and inland) is captured, along with the reproduction of the seasonal cycle. As expected, coarse resolution models miss some of the spatial patterns and can produce

significant discrepancies (for example HiRAM in 2008 at the inland HAO station), which WRF can correct.
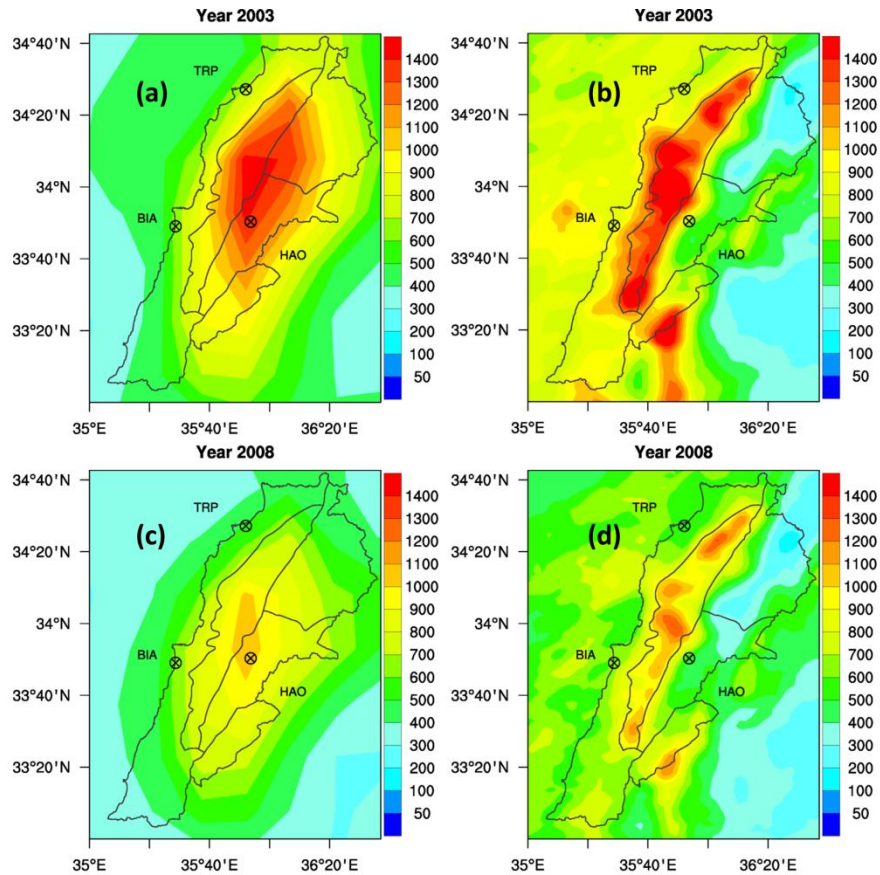
Fig. 4.7. Annual precipitation (mm) (a) 2003 HIRAM 25km resolution; (b) 2003 WRF3 km resolution; (c) 2008 HiRAM 25 km resolution; (d) 2008 WRF 3km resolution
The locations of the 3 observational stations used in the assessment are also shown.

The overall comparison between past regional model results and weather station data is quite reasonable. Recall that there is no reason to expect WRF to reproduce exactly the 2000-2010 observed average at any station, but it is anticipated to be withing the observational range. Moreover, the weather stations offer point records, whereas the model outputs are derived from a 3×3 km grid cell.
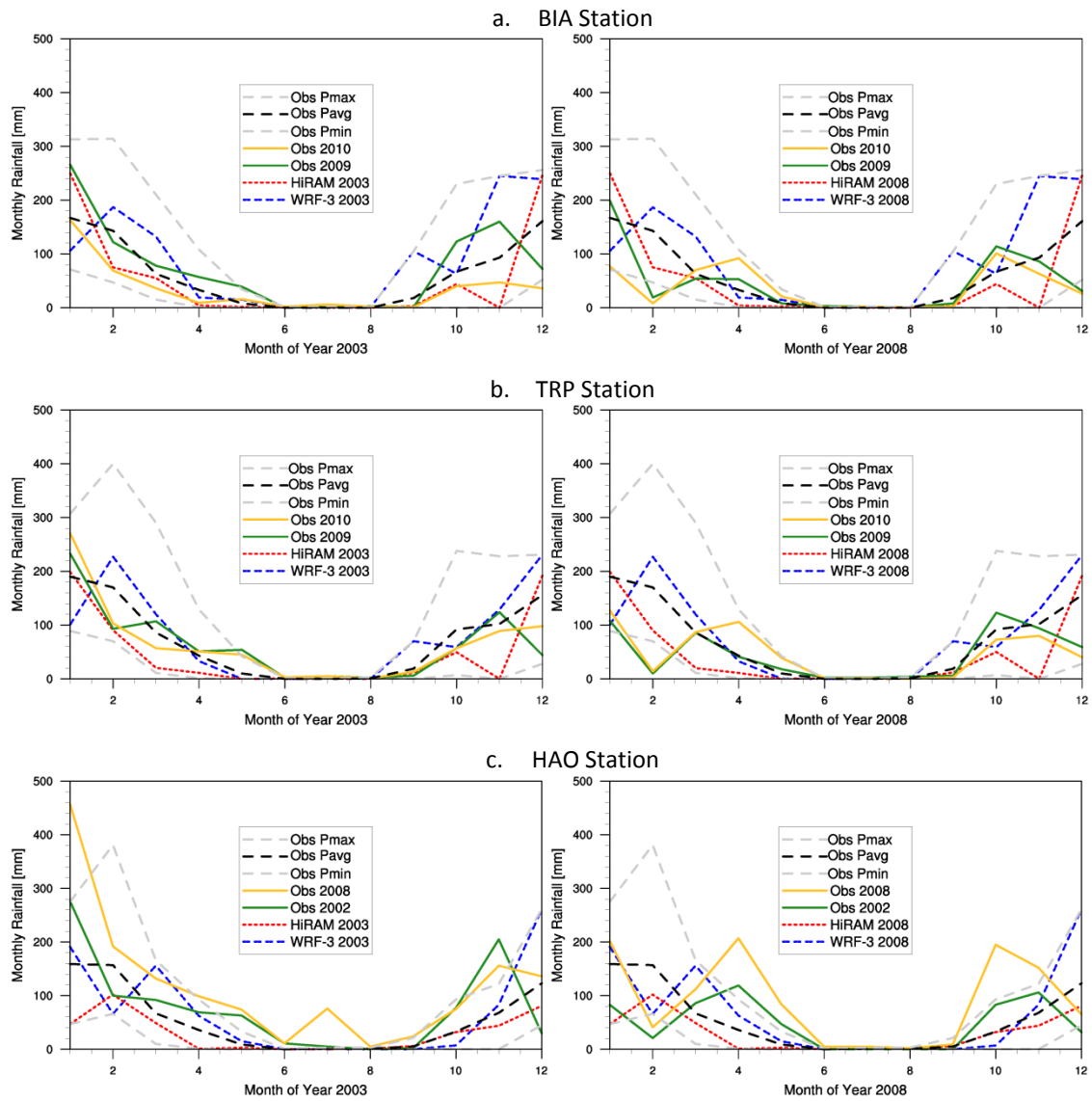
Fig. 4.8. Simulated (WRF-3 and HiRAM) monthly accumulated rainfall (mm) for years 2003 and 2008 in comparison to observed decadal monthly average, maximum and minimum (2000-2010) and observed monthly average values for the extreme years 2009 and 2010 for BIA and TRP, and 2002 and 2008 for HAO.

4.4.2.2 Future Years (2011-2050)

The projected variations in the total annual precipitation (rain and snow) by

HiRAM and WRF are presented in Table 4-2 and Fig. 4.9 to Fig. 4.12. All simulations

predict a considerable decrease in annual precipitation in the selected simulated extreme

years during the period 2011–2050, in comparison with present extreme hot and dry

conditions (2008). Each year has the highest anomaly score in its decade (except 2020

and 2017 which were selected from a 5-year span between 2016 and 2020 as explained

earlier); these reductions hence underline a worsening of the "worst-case" year in each

decade in the future and consequently increasingly adverse impacts on the water

resources of the region. Of particular concern is the potential for a 50% reduction in

snowfall (RCP 4.5 year 2050) since snowmelt is a critical source of water recharge in

the spring and early summer for the region.

Table 4-2 Annual precipitation (mm) for HiRAM and WRF over the study area

Model	Reference	RCP4.5				RCP8.5			
	2008	2020	2029	2040	2050	2017	2023	2035	2050
HiRAM	711	732	450	436	491	1072	526	445	468
WRF (total)	710	738	538	440	494	887	553	498	582
WRF (rain)	662	681	469	368	471	771	521	452	552
WRF(snow)	48	57	69	72	23	116	32	46	30
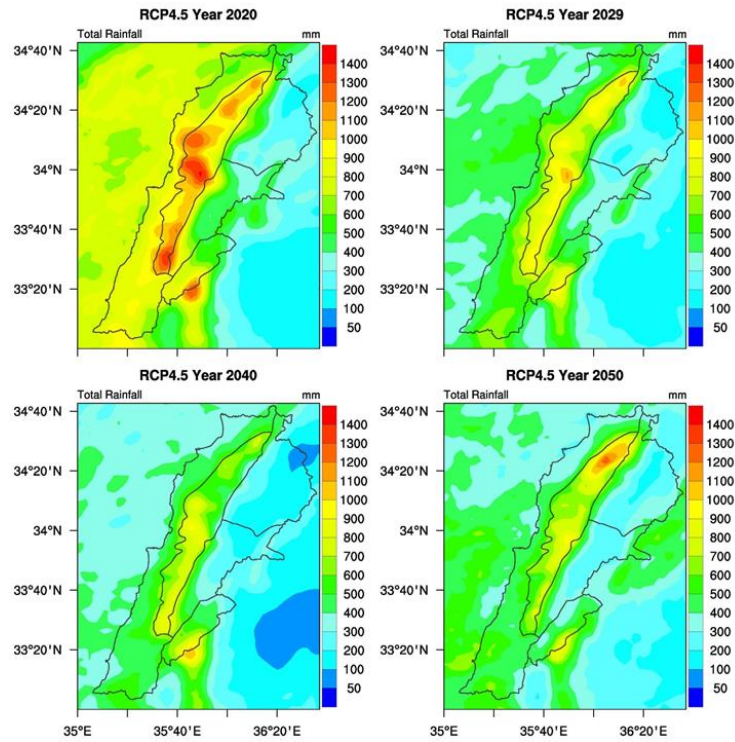
Fig. 4.9. RCP4.5 accumulated rainy-season rainfall (mm) for the extreme years (hottest and driest per decade) under consideration
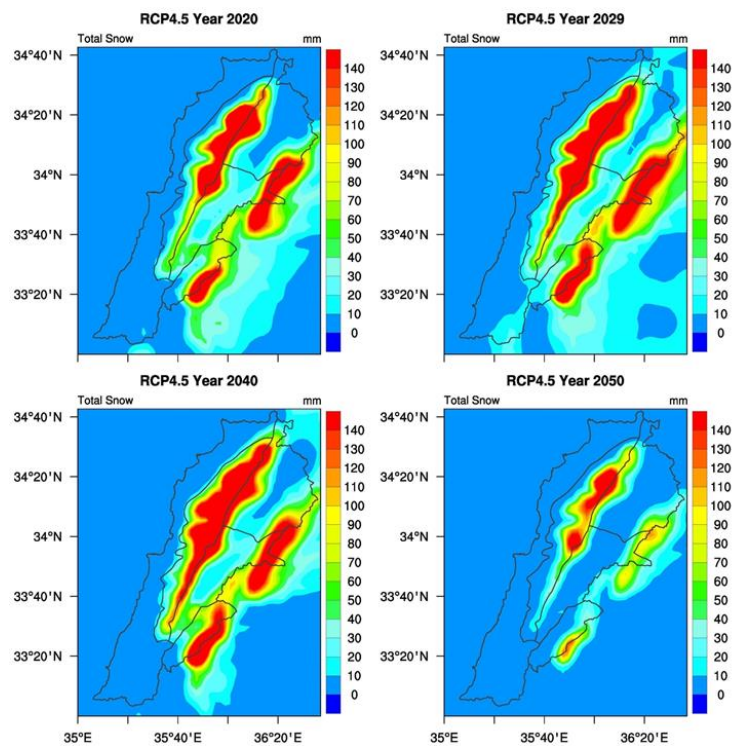
Fig. 4.10. RCP4.5 accumulated rainy-season snowfall (mm) for the extreme years (hottest and driest per decade) under consideration
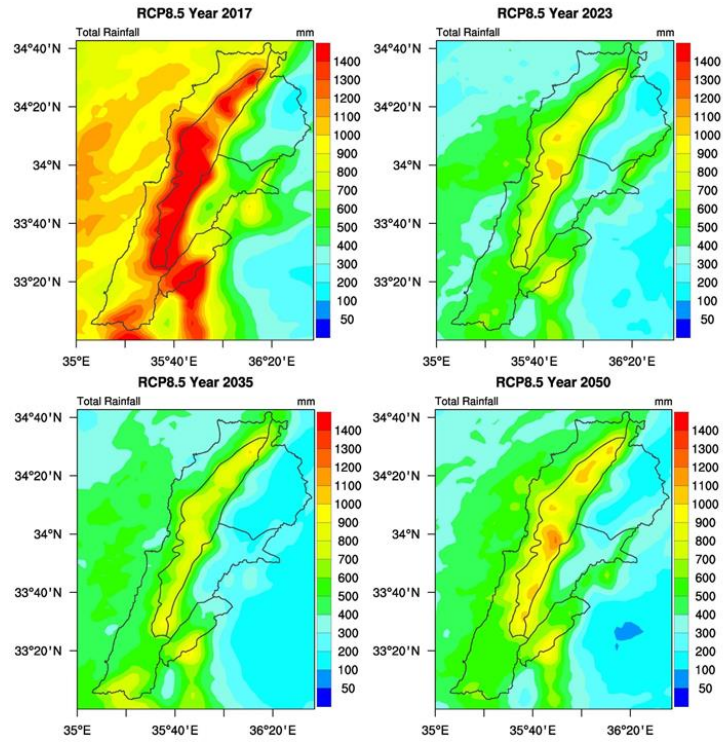
Fig. 4.11. RCP8.5 accumulated rainy-season rainfall (mm) for the extreme years (hottest and driest per decade) under consideration
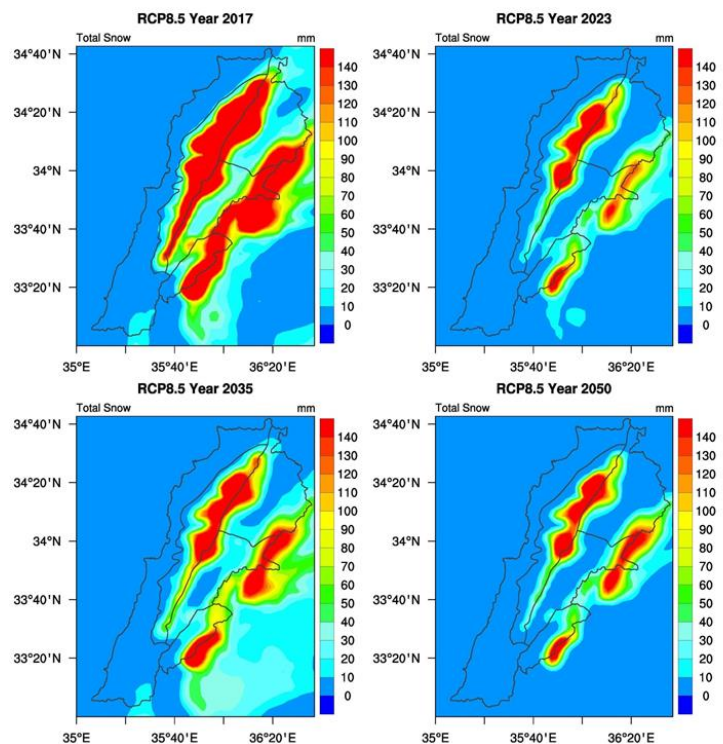
Fig. 4.12. RCP8.5 accumulated rainy-season snowfall (mm) for the extreme years (hottest and driest per decade) under consideration

91

The country averaged results alone are not sufficient to relay the whole scope of the impacts; Regional changes should equally be examined. Precipitation changes in the selected simulated extreme years during the period 2011–2050 include a variable decrease across the different climatic zones (Table 4.3), which is in accordance with the results of Lelieveld *et al.* (2014) and IPCC (2013) for the Mediterranean region. Apart from 2017 and 2020, which represent poorly the extreme conditions in their respective decades since there were selected from 5 years only (particularly 2017 which is very wet), both RCPs produce a noticeable decrease in extreme years' rainy-season (October to May) rainfall. The reduction is substantial over all climatic sub-regions, but regional differences clearly arise. This is one of the main benefits of downscaling with RCMs WRF: their high spatial resolution allows the identification of regions and watersheds inside a study area that might be particularly exposed to future changes. To be specific, the mountainous areas in this study are likely to be affected by severe changes, where rainfall is expected to decrease by approximately 16 to 33% in RCP4.5, and 14 to 24% in RCP8.5, in comparison to 2008. Precipitation in the mountainous regions nourishes the highly productive agricultural interior areas and coastal zones, and future changes will affect food production due to water shortage. Furthermore, snowfall and subsequent slow snowmelt in the mountains smooth the water recharge, and reduction in snow accumulation can further adversely influence the study area. All simulations consistently locate significant precipitation decreases along the coast (between 12 and 30%), but the most notable changes are projected for the inland regions, especially in the northern area (15 to 54% decrease) with respect to the baseline year 2008. The worst decrease over the four extreme years in rainy-season rainfall in RCP4.5 (–35%) is more pronounced than in RCP8.5 (–29%) with respect to the extreme past dry year 2008. As

for snowfall, it is likely to be impacted by climate warming with increases in saturation

vapor pressures and fluctuations in the frequency of occurrence of temperatures below

the rain-snow shift temperature (O'Gorman, 2015). Both RCPs predict an increase

during the simulated extreme years from 2020 till 2040, but this is dissipated by the

middle of the century and gives way to a decrease of about 36% over the mountains and

exceeding 50% in the inland regions (the largest reduction in snowfall).

Table 4.3. Regional rainy-season rainfall (mm) and snowfall (mm) for RCP4.5 and 8.5

	Reference	RCP4.5				RCP8.5			
Region	**2008**	**2020**	**2029**	**2040**	**2050**	**2017**	**2023**	**2035**	**2050**
Rainfall									
Coast	683	829	558	484	478	1098	519	537	601
Mountains	952	1032	803	636	735	1433	820	721	867
Inland_n	389	341	260	178	315	413	333	223	265
Inland_c	545	538	443	323	346	824	455	354	465
Inland_s	738	677	590	530	474	1155	584	520	618
Study area	**662**	**684**	**531**	**430**	**470**	**985**	**542**	**471**	**563**
Snowfall									
Coast	3	1	5	5	0	4	0	2	0
Mountains	95	121	135	156	61	249	73	91	66
Inland_n	34	38	53	45	16	88	23	36	25
Inland_c	57	58	64	63	16	110	26	44	28
Inland_s	54	67	88	91	21	131	37	59	33
Study area	**48**	**57**	**69**	**72**	**23**	**116**	**32**	**46**	**30**

The probability density function (PDF) of daily rainfall allows the

determination of the nature of potential changes, distinguishing the sort of events that

might substantially vary, and outlining the precipitation patterns in the future. Fig. 4.13

and Fig. 4.14 present the variations in the intensity and frequency of daily events in the

5 geo-climatic regions in RCP4.5 and 8.5 respectively, where only wet days ($P \geq 0.1$

mm/day) in the rainy-season are considered. The bins of PDF show the days of light

rainfall (P <1 mm/day), days of moderate rainfall (1 mm/day $\leq P \leq$ 10 mm/day), days of

heavy rainfall (10 mm/day $\leq P \leq$ 20 mm/day) and very heavy rainfall ($P\geq$ 20 mm/day).

The PDFs show that there is generally a shift towards lower intensity events in all

regions in both RCPs. The number of moderate rainfall events is projected to increase

along the coast and in the mountainous region under both RCPs. As for the frequency of

heavy precipitation, the simulated extreme years in RCP8.5 show a higher frequency of

these rainfall events than those in RCP4.5 along the coast, as well as in the central and

southern inland area.
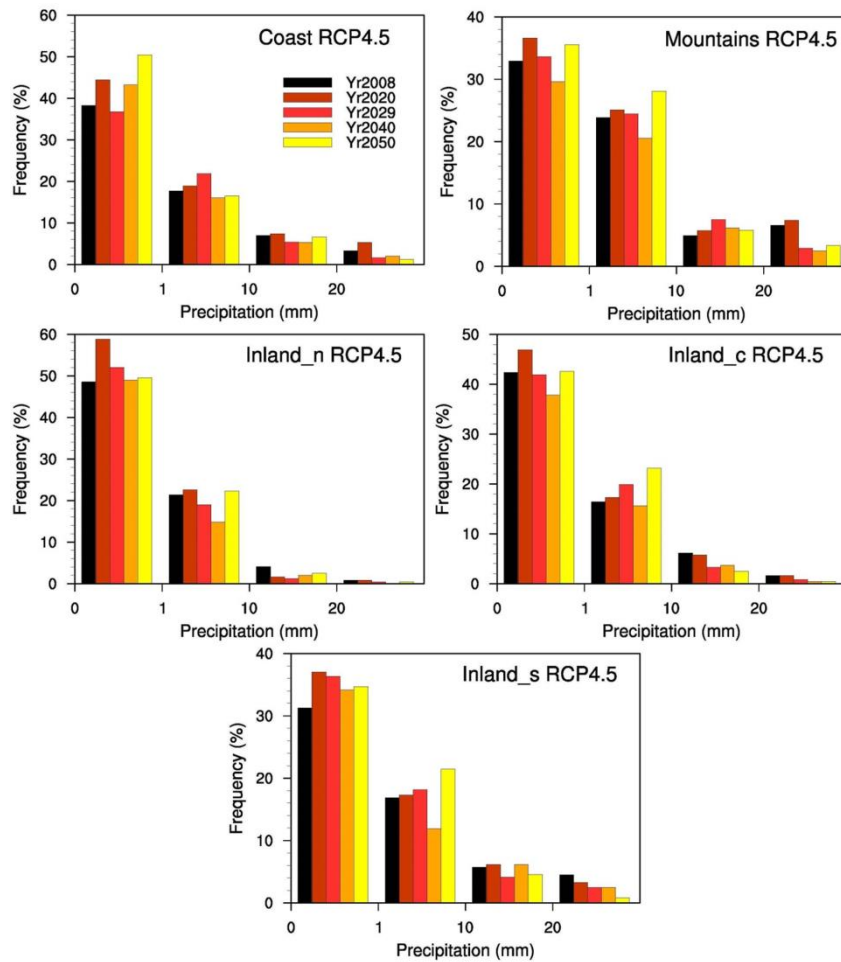
Fig. 4.13. Precipitation probability density plots per region in RCP4.5
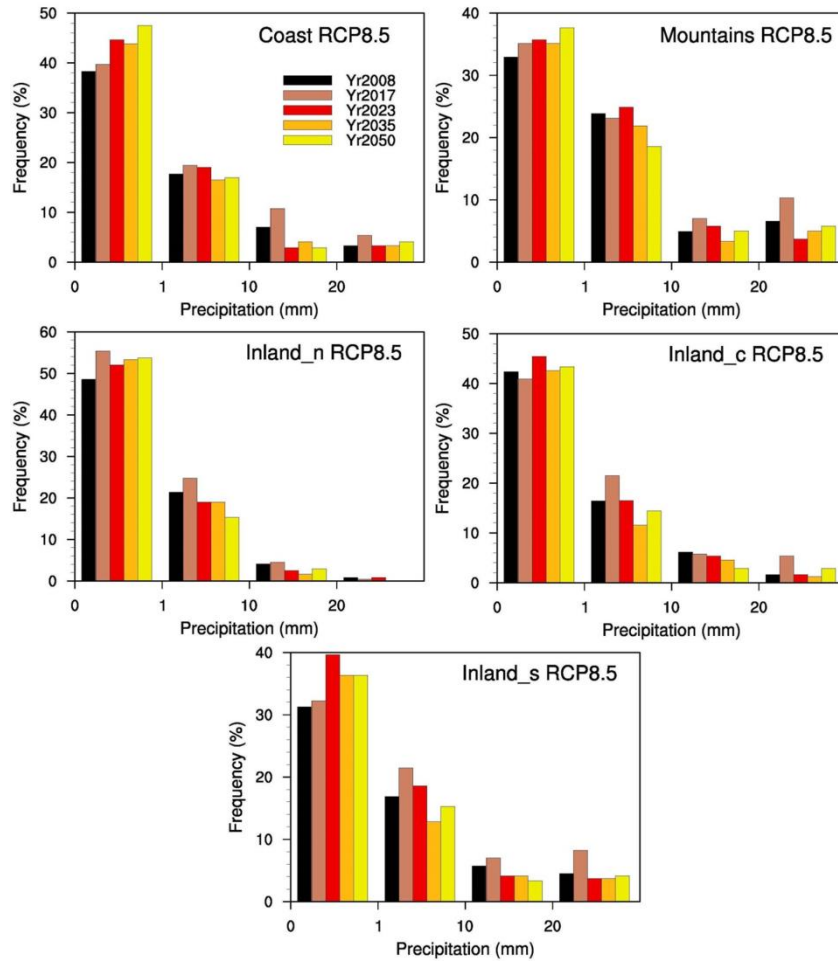
Fig. 4.14. Precipitation probability density plots per region in RCP8.5

The risk of extreme rainfall events and droughts, was further examined using five indices from the Expert Team on Climate Change Detection and Indices (ETCCDI) to portray changes in extreme precipitation: the number of consecutive dry days (CDD), consecutive wet days (CWD), days of heavy rainfall (R10MM), days of very heavy rainfall (R20MM) and maximum one day precipitation (RX1DAY) on a yearly basis (Persson *et al*., 2007) (Table 4.4). According to ETCCDI, CDD is the count, using the time series of daily precipitation amounts, of the largest number of consecutive days where rainfall rate is less than 1 mm/day. On the other hand, CWD is the count, using

the time series of daily precipitation amounts, of the largest number of consecutive days where rainfall rate is at least 1 mm/day. Days of heavy rainfall is the count of days where the rainfall rate is greater than 10mm, while days of very heavy rainfall is the number of days exceeding the rainfall rate of 20mm. The maximum one day precipitation reports the highest rainfall rate attained during a day over the year. During the future simulated extreme years, the wet episodes are anticipated to be smaller, while the dry episodes are expected to be longer. The changes in CDD are more prominent in RCP4.5 than RCP8.5 in the simulated extreme years during the period 2011-2050. The worst year in RCP4.5 (2040) indicates that the length of the dry spells is likely to increase over the region, especially in the coast (58%), mountains (75%) and northern inland region (37%). The modifications in CWD suggest that the span of continuous wet periods during the future simulated extreme years is expected to decrease over practically the entire study area. The most substantial change is expected in the northern inland region under both RCPs where the CWD drops to 50% in the 2050 simulations. This is consistent with the findings of Barrera-Escoda *et al*. (2014) for the Iberian Peninsula who projected a decrease of 10 days in CDD and a reduction of 3-4 days in CWD in similar topographies in the Mediterranean region by year 2050. Hadjinicolaou *et al*. (2011) reported similar results for Cyprus by midcentury. Similarly, the number of days of heavy and very heavy rainfall (RR0MM and RR20MM) will decrease in the simulated future extreme years in most regions, reaching the level of 50% reduction in the northern inland zone already known for its dry climate, which is the same conclusion observed in that region's PDF (Fig. 4.13 and Fig. 4.14). Finally, the maximum one-day precipitation is expected to decrease in all regions under both scenarios during the extreme years except on the mountains, where WRF projected a

slight increase. This result confirms the projections made for nearby Cyprus by 2050

(Hadjinicolaou *et al.*, 2011), which is included in our outer domain of 9km.

Table 4.4. Past and Future CDD (days), CWD (days),
R10MM (days), R20MM (days) and RX1DAY (mm) per region per RCP

	Reference	RCP4.5				RCP8.5			
Region	2008	2020	2029	2040	2050	2017	2023	2035	2050
CDD									
Coast	66	80	103	104	69	64	90	84	92
Mountains	65	85	98	114	67	73	82	80	69
Inland_n	100	109	120	137	71	114	124	125	110
Inland_c	121	114	126	135	83	117	122	102	122
Inland_s	111	110	130	119	79	109	120	100	111
Study	**92**	**100**	**115**	**122**	**74**	**96**	**108**	**98**	**101**
CWD									
Coast	7	8	6	6	5	8	4	5	4
Mountains	8	8	6	6	6	8	6	6	5
Inland_n	6	6	4	4	4	6	5	4	3
Inland_c	6	7	5	5	5	7	5	5	5
Inland_s	7	8	5	5	6	8	5	6	5
Study	**6**	**8**	**5**	**5**	**5**	**7**	**5**	**5**	**4**
RR10MM									
Coast	22	28	18	17	17	36	16	17	17
Mountains	28	33	25	20	24	41	25	21	24
Inland_n	12	9	7	5	9	36	16	17	17
Inland_c	18	18	13	10	10	41	25	21	24
Inland_s	23	23	18	17	16	12	10	6	8
Study	**21**	**22**	**16**	**14**	**15**	**27**	**15**	**12**	**15**
RR20MM									
Coast	10	14	6	6	6	18	8	8	9
Mountains	15	18	12	9	10	24	11	12	13
Inland_n	4	3	2	1	3	4	3	2	2
Inland_c	7	7	5	3	3	12	6	5	7
Inland_s	10	10	7	8	9	12	9	8	10
Study	**9**	**10**	**6**	**5**	**6**	**14**	**8**	**7**	**8**
RX1day									
Coast	62	57	74	46	42	74	51	54	64
Mountains	73	68	92	65	77	87	100	67	82
Inland_n	39	35	33	24	33	37	40	27	34
Inland_c	59	39	71	41	33	52	51	37	45
Inland_s	74	44	73	61	36	71	52	48	55
Study	62	**49**	**69**	**47**	**44**	**64**	**59**	**47**	**56**

4.5   Summary and Conclusion

In this chapter, the regional climate model WRF was used to downscale future climate simulated by the HiRAM GCM over a complex topographical area under the RCP4.5 and RCP8.5 scenarios. We simulated recent past extreme wet and dry years (2003 and 2008) and one future (2011–2050) extreme year per decade for each scenario: 2020, 2029, 2040 and 2050 from RCP4.5 and 2017, 2023, 2035 and 2050 from RCP8.5. Since the goal of this chapter is to compare the future driest year with the present driest year in order to determine how the extreme climate will shift, the baseline for comparison between the past and the future was the hottest/driest year 2008. Our focus being on water resources impacts, the selection of simulation years was performed using an anomaly score based on median annual temperature and accumulated precipitation from HiRAM daily time series. The higher inter-annual variability of precipitation resulted in it dominating this anomaly score. Model performance for average temperature and precipitation were evaluated by comparing the historic results for 2003 and 2008 results with decadal observations (2000-2010) for three weather stations located along the coast and in the central inland region. The historic results demonstrate that, compared with results from the coarse resolution of HiRAM, dynamical downscaling improves the simulated mean temperature and precipitation and is highly beneficial. The downscaled results were predominantly within the range of observed climatic ranges, correcting the cold bias inherited from HiRAM.

The improvement in temperature and precipitation obtained through downscaling are largely attributed to improvements in topography and coastline representation. WRF captured the severe distinction between the exceptionally wet climate on the seaward slopes of west mountain range, which is governed by orographic

precipitation, and the dry climate inland. For such complex topographies, therefore, climate change impact assessment requires downscaling that can capture the strong spatial variability.

In the context of implications of the two scenarios RCP 4.5 and RCP8.5 on precipitation, the high-resolution downscaling simulations provided evidence of a significant drier climate over the whole study area during the simulated future extreme years from 2016 till the mid of this century, with reduction in annual precipitation of about 30%. The projections show that this significant decrease in precipitation spans all geo-climatic regions for both RCPs. However, nontrivial inter-regional differences, which can only be captured by high resolution RCMs, emerged. The mountainous areas as well as the inland regions will be particularly affected by these precipitation decreases (particularly in terms of snowfall), while the impacts in the coastal regions are slightly lower.

CHAPTER 5

SEASONAL AND REGIONAL PATTERNS OF INTENSIFICATION OF FUTURE TEMPERATURE EXTREMES FROM HIGH-RESOLUTION DYNAMIC DOWNSCALING OVER COMPLEX TERRAIN

5.1   Introduction

Since the last century, the concentration of the main greenhouse gas (GHG), carbon dioxide (CO_2), has increased from its pre-industrial concentration of ~278 parts per million (ppm) to over 378 ppm in 2005, with a rate of rising now at 1.9 ppm per year (IPCC, 2013). As a result, the global mean surface air temperature has increased by 0.85°C and the rate of warming has reached the level of 0.01°C annually since 1950 (IPCC, 2013). The increased temperatures have caused changes in the weather and climate worldwide, and accordingly have influenced society, ecology and various economic sectors. As such, the last decade has witnessed an exceptional number of extreme heat waves around the world with considerable adverse impacts (Christidis *et al*., 2011; Rahmstorf and Coumou, 2011). For instance, between 25,000 and 70,000 deaths were attributed to the 2003 heat wave in Europe (D'Ippoliti *et al*., 2010) in addition to effects on glaciers and ecosystems leading to the destruction of large areas of forests by fire (Alexander and Tebaldi, 2012). Another example of a recent extreme heat wave is the Russian heat wave of 2010, which had substantial adverse consequences including ~55,000 deaths, 25% decrease in annual crop yields, more than 1 million hectares burned areas, and ~US$15 billion in economic losses (The World Bank, 2012).

In the absence of climate change, such extreme events would be expected to occur infrequently, but with the projections of an increase in global temperatures (IPCC, 2013), these occurrences will happen at a more accelerated pace. Indeed, "confidence has grown that some extremes will become more frequent, more widespread and/or more intense during the 21st century" (IPCC, 2013). As a result, the demand for information services on weather and climate extremes is increasing. Relying on observations alone can simply detect the historical trends. Hence, numerical modeling became the only approach for examining the projection of future extreme events. One limitation of this approach is the coarse resolution of the General Circulation Models (GCM) that at present, have spatial resolutions of about 1 degree and are not suitable for fully capturing the mesoscale systems and topographic effects needed to assess the evolution of extreme events in a future climate (Rummukainen, 2010). Dynamical downscaling techniques can refine GCM projections (Giorgi and Mearns, 1991) using high resolution Regional Climate Models (RCM) driven by GCM results or reanalysis data that can better resolve mesoscale effects including those associated with topography (e.g. coastlines, mountains, water bodies, vegetation), the local climate, and the concomitant influence on the temperature and precipitation systems (Heikkilä *et al*., 2011).

The objective of this chapter is to downscale regional future simulated temperature extremes over a challenging complex terrain, with a particular focus on the influence of topography and seasonality on future changes in the frequency, amplitude and persistence of temperature extremes. The country of Lebanon in the eastern Mediterranean basin is used as a case study. Temperature increases and future drier conditions are projected for the Mediterranean (Beniston *et al*., 2007; Giorgi and

Lionello, 2008), which could lead to an increase in extreme events according to global and regional models (Barrera-Escoda *et al*., 2014). The local population is particularly vulnerable to changes in the frequency and intensity of extreme events, such as heat waves and droughts, and indicators of the degree of future susceptibility to climatic extremes in this region are of paramount importance to guide adaptation and mitigation measures. The high-resolution Weather Research and Forecast (WRF) (Skamarock *et al*., 2008) Model is selected for downscaling, driven by the High Resolution Atmospheric Model (HiRAM) (Zhao *et al*., 2009; Jiang *et al*., 2012) to provide an understanding of the dynamics of climate change on a highly resolved regional basis, not possible using GCM output, under two different Representative Concentration Pathways, RCP4.5 and 8.5, from those defined by the IPCC (2013).

The study focuses on selected future extreme dry years from both scenarios in comparison with a past extreme dry and hot year. WRF evaluation for temperature and precipitation using observational data and HiRAM boundary conditions for historic dry years was conducted as a reference in Chapter 4, and downscaling results for precipitation were used for studying future extreme dry years in the same chapter. Chapter 4 showed good agreement between the simulations of the historic and present climate and the observational data, indicating that the model is applicable for studies of climate change over this topographically complex region. The evaluation results showed the benefit of resolving the details in the spatial and temporal patterns, for both temperature (average, maximum and minimum) and precipitation, but did not assess how temperature extremes will evolve in the future. The present chapter fills this gap, and assesses eleven indicators of climatic temperature extremes, in addition to averages. We compare how the probability distributions of these extremes change in various

regions with contrasting topographies. This focus is motivated by current literature that has shown an amplification of extremes in recent decades (Alexander *et al*., 2006) and the realization that changes in extremes have a greater impact on society and ecosystems in general than the increase in average values (IPCC, 2013; Easterling *et al*., 2000; Meehl *et al*., 2000).

5.2   Methods and Data

5.2.1   Models Description

5.2.1.1 <u>Global Model</u>

The High-resolution Atmospheric General Circulation (HiRAM) developed by the Geophysical Fluid Dynamics Laboratory (GFDL) at Princeton University is adopted to simulate climate projections. HiRAM has been developed based on the Atmospheric Model (AM2) (Zhao *et al*., 2009). It allows the use of fine horizontal grid spacing up to few kilometers and has 32 vertical levels resolution (Bangalath and Stenchikov, 2015). It employs a cubed-sphere finite-volume dynamical core (Lin, 2004) and is used here at C360 (about 25 km) resolution, coupled with the new GFDL land model, LM3, as the land component (Bangalath and Stenchikov, 2015). The HiRAM simulations follow the CORDEX protocol (Giorgi *et al*., 2009) and were conducted for historic (1975-2004) and future (2007-2050) periods using both Representative Concentration Pathways (RCP) 4.5 and 8.5 scenarios. RCP 4.5 is a scenario of long-term, global emissions of GHGs, short-lived species, and land-use-land-cover which stabilizes CO_2 equivalent at approximately 650ppm (a radiative forcing level of 4.5 W/m^2) in the year 2100 without ever exceeding that value (Clarke *et al*., 2007). As for RCP 8.5, it corresponds to a high GHG emissions pathway compared to the scenario literature (IPCC, 2013), and hence

also to the upper bound of the RCPs. RCP8.5 is a so-called 'baseline' scenario that does

not include any specific climate mitigation target. The GHG emissions and

concentrations in this scenario increase considerably over time, leading to a radiative

forcing of 8.5 W/m^2 at the end of the century (IPCC, 2013). The Sea Surface

Temperatures from the GFDL Earth System Model runs, completed for the IPCC

Assessment Report AR5, were adopted as the bottom boundary conditions over the sea.

The recommended time-varying GHG and stratospheric/tropospheric aerosol

distribution datasets were used to reproduce the observed radiative forcing in the model

(Bangalath and Stenchikov, 2015).

5.2.1.2 Regional Model

       The Weather Research and Forecasting (WRF) Model Preprocessing System

WPS was used to dynamically downscale HiRAM outputs to finer resolution in the

study area region for initial and boundary conditions. The advanced research WRF

(ARW) model version 3.4.1 (Skamarock *et al*., 2008) was adopted for all simulations. It

is a compressible, nonhydrostatic model that uses terrain-following coordinates and

solves the governing equations written in flux-form to conserve mass and dry entropy.

The Runge–Kutta third-order time scheme was used and the fifth and third-order

advection schemes were chosen for the horizontal and vertical directions, respectively.

       The simulation domains are shown in Fig. 5.1a. The WRF model is built over a

parent domain (d01) (1350 km × 1700 km) with 9 km of spatial resolution, covering the

eastern part of the Mediterranean Sea. The inner nested domain (d02) (462 km×579

km), with a spatial resolution of 3 km, is focused on the study area, the country of

Lebanon (Fig. 5.1b), and comprises parts of the surrounding countries. The highest

resolution of 3km proved to be sufficient in previous tests comparing historic WRF

simulations over the same domain to a broad range of ground observations; no

significant improvement was noted when the resolution was further increased to 1 km

(Chapter 2). Hence, this 3 km WRF resolution was adopted in the remaining of this

chapter and all results shown are from this resolution. MODIS (for the year 2001) land

use data was used with 21 land categories and Lambert Conformal projection (most

convenient for mid-latitude regions since it yields uniform grid spacing). The time step

used was 30 seconds for the largest domain, and all domains had 28 vertical levels (with

a vertically-stretched grid) arranged according to terrain-following hydrostatic pressure

coordinates. The number of vertical levels is also based on the tests for historic periods

(Chapter 2).
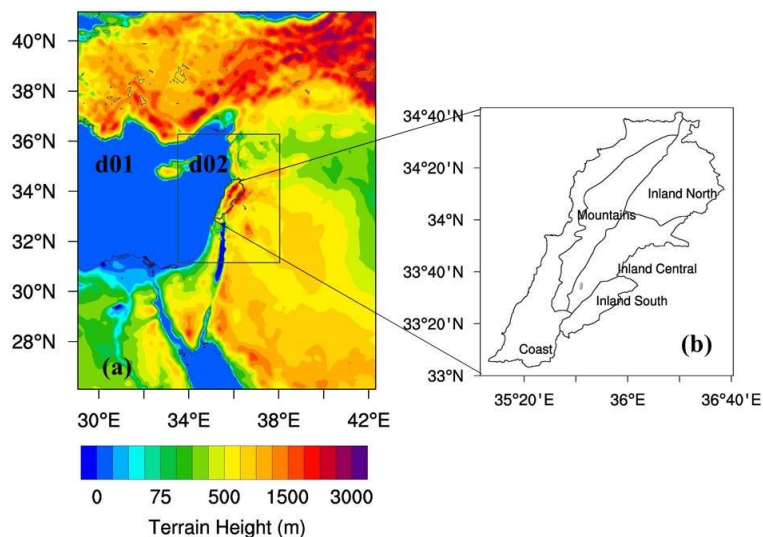
Fig. 5.1. (a) WRF's two domains (9:3km) configuration with a pseudocolor map of
terrain height ASL (m), (b) the focus area divided into its five geo-climatic regions

105

The time interval of the boundary data is 6 hours, and the sea surface temperature (SST) is also updated every 6 hours. One past dry and hot year (2008) forced by HiRAM was simulated and used as a baseline scenario to allow for comparison and quantification of changes. Then eight future yearlong simulations were performed to generate extreme climate projections over the project area, four from RCP 4.5 (2020, 2029, 2040 and 2050) and four from RCP 8.5 (2017, 2023, 2035 and 2050). The selection of these extreme years, detailed in Chapter 4, consists of identifying the "worst" year in a given decade using an anomaly score that assesses the negative precipitation and positive temperature deviations during that year from decadal means. It should be emphasized that these years will therefore not necessarily be the hottest of the decade. Each simulation covered a 13-months physical period, initialized on the first of December of the year preceding the year of interest to allow a one month spin-up period (which was discarded) before the analysed modelling periods (January to December of the year of interest), as recommended in other studies (Zhang *et al.*, 2009; Gao *et al.*, 2012; Soares *et al.*, 2012).

The parameterizations schemes adopted in this study are: WRF Single-Moment 6-Class Microphysics Scheme (WSM6) (Hong and Lim, 2006), Monin Obukhov and Mellor Yamada Janjic (Eta) for surface layer and PBL physics (Mellor and Yamada, 1974, Janjic, 2001), Rapid Radiative Transfer Model (RRTM) (Mlawer *et al.*, 1997) and Dudhia Long Wave and Short Wave (LW/SW) for radiative processes (Dudhia, 1989), and Noah Land Surface Model (LSM) (Chen and Dudhia, 2001) for surface processes. The selection is based on our previous WRF tests as detailed in Talbot *et al.* (2012) and Li *et al.* (2013). The same WRF configuration used here also performed well in historic simulations over the study area forced by reanalyses data from GFS (Chapter 2). For

past climate conditions (2008) the CO_2 concentration was considered to be 330 ppm, and for the future (2011-2050) climate, we changed the atmospheric equivalent CO_2 concentration in each simulated year of WRF to match the respective scenarios RCP4.5 and RCP8.5 and to be consistent with HIRAM. This alters the radiative balance of the simulations slightly but has a minor impact on the relatively short-term regional simulations we conduct with WRF (this was verified by comparing to simulations with current CO_2 concentration).

5.2.2 *Analysis and Data Handling*

Different climate indicators are calculated from the 2-hour interval WRF model outputs to capture extreme events,. The study area can be divided into three broad climatic trends: the coastal, the mountainous and the inland, each of which can be further subdivided into sub-regions based on a long-term trend of weather parameters including temperature, relative humidity, rainfall and wind (Atlas Climatique du Liban 1977). However, given the difference in annual precipitation (Fig. 5.1b), we only found it significant to consider these further subdivisions in the inland zone that we further partitioned into the north, central and south sub-regions. The subdivisions in the other regions are not critical for the present analysis. The adopted core indices are developed by the World Meteorological Organization working group, the Expert Team on Climate Change Detection and Indices (Persson *et al*., 2007). Theses indices were mainly selected for assessment of aspects related to a changing regional climate, which include changes in intensity, frequency and duration of extreme temperature events. The indices can be divided into 4 different categories:

- Absolute indices representing maximum or minimum values statistics

over a season or year. They include maximum daily temperature (Tmax), and minimum daily temperature (Tmin);

- Percentile-based indices including occurrence of warm nights (TN90p), occurrence of warm days (TX90p); heat wave duration index (HWDI), and heat wave frequency index (HWFI);

- Threshold indices such as annual occurrence of summer days (SU);

- Duration indices including the number of consecutive summer days (CSU), consecutive frost days (CFD), and heating degrees days (HD).

In addition to the above indices, the analysis covered the change in average temperature (Tavg) throughout the year for both RCPs in comparison to the reference year 2008. Finally, in the case of presence of biases in temperatures from WRF runs, which can be due to both HiRAM and WRF simulation errors, one can expect the biases to have a relatively minor influence on the difference fields since they would be the same for the past reference and future HIRAM/WRF runs. Table 5.1 defines each index which was calculated using the Climate Data Operators (CDO) software package (Schulzweida *et al*., 2009). The results of the indices calculations are presented in the relevant sections, i.e. if the index is based on maximum temperatures, it will be addressed in the maximum temperature section.

Table 5.1. Climate indicators calculated from daily downscaled future projections.
2008 is used as reference period for all indicators

Variable	Description
Average Temperature (Tavg)	Yearly average value of average daily temperature
Maximum Temperature (Tmax)	Yearly maximum value of maximum daily temperature
Minimum Temperature (Tmin)	Yearly minimum value of minimum daily temperature
Percent occurrence of warm nights (TN90P)	Using a time series of daily minimum temperatures Tmin, and the 90th percentile of the daily minimum temperature series during the year used as a reference TNn90, TN90P is calculated as the percentage of time where Tmin > TNn90
Percent occurrence of warm days (TX90P)	Using the time series of daily maximum temperatures Tmax, and the 90th percentile of the daily maximum temperature series during the year used as a reference TXn90, TX90P is calculated as the percentage of time where Tmax > TXn90
Heat Wave Duration Index (HWDI)	Using the time series of daily maximum temperatures Tmax, and the mean TXnorm of the daily maximum temperature series of a 5-day window centered on each calendar day during the year used as a reference, HWDI is the number of days where, in intervals of at least 6 consecutive days, Tmax > TXnorm + 5^0C. A further output is the number of heat waves periods longer than or equal to 6 days
Heat Wave Frequency Index (HWFI)	Using the time series of mean daily temperatures Tavg, and the 90th percentile TGn90 of the mean daily temperature of a 5-day window centered on each calendar day during the year used as a reference, HWFI is the number of days where, in intervals of at least 6 consecutive days, Tavg > TGn90. A further output is the number of warm-spell periods longer than or equal to 6 days.
Summer days (SU)	Using the time series of daily maximum temperatures Tmax, SU is the number of days where Tmax > 25^0C
Consecutive Summer days (CSU)	Using the time series of daily maximum temperatures (Tmax), CSU is the largest number of consecutive days where Tmax > 25^0C
Consecutive Frost days (CFD)	Using the time series of daily minimum temperatures (Tmin), CFD is the largest number of consecutive days where Tmin < 0^0C
Heating Degree days (HD)	Using the time series of daily mean temperatures Tavg, then the heating degree days are defined as the sum of $(17 - Tavg)^0$C, where only values Tavg > 17^0C are considered.

5.3   Results and Analysis

5.3.1   Average Temperatures (Tavg)

The mean seasonal and annual temperatures over the various regions of the study area inside the fine nest for RCP4.5 and RCP8.5 are shown in Table 5.2. For RCP 4.5, there are no major regional differences in the annual mean warming, except for the

tendency of the coast to warm less than the mountain and interior regions, but strong

seasonal differences are observed in all regions. The unexpected decreases in the winter

(December-January-February, DJF) and spring (March-April-May, MAM) temperatures

almost offsets the increases in summer (June-July-August, JJA) and autumn

(September-October-November, SON) temperatures, yielding annual mean

temperatures that increase by about 0.3^{o}C. For RCP8.5, the picture is somewhat

different with cooling in the winter and spring early on, but that seems to reverse after

2040. The coastal warming is also weaker than other regions in RCP 8.5 possibly due to

sea breeze effects. This implies that the inter-seasonal temperature swings will be more

intense in all regions for both scenarios. The temperature decrease during winter months

could be linked to a reduction in cloud cover and rainfall (Chapter 4), which increases

radiative surface cooling and reduces the release of latent heat during precipitation. This

would then result in a more rapid depletion of soil moisture in the summer that

exacerbates the temperature rise during the hot season by limiting evaporative cooling.

The regions that are most affected by the decrease in winter precipitation are the

mountains and northern and southern inland regions (Chapter 4), which are the same

areas where the decrease in the average winter temperature can exceed 2°C in the year

2040 from RCP4.5. This decrease is also taking place in the spring season of the year

2029 for RCP4.5, where it affects the central inland region as well. The strong warming

will affect the mountains and inland regions during the summer and fall seasons in both

scenarios, with the strongest signal occurring during the fall where the increase in the

average temperature can reach nearly 4°C in the central inland region (2029 and 2040

compared to 2008). The same pattern of decrease (increase) in winter and spring

(summer and fall) average temperature is present in RCP8.5, where the rise in summer

and fall temperature will remain on the order of +2.5°C. However RCP8.5 results, as

expected, in warmer yearly-averaged temperatures over all regions.

Table 5.2. Regional, seasonal and annual average 2m temperature (°C)

Season/ Region	Ref. 2008	RCP4.5				RCP8.5			
	2008	2020	2029	2040	2050	2017	2023	2035	2050
DJF									
Coast	11.3	11.3	9.9	9.6	10.0	9.7	10.7	10.7	11.7
Mountains	4.4	4.4	2.5	2.2	3.3	2.4	3.6	3.7	5.1
Inland_north	4.7	4.4	2.6	2.6	3.3	2.9	3.6	3.9	5.4
Inland_central	5.0	5.1	3.1	3.1	4.1	3.4	4.1	4.4	6.0
Inland_south	5.6	5.6	3.7	3.6	4.6	3.9	4.7	4.9	6.5
Study area	**6.2**	**6.1**	**4.4**	**4.2**	**5.1**	**4.5**	**5.3**	**5.5**	**6.9**
MAM									
Coast	17.8	16.4	16.5	17.1	17.0	16.8	18.4	17.2	17.2
Mountains	11.6	10.2	9.2	10.0	10.2	9.3	11.9	10.2	10.5
Inland_north	12.9	11.8	11.0	11.8	12.1	11.0	13.2	11.8	12.1
Inland_central	13.3	12.1	11.1	11.8	12.2	11.1	13.5	12.0	12.2
Inland_south	13.7	12.4	11.4	12.1	12.5	11.5	13.9	12.3	12.2
Study area	**13.9**	**12.6**	**11.8**	**12.6**	**12.8**	**11.9**	**14.2**	**12.7**	**12.8**
JJA									
Coast	24.0	24.2	25.4	24.3	24.6	23.2	24.4	24.7	26.2
Mountains	19.3	20.1	22.2	21.5	20.1	19.0	20.4	21.3	21.4
Inland_north	21.7	22.4	24.4	23.8	22.7	21.5	23.0	23.7	23.9
Inland_central	21.8	22.7	24.8	24.1	22.8	21.8	23.1	24.1	24.0
Inland_south	21.4	22.3	24.3	23.4	22.3	21.2	22.4	23.3	23.6
Study Area	**21.6**	**22.3**	**24.2**	**23.4**	**22.5**	**21.3**	**22.7**	**23.4**	**23.8**
SON									
Coast	17.9	19.3	21.1	20.7	18.9	20.2	18.9	19.7	20.1
Mountains	11.6	13.2	15.2	15.4	12.9	14.4	12.9	13.9	13.7
Inland_north	12.7	14.1	16.3	16.5	14.1	15.7	14.2	15.2	15.1
Inland_central	13.1	14.8	16.5	17.0	14.6	16.0	14.6	15.6	15.4
Inland_south	13.4	15.1	17.0	17.2	14.7	16.3	14.8	15.8	15.6
Study Area	**13.7**	**15.3**	**17.2**	**17.4**	**15.0**	**16.5**	**15.1**	**16.0**	**16.0**
Annual									
Coast	17.8	17.8	18.2	17.9	17.6	17.5	18.1	18.1	18.8
Mountains	11.7	12.0	12.3	12.3	11.6	11.3	12.2	12.3	12.7
Inland_north	13.0	13.2	13.6	13.7	13.1	12.8	13.5	13.7	14.1
Inland_central	13.3	13.7	13.9	14.0	13.4	13.1	13.8	14.0	14.4
Inland_south	13.5	13.9	14.1	14.1	13.5	13.2	14.0	14.1	14.5
Study Area	**13.9**	**14.1**	**14.4**	**14.4**	**13.9**	**13.6**	**14.3**	**14.4**	**14.9**

A major incentive for using RCM in climate impact research is its capability to

characterize extreme events. Normally, extreme weather happens swiftly and over a

small geographical area, hence RCMs are mostly appropriate for examining these events. One particular event is the annual occurrence of warm spell days, indicated by the heat wave frequency index (HWFI) defined as annual count of days with at least 6 consecutive days when the daily Tavg exceeds the 90th percentile of a 5-day window centered on each calendar day of the reference base year 2008, and is illustrated in Fig. 5-2. For RCP 4.5, this index increases predominately over the mountains and inland regions, with a peak in 2029 (66 days on the average and 4 episodes), while the warming on the coast remains minimal during the extreme future years considered (only 2 episodes). The picture is somewhat the same for the coast in RCP8.5 until the middle of the century when the warm spells intensify over the entire territory. Regardless of which RCP is considered, increases in this index are found in the mountainous areas during all simulated years (4 episodes on average over this region), which increases the vulnerability of the whole region given the effect on snowmelt that is essential for groundwater recharge of utmost importance for water supply, agriculture, and the economy.
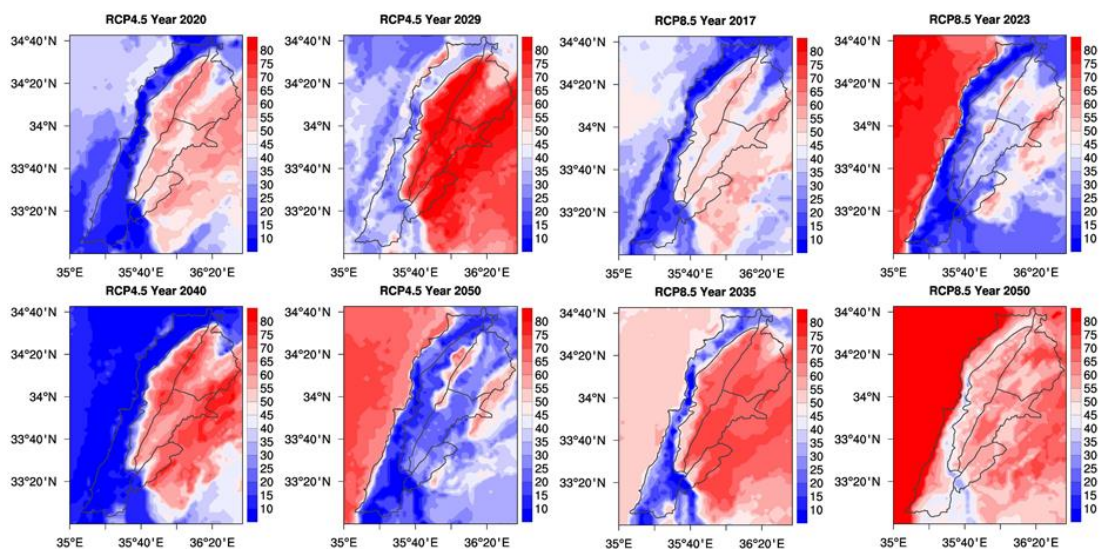
Fig. 5-2 HWFI (days) for RCP4.5 and 8.5 with reference to the year 2008

Under current conditions, a significant fraction of energy is consumed for heating during cold weather. With higher temperatures under a changing climate, it would therefore be logical to expect decreased heating demand during the colder part of the year, but this might not occur since it seems that the winters are cooling. This hypothesis was investigated for both RCP4.5 and 8.5 with reference to the baseline year 2008 (refer to Table 5.3) using the heating degree days (HD). This number increased in all regions during all simulated years in RCP4.5 and two years in RCP8.5. During the other two years in RCP8.5, the HD remained practically the same in 2023 and modestly decreased by mid-century (2050) in the same RCP. The most affected area in both RCPs is the coastal zone where the increase in HD reaches 11% on average during RCP4.5 and 7% during RCP8.5, compared to an increase of 5% in RCP4.5 and 3% averaged over the whole study area. This is consistent with the reduced winter-time temperature presented in Table 5.2, and with the increase in extreme minimal temperature that will be discussed in a subsequent section. However, over longer periods of time, temperatures in the Middle East are projected to continue to increase (Bou-Zeid and El-Fadel, 2002; Barrera-Escoda *et al.*, 2014; IPCC, 2013). Hence, the trend of decreasing numbers of HD in RCP8.5 is likely to continue and most likely to accelerate.

Table 5.3. Projected HD in RCP4.5 and 8.5 with respect to year 2008

	Ref.	RCP4.5				RCP8.5			
Region	**2008**	**2020**	**2029**	**2040**	**2050**	**2017**	**2023**	**2035**	**2050**
Coast	804	848	912	901	912	1016	785	859	769
Mountains	2270	2316	2369	2333	2392	2575	2222	2288	2141
Inland_north	2022	2069	2160	2088	2161	2294	2031	2038	1915
Inland_central	1913	1939	2067	1987	2033	2193	1909	1931	1812
Inland_south	1820	1858	1984	1924	1961	2113	1814	1868	1726
Study area	**1766**	**1806**	**1898**	**1847**	**1892**	**2038**	**1752**	**1797**	**1672**

5.3.2 *Maximum Temperatures (Tmax)*

Fig. 5.3a and b show the yearly maximum temperature (Tmax) between the reference hot year 2008, and the simulated extreme hot years from RCP4.5 and RCP8.5, respectively. This represents the maximum near-surface air temperature; its increase is mostly pronounced in the central inland region where in 2029 it exceeds the 2008 reference by 5.9°C in RCP4.5, whereas the change along the coast remains minimal in the same scenario. In RCP8.5 and during 2035, the warming is drastic inland with the largest increases in the northern areas (6.9°C), while the central part at a near similar high increase reaching 6.2°C. Overall the project area, Tmax are expected to increase by 1% (coast) and 13% (central inland) in RCP4.5 and between 5% (coast) and 15% (central inland) in RCP8.5 with respect to the reference year 2008, and the central inland region experiencing the worst warming on average. These results are consistent with previous findings for the Mediterranean area (Gonçalves *et al*., 2013; Barrera-Escoda *et al*., 2014), but are particularly alarming for health impacts as will be further discussed below when heat waves events are considered.
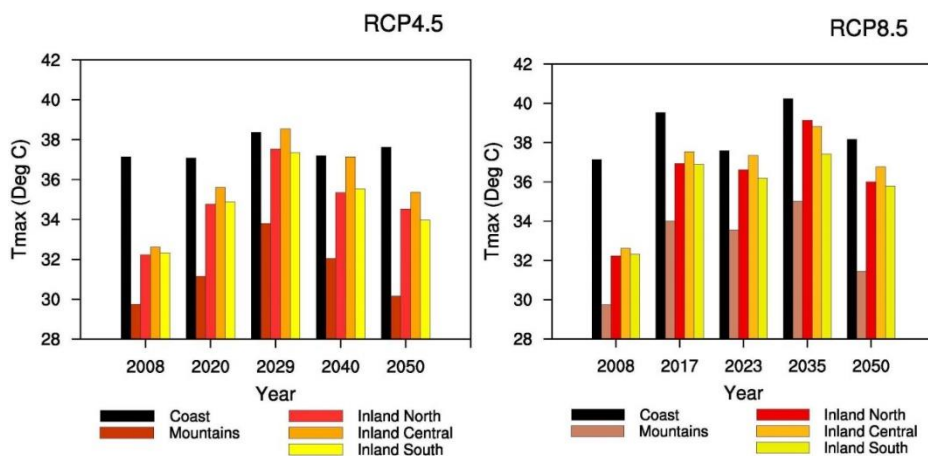
Fig. 5.3. (a) RCP4.5 yearly regional maximum 2m temperature (°C); (b) RCP8.5 yearly regional maximum 2m temperature (°C), with respect to reference year 2008

The consecutive summer days (CSU) are also expected to increase in the next few decades, particularly during the extreme simulated years from RCP4.5 and RCP8.5 as illustrated in Table 5.4. This increase could double in the central inland region, and triple for the mountainous region in years 2029 and 2040 from RCP4.5, in comparison with 2008. The conditions in RCP8.5 aggravate towards the mid of the century where this value will double on the coast, home of the economic and business centers, as well as central inland, hub of the agricultural sector. These results suggest a dramatic increase in drought occurrence with potentially severe adverse consequences to the agricultural sector. The most vulnerable area is the mountainous zone, with an increase of more than 3 folds in the number of CSU.

Table 5.4. Projected CSU (days) in RCP4.5 and 8.5 with respect to year 2008

Region	Ref. 2008	RCP4.5				RCP8.5			
		2020	2029	2040	2050	2017	2023	2035	2050
Coast	51	63	71	71	77	57	74	68	105
Mountains	6	13	19	20	12	14	10	20	21
Inland_north	50	64	78	78	64	62	70	71	79
Inland_central	40	59	83	84	66	57	58	72	78
Inland_south	25	43	54	59	40	33	39	56	59
Study area	**34**	**48**	**61**	**62**	**52**	**45**	**50**	**57**	**69**

Summer days (SU) are defined by a fixed threshold of 25°C for the daily maximum temperature. The spatial variability of the number of SU within the model domain is presented in Fig. 5.4 on the basis of absolute simulated number of summer days per year for both (a) past (2008) (b) worst future year in RCP4.5 (2029) and (c) worst future year in RCP8.5 (2050). It is worth noting that the worst year in an RCP was identified based on an anomaly score taking into consideration both median temperature

and annual precipitation from HiRAM yearly time series (2007-2050) (Chapter4). As such, even warmer years might in fact exist in the HiRAM simulation. Dark orange and brown colors in Fig. 5.4 delineate regions where the number of summer days exceeds 80. Concerning future changes in summer days in RCP4.5 (Fig. 5.4b), a slightly different pattern is observed. Summer days exceeding 80 now spread, especially in the West Mountains that show the most widespread and acute increases (98%), while this increase remains minimal along the coast (11%). As for the inland areas, the increase varies between 23% in the central zone to 25% to the north, reaching 31% in the south. A similar pattern of increase in the number of SU is observed in RCP8.5 (Fig. 5.4c), reaching 14% for the coast, 82% for the mountains, 21% for the central inland, and 26% for the northern and southern inland zones, which indicates that the mountains are the most vulnerable to the increase in the number of summer days.
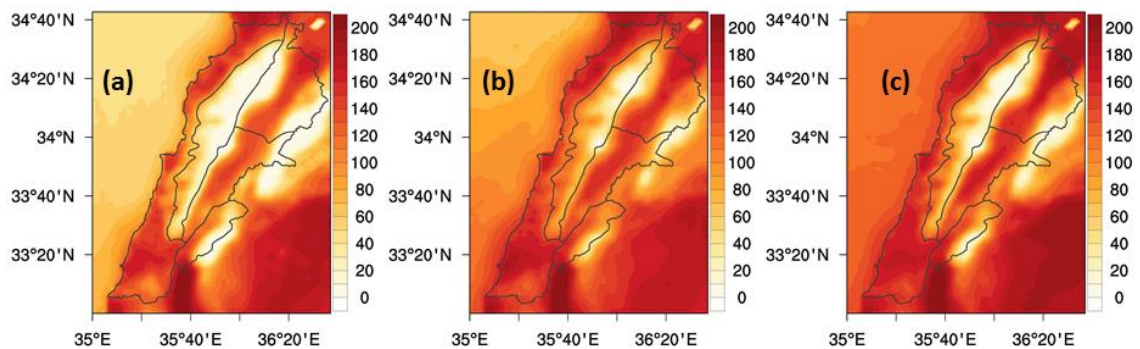
Fig. 5.4. SU (days) (a) year 2008; (b) RCP4.5 year 2029; (c) RCP8.5 year 2050

Fig. 5.5. illustrates the HWDI for the simulated extreme years in RCP4.5 and RCP8.5 with respect to the reference year 2008. As mentioned above, this index which is based on the mean TXnorm>5°C of the daily maximum temperature series of a 5-day

window centered on each calendar day of 2008, is of paramount importance since heat waves are a major cause of weather-related deaths that have broad geographic impacts. This is further exacerbated by the urbanization trends in the region and the potential synergistic interactions between heat waves and urban heat islands (Li and Bou-Zeid, 2013). Here again, the mountainous and the inland regions are the most affected, but the impact will intensify in RCP8.5 to reach the coast. The results of the last 2 decades in both RCPs are somewhat similar, except for the coast, with the year 2050 presenting milder results in both scenarios. As for the heat wave episodes , it varies from 3 events (year 2017 and 2023) to 4 events (year 2050) and reaching 5 events (year 2035) in RCP8.5 while remaining 2 events during year 2020 and 2050, and increasing to 4 events (year 2040) and registering 5 events (year 2029) in RCP4.5.
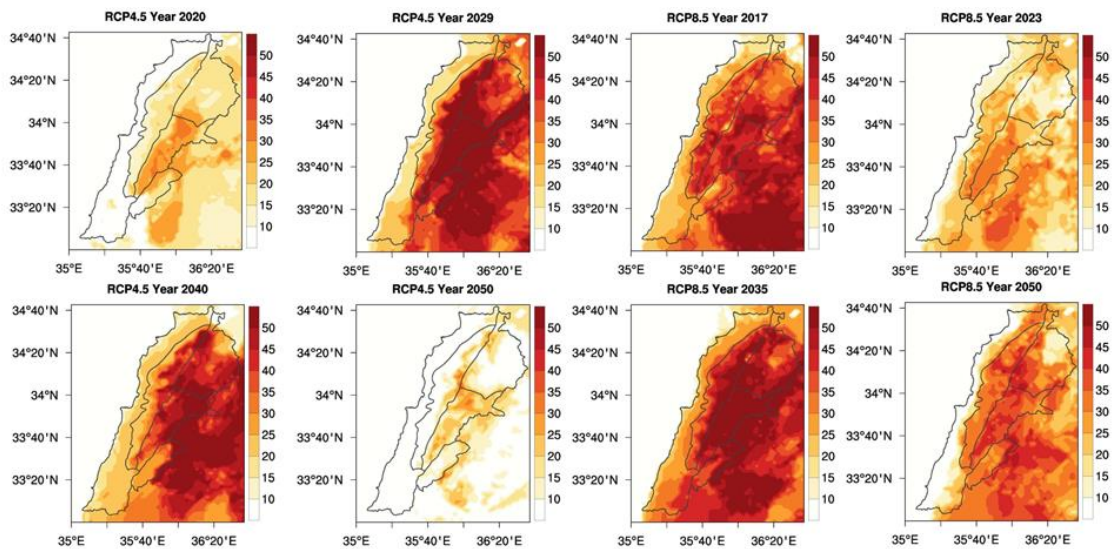
Fig. 5.5. HWDI (days) for RCP4.5 and 8.5 with reference to year 2008

Another index computed relative to the local climate is the percent of very warm days (TX90P), during which the daily Tmax values exceed the reference period (2008) 90th percentile Tmax (Coast: 29°C; Mountains: 23°C; Inland north and central: 28°C and inland south: 27°C). Fig. 5.6 illustrates the spatial distribution of this index for both RCPs. On average and for each RCP, the most vulnerable region is the central inland zone where this index increases by 25% in 2029 (RCP4.5) and 21% (RCP8.5), with potential adverse impacts on agriculture, human health, energy demand and ecosystem resilience. Finally, the drastic increase in TX90P will be on the coast by midcentury in RCP8.5, which confirms with the results obtained in the HWDI presented above.
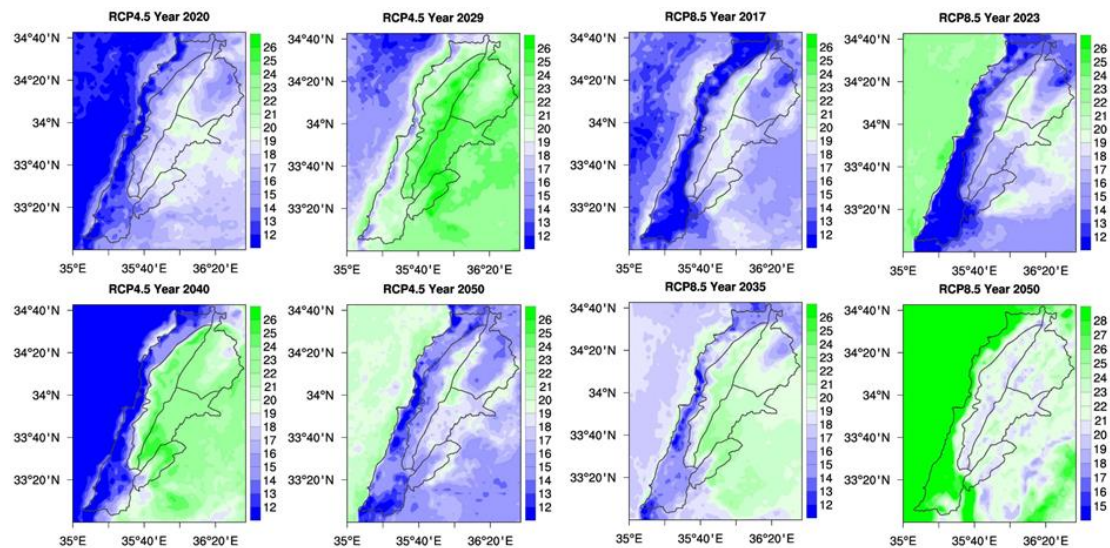
Fig. 5.6. TX90P (°C) for RCP4.5 and 8.5 with reference to year 2008

5.3.3 *Minimum Temperatures*

Fig. 5.7 illustrates the regional yearly minimum temperature for the reference hot year 2008, and the simulated extreme future hot years from RCP4.5 and 8.5. Winter minima are projected to decrease across all regions, and freezing temperatures are even projected for the coastal zone especially in RCP4.5. The extreme minimal temperatures are more pronounced in RCP4.5 than in RCP8.5, where the values decrease on average by 1.7°C in RCP4.5, and by around 0.3°C in RCP8.5. Under RCP4.5, the minimum temperatures are expected to decrease by 4.8°C in northern inland, by 1.6°C along the coast and by 3.9°C in the mountainous areas. As for RCP8.5, the minimum temperature will decrease in the first 3 decades then it will increase by 2050 with respect to the baseline scenario 2008.
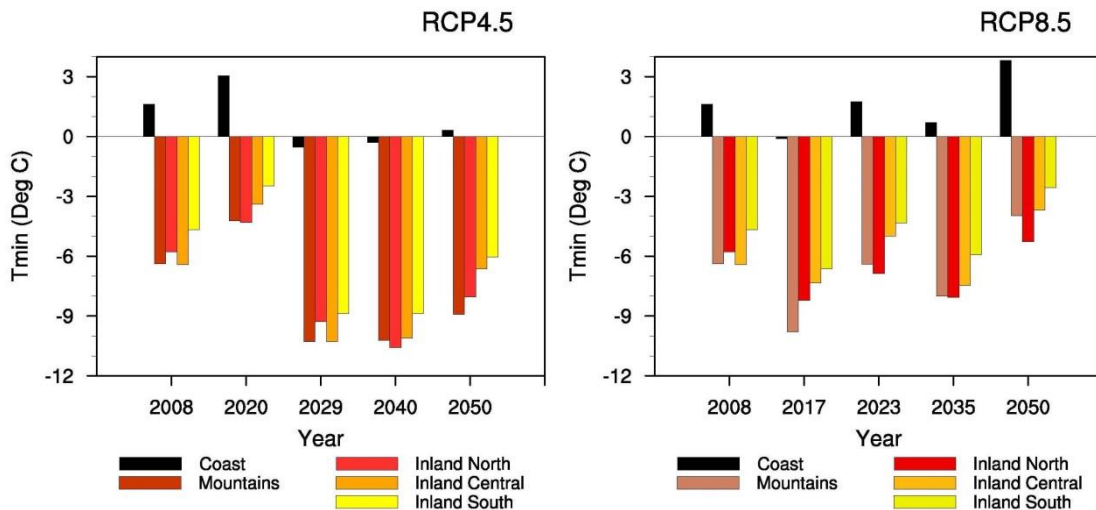
Fig. 5.7. Yearly regional minimum 2m Temperature (°C) for RCP4.5 (a)
and RCP8.5 (b)

Fig. 5.8. illustrates the PDFs of the regional annual minimum temperature for the baseline year 2008, as well as for the future simulated extreme years in RCP4.5 and 8.5 (only one inland region is shown, the other have similar trends). These were obtained by taking the daily minimum temperature series of the reference year 2008 and the 8 future years and dividing them into bins from -15$^{\mathbf{o}}$C to 30$^{\mathbf{o}}$C. For all regions in RCP4.5, the years that are the hottest on average (2029 and 2040) display the strongest decrease in minimum temperatures, showing that seasonal swings will be intense during those years. A general shot to lower temperature can be detected in most PDFs relative to 2008. What is common in all regions is an increase in the frequency of cold and hot minima with a tendency towards greater cold temperatures during the third and fourth decade in RCP4.5, and the second and fourth decade in RCP8.5, a result consistent with the findings in Fig. 5.7. above.
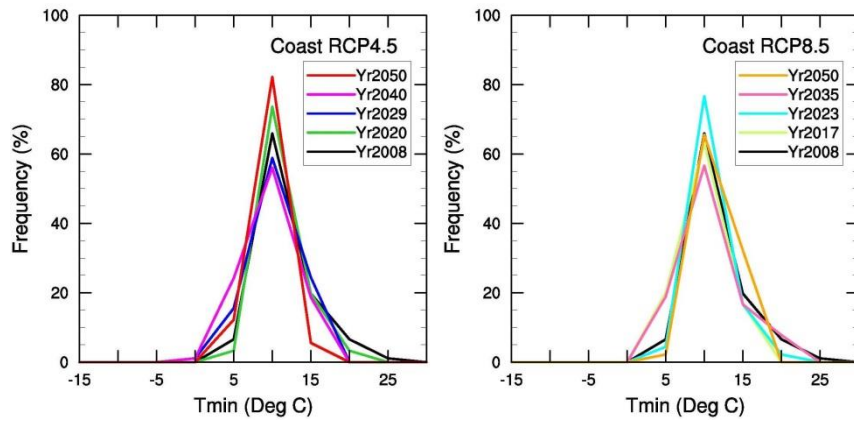
a. Coastal region
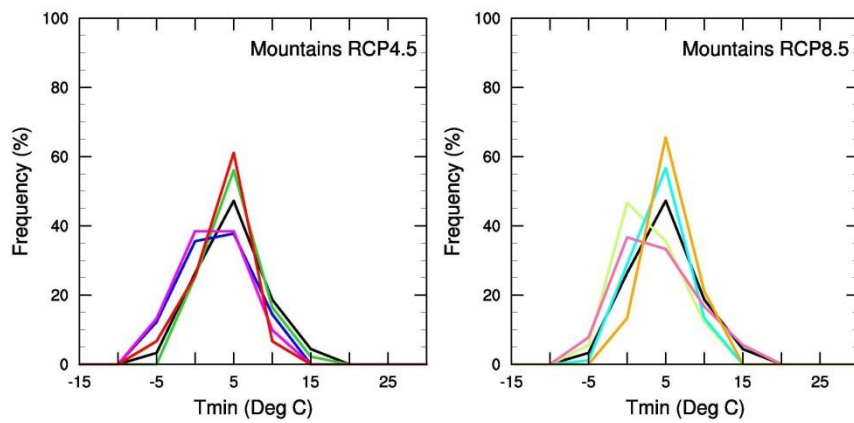
b. Mountainous region
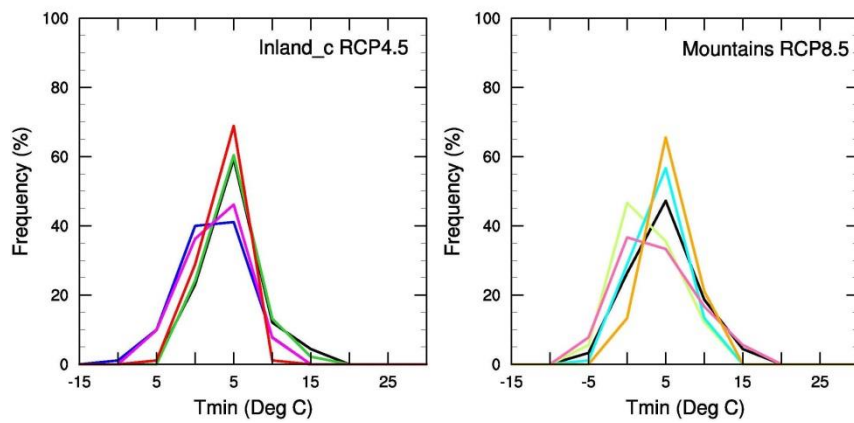
c. Central inland region

Fig. 5.8. PDFs of regional 2m minimum temperature (^{o}C) for RCP4.5 and 8.5

Frost occurs when the surface minimum temperature drops below 0°C due to phenomena such as radiation cooling or cold temperature advection (Meehl *et al*.,

2007), and frost adversely affects crops by freezing cellular tissue and damaging foliage (Ahn *et al*., 2015). It can have significant impacts on the emergence or maturation of plants especially if they occur early or late during transition seasons (Alexander and Tebaldi, 2012). The number of consecutive frost days (CFD) in RCP4.5 would markedly increase by over two folds its value in the control year 2008 during years 2029 and 2040 in all regions (Table 5.5). Even the coastal zone will suffer from a couple of days of frost during those extreme years, a result coherent with the projected extreme minimum temperatures discussed above (Fig. 5.8). One must also not overlook the doubling in the same scenario of the number of frost days in the fertile agricultural region in the central inland, which will lead to adverse consequences on the agricultural yield in that region. The projections in RCP8.5 are milder than those of RCP4.5, and their trend reflects the topographic situation. The CFD number is increasing with increasing elevation and distance from the Mediterranean Sea. In general, in RCP8.5, a decrease in CFD occurrence is projected by the midcentury, which is in accordance with a minor increase in projected regional minimum temperatures (Fig. 5.8.).

Table 5.5. Projected CFD (days) in RCP4.5 and 8.5 with respect to year 2008

Region	Ref. 2008	RCP4.5				RCP8.5			
		2020	2029	2040	2050	2017	2023	2035	2050
Coast	0	0	2	2	1	1	0	1	0
Mountains	12	11	29	27	18	18	13	16	8
Inland_north	9	9	25	24	14	16	12	14	8
Inland_central	10	8	20	23	12	14	11	13	7
Inland_south	9	6	23	21	9	13	9	13	4
Study area	**8**	**7**	**20**	**19**	**11**	**12**	**9**	**11**	**5**

Fig. 5.9. depicts the warm night index (TN90P), which is the percent of the time that daily Tmin values exceed the reference period (2008) 90th percentile Tmin (Coast: 23°C, Mountains, Inland north and central: 21°C, and Inland south: 22°C) for both RCP4.5 and 8.5. A high minimum temperature is particularly harmful to human wellbeing and high night-time temperatures combined with elevated levels of relative humidity in August 2003 attributed to a large extent to the detrimental effect of the heat wave of that year in Europe (Souch and Grimmond, 2004; D'Ippoliti *et al*., 2010). In general, TN90P follows the same trend as TX90P across all regions in RCP4.5 when comparisons are made with Fig. 5.6. On average, the night time warm spells are less pronounced along the coast, while the remaining regions exhibit a similar level of warming in RCP4.5 with a decrease in TN90P towards 2050. The situation is somehow reversed in RCP8.5, with the highest percentage of warming happening by 2050 and affecting the coastal zone more than the other regions in all other simulated years or RCPs. This is in line with the result presented in Fig. 5.7, where the Tmin along the coast in 2050 (RCP8.5) is the highest amongst all values and the lower number in CFD (Table 5.5).
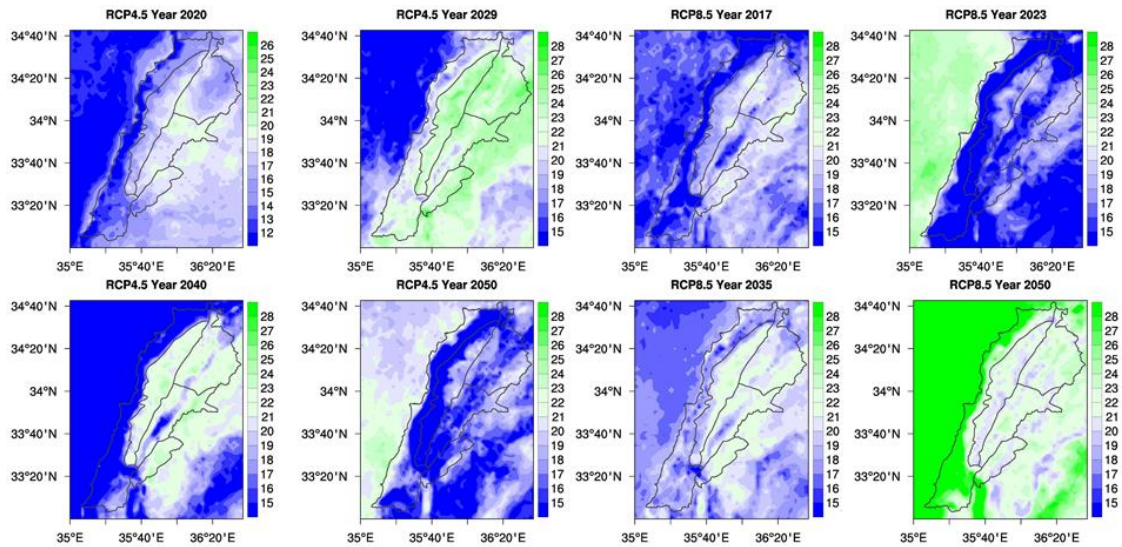
Fig. 5.9. TN90P (^{o}C) for RCP4.5 and 8.5 with reference to year 2008

5.4 Conclusion

In this chapter, the regional climate model WRF was used to downscale future climate simulated by the HiRAM GCM over a complex topographical terrain along the eastern Mediterranean, for both the RCP4.5 and RCP8.5 scenarios. The simulations covered the past extreme dry year (2008) as a baseline reference, and one future (2011–2050) extreme year per decade from each scenario: 2020, 2029, 2040 and 2050 from RCP4.5 and 2017, 2023, 2035 and 2050 from RCP8.5. The projected climate change signal assessed the average, maximum and minimum temperature with a focus on extreme events that can cause significant economic and social damage and disruption (Easterling *et al*., 2000, IPCC, 2013), as well as seasonal and regional differences over the study region.

RCP 4.5 and 8.5 future climate projections tend to produce decreases of average air temperature in the winter and spring (although this trend is reversed in RCP 8.5 by the mid-century), and increases in the summer and fall. The yearly means are

124

therefore not adequate to assess the impacts of climate change on the region since they show milder increases than summertime temperatures. The temperatures are as expected warmer in RCP 8.5 than RCP 4.5. Regional differences were also significant, with the largest effects noted in the mountains and central inland regions. This is accompanied by an increase in the warm spell duration index (HWFI) in these areas, which can even extend to the coast by 2050 in RCP8.5 and influence snowmelt and water resources.

Regarding the maximum temperatures, all WRF simulations project a warming over the study region with different intensities depending on the year and/or RCP under consideration, with the worst case scenario occurring in the central inland and the mountainous regions. The number of consecutive summer days will double in the central inland, while it will triple over the mountains, affected also by the highest increase in the number of summer days. The mountains region is particularly important since the increase in near-surface air temperature will lead to more winter precipitation falling as rain instead of snow and earlier snow melt, which can influence the occurrence of extreme events such heat waves and floods. Regarding minimum temperatures, winter minima are expected to decrease across all regions, and freezing temperatures are even projected for the coastal zone especially in RCP4.5. During the same scenario, the consecutive number of frost days (CFD) will double in the inland region, which will lead to adverse consequences on the agricultural yield in that area. Therefore, the most striking finding is the drastic rise in inter-seasonal variability, even when yearly-average trends do not appear significant.

The results of this chapter suggest that, irrespective of the emission scenario considered, future changes in extreme weather systems may have a substantial effect on the study area, which is already subject to water scarcity challenges. Seasonal

differences are more important than yearly mean trends and should be considered when impact and adaptation scenarios are developed. Furthermore, impacts vary across regions over this complex terrain, and this variability requires downscaling simulations to capture and take into consideration. Particularly critical are extreme hot weather episodes, which are expected to increase by the mid of the twenty-first century.

CHAPTER 6

DOWNSCALING OF CLIMATE CHANGE IMPACTS ON SILAGE MAIZE YIELD IN SEMI-ARID REGION

6.1   Introduction

Future climate change is expected to alter water availability (Díaz-Ambrona *et al*., 2004; Anwar *et al.*, 2007; Abraha and Savage, 2008; Laux *et al*., 2010), which is essential to plant growth, and hence its impacts on agriculture are going to be pronounced. Given that more than 80% of total global agricultural areas is rain-fed, changes in future precipitation due to climate change will affect total yield production (Olesen and Bindi, 2002; Tubiello *et al*., 2002; Reilly *et al*., 2003). Globally, irrigated agricultural land covers less than one-fifth of all cropped surfaces but yields around 45% of the world's food (Döll and Siebert, 2002); the source of this water is mainly from groundwater aquifers or rivers located in watersheds that are often distant from the irrigated lands and could be in different climatic environments (Gornall *et al*., 2010). Therefore, even irrigated agriculture might be affected by climate change. Thus far, global warming alone has been estimated to have resulted in an average annual combined losses of 40 Million tons of crop yield per year since 1981 (Lobell and Field, 2007), but other hydrometeorological modifications resulting from climate change will also alter crop yields. Potential increases in winter temperatures will reduce snowfall and change its timing, both of which will alter the natural systems governing water storage and release. Moreover, the decrease in precipitation will affect the runoff amount, especially at the onset of snowmelt in the spring season (Gornall *et al*., 2010). Rising evaporative demand resulting from increasing temperatures, caused by the

escalation of greenhouse gases (GHGs) (IPCC, 2013), and extended growing seasons will also impact the irrigation requirements that are estimated globally to be in excess of 5 to 20% by the end of the twenty first century in comparison with the present conditions (Döll, 2002; Fisher *et al.*, 2007).

The impact of climate change on the yields of silage maize (a C_4 plant) is a global concern (Abraha and Savage, 2006). It is a widely used crop and popular forage for livestock due to (1) high yields of high-energy feed per area, (2) high digestibility, (3) can be stored directly at harvest when plant characteristics are near ideal, (4) rapid harvest, and (5) low-cost storage (Wheaton *et al.*, 1993; Schroede, 2004). The annual production of silage maize was 487 million tons in 2013 worldwide (Food and Agriculture Organization, 2013) and it is the third ranked cultivated cereal in Lebanon, country subject of this study, where the production reached 900 hectares in 2005 (Lebanon SNC, 2011). Yet, the cultivation of maize is very sensitive to climate (Tubiello *et al.*, 2000; Gornall *et al.*, 2010; Díaz-Ambrona *et al.*, 2013). High yields are obtained with a combination of good crop and silage management practices and optimum weather conditions. In fact, the growth and maturity of a maize hybrid are closely related to daily and seasonal temperatures with a need to sow maize seeds in warm, moist soil for germination. A delayed planting date past early May can result in 1% grain loss per day (Lee *et al.*, 2006). On the other hand, periods of high relative humidity, frost, and hail are known to reduce the yield and the quality of the maize. Moreover, high temperatures during the reproductive development are particularly damaging to maize at tasseling, when the plant has reached its full height and begin to shed its pollen. If temperatures exceed 36°C during this vegetative growth period, reduction in pollination occurs (Gornall *et al.*, 2010).

Changes in crop yields in response to changing climatic conditions are often assessed through the use of crop simulation models (Abraha and Savage 2006). Process-based models of crop growth, such as CropSyst (Stöckle *et al*., 1994; Stöckle *et al*., 2003; Stöckle *et al*., 2014), use daily weather data to evaluate the impact of climate change on maize production (Tubiello *et al*., 2000; Torriani *et al*., 2007a & b). CropSyst allows for the simulation of yields under multiple possible climate change scenarios once it is calibrated for the simulation sites of interest. The model can also be used to assess the impact of diverse adaptation schemes on the yield of simulated crops in an effort to improve harvest under climate change (El Afandi *et al*., 2010). Several attempts have been made with Cropsyst to examine the potential impacts of climate change on the grain yield of maize at various locations worldwide (Tubiello *et al*., 2000; Díaz-Ambrona *et al*., 2004; Abraha and Savage, 2006; Torriani *et al*., 2007a & b; Tingem *et al*., 2009a & b; El Afandi *et al*., 2010; Laux *et al*., 2010; Boggia *et al*., 2013; Díaz-Ambrona *et al*., 2013; Holzkämper *et al*., 2015; Ouda *et al*., 2015). Yet, most of these studies either used climate scenarios generated from global circulation models (GCM) or synthetic climatic scenarios generated from stochastic weather generator (e.g., Climgen; Nelson, 2002). While GCMs simulate several facets of the climate system and corresponding interactions (Murphy *et al*., 2004), they use horizontal grid spacing on the order of hundreds of kilometres. Hence, the coarse grids of GCMs preclude accurate capturing of extreme events, such as heat waves, drought and floods, that are deemed critical when utilizing their projections in climate-change impact studies at the regional and local levels. These limitations are exacerbated over complex terrain where the important effect of orography on precipitation cannot be captured by

coarse models (Giorgi and Mearns, 1991; Wang *et al*., 2004; Giorgi, 2006; Argüeso *et al*., 2012; Berg *et al*., 2013).

In this chapter, results from a dynamical high-resolution (3km) downscaling effort were coupled with CropSyst over a complex topographical domain in the eastern Mediterranean basin with two objectives in mind: (1) to assess the impact of climate change on the yield and consumptive water use of silage maize (*Zea Mays* var Oropesa) under two Representative Concentration Pathways (RCPs) 4.5 and 8.5 (IPCC, 2013), and (2) to determine the effectiveness of adaptation strategies in improving the yield and water productivity of silage maize under these scenarios. The study focused on future extreme dry and hot years from both RCPs in comparison with a past extreme dry and hot year to gage the worst-case impacts of climate change.

6.2 Methods

6.2.1 *Modeling domain and data sources*

The observational data used in this study were obtained from irrigated field experiments conducted at the Agriculture Research and Education Center (AREC) of the American University of Beirut (AUB) located along a high altitude plain in the semi-arid inland region of Lebanon (latitude 33°55'N, longitude 36°05'E, elevation 995m) (Fig. 5.1c). Established in 1953, AREC is among the largest non-profit agricultural research and education centers in the Middle East, encompassing 100 hectares of research facilities and agriculture land (http://www.aub.edu.lb/fafs/arec/Pages/index.aspx). AREC was selected as a pilot study area for the reason that it has its own weather station operating since 1956, agricultural land producing forage crops, fruits, and vegetables, and an irrigation system, all with

archived records for crop yields, soil and management procedures (irrigation, fertilization, etc.). Hence, this site is representative of crops-growing conditions in Lebanon and similar Mediterranean climates. The long-term (1978-2008) annual average precipitation of 512 mm is mostly concentrated during the autumn and winter seasons. The mean annual temperature is 15.1°C with a maximum in August that often exceeds 35°C and a minimum of approximately -5°C in February. The soil is alkaline (pH ≈8.0) and gravelly clayey (Yau and Rayan, 2013). Long-term meteorological characteristics for the site are presented in Table 6.1 as obtained from AREC, and soil characteristics in Table 6.2.
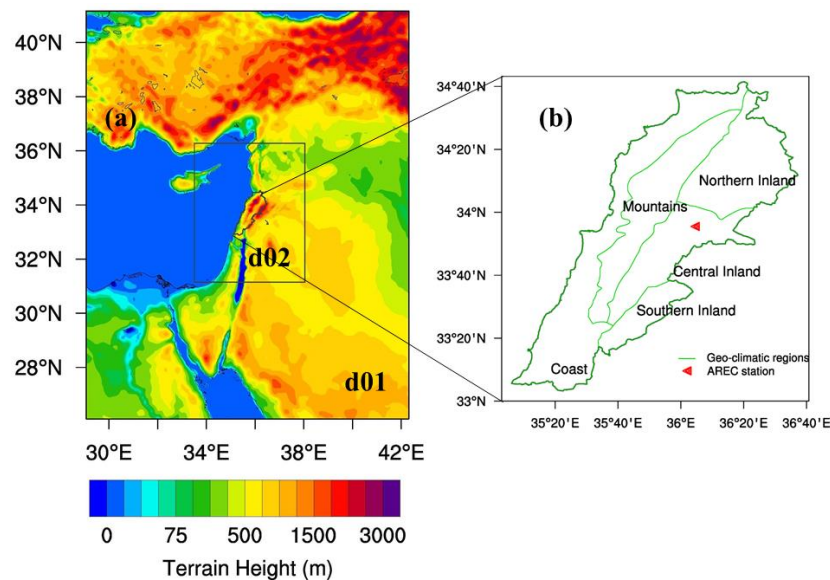
Fig. 6.1. (a) Eastern Mediterranean basin showing WRF's 2 domains (9:3 km) configuration and topographic features of the study area, (b) AREC location and the geo-climatic regions

Table 6.1. AREC Long term (1978-2008) average monthly maximum (Tmax), minimum (Tmin), average (Tavg) temperature, total rainfall (PP), sunshine hours, relative humidity, wind speed and evapotranspiration

Month	Tmax (^{0}C)	Tmin (^{0}C)	Tavg (^{0}C)	PP (mm)	Relative Humidity (%)	Wind Speed (m/s)	Sunshine (hrs)	ET0* (mm/day)
January	16.6	-4.7	4.2	111	74.6	1.55	5.2	1.72
February	18.7	-4.4	5.0	109	69.0	1.82	5.9	2.26
March	22.6	-3.1	9.2	76	58.3	1.83	6.7	3.35
April	28.9	0.1	14.8	26	48.9	1.89	8.1	5.05
May	32.3	2.9	18.2	12	43.5	1.83	9.7	6.07
June	35.2	6.8	22.1	2	39.8	1.91	11.5	6.68
July	36.9	10.4	25.6	0	32.4	1.87	11.7	6.81
August	36.6	10.1	25.0	0	36.4	1.77	11.1	6.23
September	34.7	7.7	21.7	1	40.8	1.68	9.6	5.12
October	31.7	4.3	16.6	20	57.2	1.60	7.9	3.66
November	24.3	-0.8	11.6	55	56.0	1.53	6.6	2.5
December	19.6	-3.9	6.7	99	67.0	1.50	5.1	1.69
Annual	28.2	2.1	15.1	512	52.0	1.73	8.2	1559.2

* ET_0 is calculated by AREC as the average of 12 years ET0 (1988-2000)

Table 6.2. Soil characteristics at AREC

	Mean values (0 - 1.5m)
Bulk density (g/cm^3)	1.25
Permanent wilting point (m^3/m^3)	0.21
Field capacity (m^3/m^3)	0.44
Sand (%)	10
Silt (%)	27
Clay (%)	63
pH	7 – 8
Cation exchange capacity (meq/100g)	32.8 – 37.7

The yearly growing season of silage maize (*Zea Mays* var Oropesa) in AREC is from May to October under an automatic sprinkler irrigation regime of 485 mm/ha following the schedule in Table 6.3. All plots in AREC are pre-irrigated before planting to ensure adequate moisture in the soil profile at planting time. Nitrogen (300 kg/ha) is spread by hand as ammonium nitrate to the silage maize plots post emergence in the vegetative phase one week prior to tasseling, while a 17-17-17 balanced ratio blend of

Nitrogen, Phosphorus and Potassium (700 kg/ha) is applied on sowing day. Yields of

crop dry matter are maximized near 65% soil moisture by mass and losses during

feeding, storage, and harvesting are minimized (Roth and Heinrichs, 2001). Harvest

usually takes place 5 days after physiological maturity when the whole corn plant will

have a dry matter of 32 to 38 percent, the corn kernel contains about 62 to 65 percent

dry matter; and ear corn contains about 55 to 60 percent dry matter, prior to black layer

formation at the tip of the kernel (Ashley, 2001). It is worthwhile to mention that loss of

plant nutrients as a result of surface runoff is not considered in this work due to the

minimal runoff amount occurring rarely at AREC during the silage maize growing

season (May to October).

Table 6.3. Irrigation schedule for the silage maize season

Days after sowing	Water amount (mm)
7	30.8
14	30.8
21	30.8
28	30.8
35	30.8
42	30.8
49	30.8
56	52.1
63	52.1
70	41.3
77	41.3
84	41.3
91	41.3
Total	**485.0**

6.2.2 *Modeling Framework*

The modeling framework used in this study consists of a top down approach where the outputs of a high resolution GCM (HiRAM) are dynamically downscaled by a high resolution RCM (WRF) for past and for future selected extreme dry and hot years under two RCPs. The resulting outputs of daily climate variables (temperature, precipitation, wind, humidity, and solar radiation) are then relied upon to force a crop model (Cropsyst) at the local pilot area (AREC) described in the previous section in order to obtain past and future silage maize crop yields and related irrigation water demands during these extreme hot and dry years. Local past observed weather data at AREC and collected field data (crop cultivar, phenology, yields, soil, irrigation, fertilization and other management practices), were used to calibrate the crop model. After calibration, the model was validated using the measured data of silage maize yields. Different adaptation and mitigation strategies are then proposed and assessed in order to reduce the impact of climate change on crop yields and water demands (Fig. 6.2).
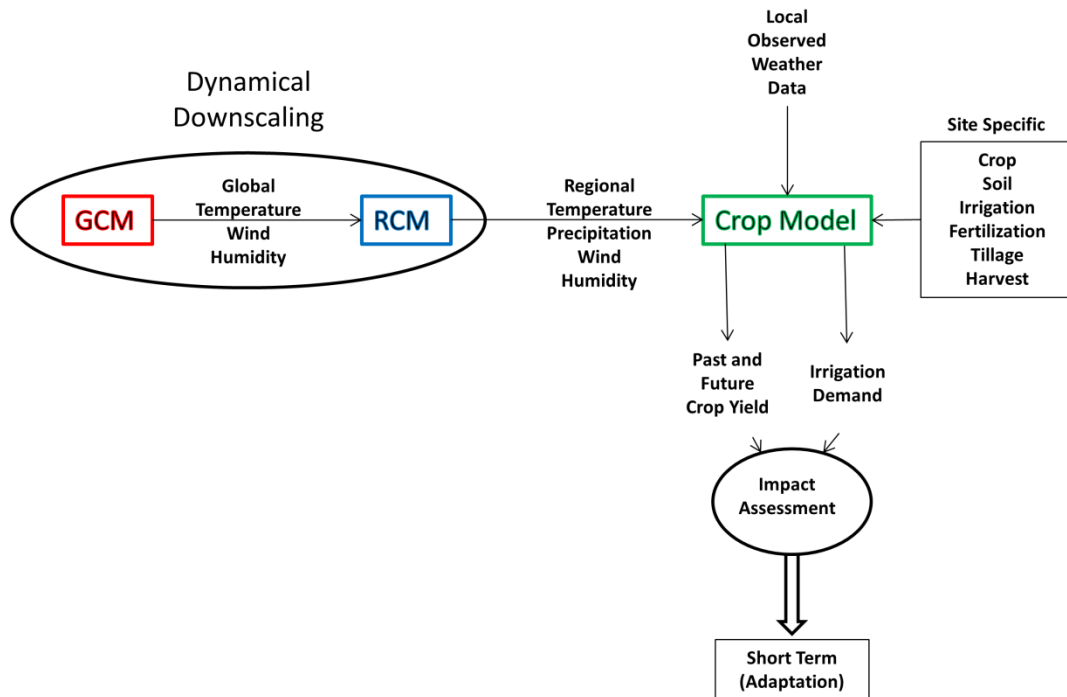
Fig. 6.2. Adopted top down approach flowchart

6.2.2.1 Climate Models

WRF (Skamarock *et al*., 2008) model is a next-generation mesoscale numerical weather prediction system that serves both operational and research communities (Heikkilä *et al*., 2011). For this study, two one way nested computational domains of horizontal resolutions of 9 km and 3 km, respectively, have been set (Fig. 6.1a). The highest resolution of 3km was shown to be sufficient in previous tests comparing historic WRF simulations over the study area to a wide range of observational data; no significant difference in errors was noted when the resolution was further increased to 1 km with model set-up, parameterization and evaluation detailed in Chapter 2.

Initial and boundary conditions for the RCM were obtained from the High Resolution Atmospheric Model (HiRAM)'s past and future simulations. The time interval of the boundary data is 6 hours, and the sea surface temperature (SST) was also

updated every 6 hours (Bangalath and Stenchikov, 2015). One past dry and hot year

(2008) forced by HiRAM was simulated and employed as a baseline scenario to allow

for comparison and quantification of the changes. Then eight future yearlong

simulations were performed to generate extreme climate projections over the project

area (Fig. 6.1b), four from RCP 4.5 (2020, 2029, 2040 and 2050) and four from RCP

8.5 (2017, 2023, 2035 and 2050). These critical past and future years were selected

based on an anomaly score that relies on the mean annual temperature and accumulated

precipitation from HiRAM daily time series to identify the worst year per decade from a

water resources perspective (refer to Chapter 4 for a detailed description of the anomaly

score and the years' selection process). The reason behind this selection is that the

influence of global warming on the project area can be assessed by comparing the past

and future statistics of various meteorological fields from years selected precisely to

have extreme hydro-meteorological events such as heat waves, intense storms, or

drought periods. Our downscaling simulations do not aim to reproduce decadal-means

or average climatological conditions, the trends of which are reasonably captured by

GCM outputs despite their shortcomings. Our focus is rather on extreme years where

the impacts are the largest. RCP4.5 is a stabilization scenario in which total radiative

forcing is stabilized shortly after 2100, without overshooting the long-run radiative

forcing target level (Smith and Wigley, 2006; Clarke *et al*., 2007; Wise *et al*., 2009). As

for RCP8.5, it is characterized by increasing GHG emissions over time, representative

of scenarios in the literature that lead to high GHG concentration levels (Riahi *et al*.,

2007).

6.2.2.2 <u>Crop Simulation Model</u>

The CropSyst model was used to examine the potential effects of future climate change on the productivity of silage maize (*Zea Mays* var Oropesa) yields. CropSyst is a daily time step, multiyear, multicrop simulation model designed to predict crop growth and development, crop yield, daily residue loss, nitrogen leaching, soil erosion, weather and management (irrigation, fertilization, residue, and tillage) (Stöckle and Nelson, 2003). The model simulates a single land block fragment, which represents a biophysically homogeneous unit area with a uniform management routine (Stöckle *et al.*, 2003). The three essential components of the model are the water balance, the nitrogen balance, and crop growth. The water budget in CropSyst includes irrigation and precipitation, interception and runoff, infiltration and redistribution, potential and actual evaporation, and water uptake. Potential crop growth, expressed as biomass increase per unit area, is based on a minimum of four limiting factors: light, temperature, water, and nitrogen (Stöckle *et al.*, 1994). Crop development is simulated on the basis of the accumulated thermal time or growing degree days (GDD) required to reach each vegetative stage, and the production rate of biomass is simulated by capturing either radiation or water, depending on the most limiting factor among them (Bouazzama *et al.*, 2013). Details on the use, parameterization, and execution of the model can be found in Stöckle and Nelson (2003).

The model has been evaluated in many locations by comparing model estimates to data collected in field experiments for several crops (Pala *et al.*, 1996; Donatelli *et al.*, 1997; Confalonieri and Bechini, 2004; Jalota *et al.*, 2006; Benli *et al.*, 2007; Abraha and Savage, 2008; Tatsch and BindiM, 2009; El-Baroudi *et al.*, 2013; Singh *et al.*, 2013) with good performance reported in predicting yield and biomass in

response to water management for maize (Morari *et al*., 2001; Bellocchi *et al*., 2002; Sommer *et al*., 2007; Bonfante *et al*., 2010; Bouazzama *et al*., 2013). All of these studies used low-resolution weather data from direct outputs of GCMs or generated using Cropsyst weather generator, ClimGen that generates precipitation, daily maximum and minimum temperature, solar radiation, air humidity, and wind speed using existing weather data. The performance of ClimGen has been evaluated in several studies with good agreement between simulated and observed weather parameters (Castellvi and Stöckle, 2002; McKague *et al*., 2005; Safeeq and Fares, 2011; Esquivel *et al*., 2015). The limitation with ClimGen is that it produces climate variables on a 0.5 x 0.5 degree grid by combining GCM-resolution climate change data derived from the pattern scaling method at a 5 degree resolution with observations of climate at half – degree resolution to simulate future climates at half-degree resolution. This coarse resolution cannot resolve complex topography, coast lines, land use and surface heterogeneities. A better alternative is to use data from dynamic downscaling that consists of driving an RCM at high resolution by the output of a GCM for the concerned region (Wang *et al.* 2004) to produce a more representative regional climate with fine-scale topographies that are lacking in GCMs (Antic *et al*., 2004). For this purpose, weather station data, measured daily at AREC are used to parameterize Cropsyst for the past calibration and validation simulations. Once the model is calibrated and validated, the climate variables outputs at a 3km resolution from WRF are used as input to Cropsyst for past (2008) future (RCP 4.5: 2020, 2029, 2040 and 2050; and RCP 8.5: 2017, 2023, 2035 and 2050) simulations. As such, ClimGen is only relied upon to populate the missing observed data in daily weather for past simulations at AREC.

6.2.3 *Analysis and Data Handling*

Daily weather data (as summarized in Table 6.1) from AREC weather station covering the period 1978 to 2008 were used as an input to Climgen (version 4.06.08) weather generator (Nelson, 2002) to parameterize Cropsyst (version 4.19.06) for the project area and generate daily missing observed weather parameters such as dew point data, which were not available. We also used Climgen to generate missing daily weather data in the observed daily time series (precipitation, maximum and minimum temperature, solar radiation, maximum and minimum relative humidity, and average wind speed). Solar radiation was calculated from sunshine duration hours using Angström's (1924) equation. We used the recorded planting dates and silage maize yields during the years 2004 and 2005 for Cropsyst calibration under unstressed conditions. Validation was conducted under stressed conditions for the years 2006 to 2008 by running the calibrated model with on-site planting dates and comparing the site observed and predicted silage maize yields as recommended by Donatelli *et al.* (1997). Reference evapotranspiration ET0 was calculated by Cropsyst using the Penman–Monteith equation (Allen *et al*., 1998). Water redistribution in the soil was simulated using the cascade approach (Romano *et al*., 1998).

The values of required Cropsyst input parameters, listed in Table 6.4 below, were either taken from the CropSyst manual (e.g., unstressed harvest index) (Stockle and Nelson, 2003) or from other literature sources (e.g. base and cutoff temperatures) or calibrated based on values observed in the field by AREC (e.g. growth periods). The calibration consisted of slight adjustments of selected crop input parameters (e.g. above ground biomass-transpiration coefficient (Tanner and Sinclair, 1983), radiation-use efficiency (Monteith, 1981)) to obtain the smallest errors between the observed yields

and Cropsyst predicted yields. These adjustments were around values that were either typical for silage maize or known from previous experiences with Cropsyst (Donatelli *et al.*, 1997; Torriani *et al.*, 2007b; Bouazzama *et al.*, 2013; Díaz-Ambrona *et al.*, 2013).

Statistical indices used to test the goodness between observed and predicted (i.e., simulated by cropsyst) grain yields in each growing season were calculated for the calibration (2004-2005) and validation (2006, 2007 and 2008) of Cropsyst. The indicators of performance were: (1) the percentage root mean square error (%RMSE) (Jamieson *et al.*, 1998); (2) the coefficient of determination (R2); (3) the Willmott index of agreement (WI) (Willmott, 1982); and (4) the residual mass coefficient (CRM) (Addiscott and Whitmore, 1987) (Table 6.5).

Table 6.4. CropSyst crop parameter values used for silage maize

	Value	Unit	Source
Emergence	100	GDD[**]	Calibrated
End of new leaf growth	800	GDD	Calibrated
Begin flowering	900	GDD	Calibrated
Begin grain filling	1200	GDD	Calibrated
Maturity[*]	1620	GDD	Calibrated
Specific leaf area at optimum	20	m^2/kg	Manual
Stem/leaf partition coefficient	3		Manual
Unstressed harvest index	0.48		Manual
Above ground biomass transpiration coefficient	12	Pa	Calibrated
Base temperature	10	^{0}C	Literature
Cutoff temperature	30	^{0}C	Literature
Mean daily temperature that limit growth	25	^{0}C	Manual
Leaf area duration	800	GDD	Calibrated
Radiation use efficiency	3.9	g/MJ	Calibrated
Maximum root depth	1.5	m	Manual

[*] Harvest is assumed to take place 5 days after maturity
[**] (GDD) growing degree days

Table 6.5. Performance indicators used to evaluate model performance

Statistical variable	Description	Equation	Optimum value
RMSE	Root mean square error	$RMSE = \sqrt{\dfrac{1}{n}\sum_{i=1}^{n}(P_i - O_i)^2}$	0
%RMSE	Percentage root mean square error	$\%RMSE = \dfrac{RMSE}{\frac{\sum_{i=1}^{n} O_i}{n}} x100$	0%
R^2	Coefficient of determination	$\dfrac{(\sum_{i=1}^{n}(P_i - \bar{P})(O_i - \bar{O}))^2}{\sum_{i=1}^{n}(P_i - \bar{P})^2 . \sum_{i=1}^{n}(O_i - \overline{O)^2}}$	1
WI	Willmont index of agreement	$1 - \dfrac{\sum_{i=1}^{n}(P_i - O_i)^2}{\sum_{i=1}^{n}(|P'_i| + |O'_i|)^2}$	1
CRM	Residual mass coefficient	$\dfrac{(\sum_{i=1}^{n} O_i - \sum_{i=1}^{n} P_i)}{\sum_{i=1}^{n} O_i}$	0

O_i – observed value; P_i – predicted value; $\bar{P}$-mean of the predicted; $\bar{O}$- mean of the observed; $P'_i = P_i - \bar{O}$; $O'_i = O_i - \bar{O}$

Once calibrated using the observed data for 2004 and 2005 seasons, Cropsyst was used to predict yields and water demands under future scenarios. The effects of a climate change on silage maize crop production is expressed as the relative changes in yields between baseline scenario (dry and hot year 2008 WRF simulated data) and future extreme years climate under RCP4.5 (years 2020, 2029, 2040 and 2050) and RCP8.5 (years 2017, 2023, 2035 and 2050).

6.3 Results and Analysis

6.3.1 Calibration and Validation

Predicted (simulated by cropsyst using the observed weather data at AREC) and observed seasonal silage maize grain yields during calibration (2004 and 2005) and

validation (2006 to 2008) showed a good model performance (Fig. 6.3). Predicted versus observed seasonal yield data pairs tended to line up around the 1:1 line that indicates perfect agreement along the range of observed yields. We reiterate that the growing season happens once every year from May to October, thus the seasonal yield is the same value as the yearly yield. Average predicted and observed grain yields for calibration and validation compared well with RMSE values were less than 10% of the observed average. The values of the index of agreement, WI, and the coefficient of determination R^2 were high and the CRM points to a nearly perfect fit (a value of zero means optimal agreement) (Table 6.5).
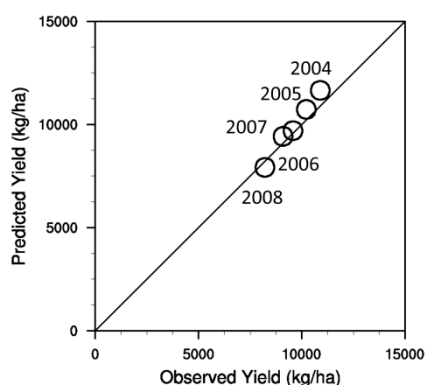
Fig. 6.3. Predicted/observed yearly yield (kg/ha) for calibration (2004-2005) and validation (2006-2008))

Table 6.6. Performance indicators for the calibration and validation of yield

	%RMSE	R^2	WI	CRM
Yield Calibration	3.1%	1.00	0.97	-0.06
Yield Validation	1.9%	0.95	0.96	-0.01

Accordingly, the overall yield simulations were considered satisfactory for all growing seasons The errors in the predictions of biomass growth during the growing season were smaller for 2006 to 2008 (years of validation) than for 2003 and 2004 (years of calibration). Note however that climatic conditions and sowing date vary between cropping seasons. The later sowing in 2008, accompanied by the hottest weather compared to 2004 to 2007, resulted in a sensitive reduction of the cropping cycle duration and, as a consequence, in a lower potential yield value.

6.3.2 Future Simulations without Adaptation

Modifications were introduced to CropSyst to account for the effects of increased atmospheric CO_2 concentration (Meinshausen *et al*., 2011) on plant growth and water use under the eight future simulated years from both RCPs (Table 6.7). Daily WRF outputs for the AREC, calculated from the two hourly outputs, for precipitation, maximum and minimum temperatures, solar radiation, maximum and minimum relative humidity and average wind speed served as input to Climgen which was then used to generate the maximum and minimum dew temperatures. The planting date (~day 149 of the year) and crop management regime (irrigation, fertilization, conservation tillage) were defined to be similar to those adopted in the baseline scenario for year 2008. The yield of 2008 was obtained by running Cropsyst using the weather data from WRF outputs and not from the observed weather data at AREC during 2008. Table 6.8 presents the projected monthly precipitation and temperatures at AREC under both RCP4.5 and 8.5, while Table 6.9 displays the projected silage maize yield and the corresponding water balance components under the same scenarios.

Table 6.7. Equivalent CO_2 concentration adopted in the simulations of WRF and Cropsyst (Source: Meinshausen *et al*., 2011)

RCP	Year	Equivalent CO_2 concentration (ppm)
4.5	2020	423
	2029	454
	2040	493
	2050	526
8.5	2017	417
	2023	443
	2034	510
	2050	628

Table 6.8. Baseline and projected monthly precipitation, maximum and minimum temperatures at AREC for RCP4.5 and 8.5

Year	Jan	Feb	Mar	Apr	May	Jun	Jul	Aug	Sept	Oct	Nov	Dec	Total
Precipitation (mm)													
Baseline													
2008	15.0	24.0	15.0	0.0	6.0	0.0	0.0	1.0	0.0	18.6	25.9	74.3	**179.8**
RCP 4.5													
2020	38.5	2.1	82.7	28.8	64.1	29.3	0.0	0.0	0.2	38.1	82.4	87.6	**453.8**
2029	43.6	69.2	32.2	15.1	27.7	1.1	0.0	0.0	0.0	103.2	2.8	23.2	**318.1**
2040	16.4	30.2	33.2	44.2	19.9	0.5	0.0	0.0	0.0	8.4	3.5	16.9	**173.2**
2050	14.0	12.6	18.9	63.1	5.5	5.9	0.0	2.1	0.1	25.9	43.8	26.5	**218.4**
RCP 8.5													
2017	87.2	29.3	38.9	85.1	31.8	41.6	0.0	0.0	0.0	49.2	117.7	109.5	**590.2**
2023	8.4	60.5	27.2	15.3	45.0	0.0	0.0	0.0	0.0	15.5	66.3	19.9	**258.1**
2035	40.8	45.4	42.0	36.6	21.2	17.4	0.0	0.0	4.4	0.2	42.2	3.2	**253.5**
2050	6.2	44.5	49.3	20.7	31.8	0.0	0.0	0.0	0.3	42.1	94.1	32.9	**321.8**
Tmax (^{0}C)													
Baseline													
2008	12.2	14.4	22.4	25.0	26.7	32.5	34.4	35.3	25.9	22.9	17.5	11.1	**23.4**
RCP 4.5													
2020	10.3	14.4	16.0	20.4	23.9	28.6	33.5	34.3	29.2	22.1	16.1	9.9	**21.6**
2029	7.3	7.3	12.4	20.1	24.3	32.2	34.8	36.5	31.4	22.1	21.1	14.0	**22.0**
2040	6.5	8.5	14.1	21.1	24.1	30.5	35.1	36.5	31.3	24.9	21.2	13.3	**22.3**
2050	10.6	10.9	16.1	21.5	24.2	30.5	33.9	32.5	30.7	22.5	14.7	10.9	**21.6**
RCP 8.5													
2017	9.3	9.6	13.7	20.5	22.6	26.9	33.6	32.5	32.9	25.3	12.8	8.4	**20.7**
2023	9.8	12.6	18.2	22.8	23.8	29.8	33.3	35.0	30.5	23.2	13.9	9.6	**21.9**
2035	7.7	11.6	15.4	21.1	23.0	29.6	36.8	34.3	28.3	25.8	17.7	13.4	**22.1**
2050	13.4	12.7	14.4	23.4	23.3	30.7	34.1	35.5	29.4	25.7	14.1	12.2	**22.4**

144

						Tmin (°C)							
Year	**Jan**	**Feb**	**Mar**	**Apr**	**May**	**Jun**	**Jul**	**Aug**	**Sept**	**Oct**	**Nov**	**Dec**	**Total**
						Baseline							
2008	0.2	0.7	7.0	8.1	8.8	13.7	15.0	17.2	11.5	9.3	3.5	1.7	**8.1**
						RCP 4.5							
2020	2.1	3.8	5.3	7.2	10.7	14.9	17.4	18.5	15.3	11.2	7.3	2.0	**9.6**
2029	-0.8	-0.6	2.2	8.6	12.0	18.1	18.5	19.5	16.0	11.7	10.6	4.3	**10.0**
2040	-0.7	0.0	3.3	9.6	11.2	15.7	18.8	19.4	16.4	12.3	9.8	4.1	**10.0**
2050	0.9	0.7	4.6	8.7	10.4	16.2	18.4	17.0	15.6	11.6	6.6	2.1	**9.4**
						RCP 8.5							
2017	1.6	1.6	2.4	9.2	11.0	13.6	18.6	16.9	17.5	14.1	5.6	1.8	**9.5**
2023	1.1	3.1	7.0	10.4	11.5	15.3	17.4	18.9	14.7	11.9	5.4	1.2	**9.8**
2035	0.2	2.2	4.4	10.0	9.9	16.1	19.9	19.2	14.4	12.2	8.2	3.2	**10.0**
2050	3.1	3.0	3.2	10.8	10.7	16.7	18.8	20.1	15.1	14.4	5.4	3.1	**10.4**

Table 6.9. Baseline (2008) and projected crop yield and water balance
under RCP4.5 and RCP8.5

	RCP4.5										
	Predicted Yield (kg/ha)			**Water Balance (mm)***							
			%								
Year	**Yield**	**Yr 2008**	**Difference**	**P**	**Ir**	**In**	**R**	**E**	**T**	**D**	**WB**
2020	7423	8142	-8.8%	41	485	0	3	218	469	0	-166
2029	5297	8142	-34.9%	1	485	1	0	207	387	0	-108
2040	5253	8142	-35.5%	1	485	0	0	206	353	0	-73
2050	7149	8142	-12.2%	15	485	0	0	197	431	0	-129
	RCP8.5										
2017	7869	8142	-3.3%	43	485	0	9	204	500	0	-185
2023	5321	8142	-34.6%	0	485	0	0	211	351	0	-76
2035	5547	8142	-31.9%	18	485	0	0	221	380	0	-98
2050	7187	8142	-11.7%	15	485	0	0	194	420	0	-115

*P=Precipitation, Ir=Irrigation, In=Interception, R=Runoff, E=Evaporation, T=Transpiration, D=Drainage,
WB=Water Balance

While the predicted cycle in the simulated extreme years of RCP4.5

precipitation is characterized by considerable yearly variability, there is an indication of

a decrease in yearly precipitation, especially in 2040, which is the worst case scenario of

RCP4.5 based on the anomaly score, compared to average yearly precipitation in 2008

at AREC. Note that year 2008 was also a dry year and the predicted precipitation of all four years in RCP4.5 was still lower than 512 mm average yearly precipitation at AREC (Table 6.1). For Tmax, the predicted values show warmer summer and fall seasons and colder winter and spring seasons in comparison to year 2008. As for Tmin, warmer temperatures occur in all seasons except winter, where the minimum temperatures are expected to decrease compared to 2008. It is worthwhile to mention that the difference in average yearly temperature between past and future simulated years was minimal (Chapter 4), while the major difference in maximum and minimum temperature extremes was significant.

Note also that prior to simulating maize yield by Cropsyst, WRF control run for 2008 was checked for its biases in representing the seasonality of precipitation and temperature for the period 2000-2010 (Chapter 4). Compared to observational data, the WRF control run represents the seasonal cycles of mean precipitation and temperature reasonably well with no large biases. Hence, no bias correction was introduced which offers the advantage that the disruption of the physical consistency between the different variables (precipitation and temperature) is avoided (Waongo *et al.*, 2015).

Knowing when and how climate change will impact crop production is essential for devising adaptation strategies. Under RCP4.5 conditions, and without any adaptation measures, the negative effects on crop yields of warmer temperatures and decreased precipitation were stronger than the positive effects of elevated CO_2 in simulated years. Under the same management practices used in 2008 (date of planting, irrigation, fertilization, tillage, etc.), silage maize yields at AREC is expected to decrease by 8.8% to 35.5%, depending on the year and governing weather conditions, with year 2040 resulting in the highest decrease in yield (Table 6.9). Moreover, the

temperature increase during the growing period in 2040, the year presenting the highest decrease in yield in RCP4.5, had a direct effect over crop phenology, whereby the crop growth period, from sowing to crop maturity, exhibited a reduction due to warmer temperatures. Earlier crop flowering and maturity accompanied with a shorter grain filling period reduced the potential yield and silage maize maturity was reached 19 days earlier in 2029 compared to baseline scenario (year 2008).

Diminishing future maize yields, of 3.3% to 34.6%, were also projected under RCP8.5 accompanied with a negative soil water balance (Table 6.9) in comparison with the irrigation amount and schedule of 2008 presented in Table 6.3. In the extreme years in RCP8.5, negative effects caused by changes in climatic conditions overcome the positive effect of biomass increase, and as a consequence, a decrease in crop productivity due to stress by temperature or water is induced. During the early stages of the planting dates of this period, there was generally frequent rain. But there were also high air temperatures and increased solar irradiances particularly during the grain filling stage, which resulted in increased evapotranspiration, and increased crop water and temperature stress indices. All these contributing factors could have been the reasons for the low yield. In addition, the high air temperatures could have the effect of reducing the time for grain filling, and hence reduced yield.

Regarding water balance under both RCPs, a water deficit is expected in the future simulated extreme years from RCP4.5 and RCP8.5, in comparison with the irrigation amount and schedule of 2008 presented in Table 6.3. This is probably due to the higher evapotranspiration demands occurring during those years (Table 6.9).

6.3.3   *Future Simulations with Adaptation*

Adaptation in agriculture means finding the best strategy that will cancel out the negative impacts of climate change with respect to decrease in yield in a given environment. It can be either (1) adapting the environment to suit the plant, or (2) adapting the plant to suit the environment. The environment includes all conditions to which the plant is subjected to during the growing season (from pre-seedling emergence to harvest and maturity). Strategies to adapt to climate change concentrate on the greatest impact of increased temperatures and reduced precipitation with corresponding effect on lowering crop yields. In this study, we did not seek to maximize yields under the future scenarios, but rather to examine the effects of simple adaptation strategies, commonly available to the farmer today. Among the strategies used for adapting the environment to suit the plant is better matching the planting date to the new environmental conditions. For a given region, the growing season is determined by the 'earliest' sowing date and the 'latest' harvest date. The earliest sowing date depends strictly on soil temperature and the probability of frost events during the early stages of the maize crop. The latest harvest date depends on the forage plan (which crop is planned to be sown after the maize) and the risk (probability) of not harvesting due to climatic reasons (e.g. excess rainfall in early autumn). For instance, early planting of spring crops helps avoid plant drought and heat stress during the warmer and drier summer months predicted under climate change. This strategy is recommended in previous studies (Lobel and Field, 2007; Abraha and Savage, 2008; Laux *et al*., 2010; Boggia *et al*., 2013; Waongo *et al*., 2015), however there is the problem of the farmer's knowing in advance that he needs to shift the planting date early during the year in order to cope with a more variable pattern of weather. In this context comes the importance of

seasonal forecasting, which is the attempt to provide useful information about the "climate" that can be expected **in the coming months** (Stockdale, 1997; Stockdale *et al.*, 1998; Segschneider *et al.*, 2001; Vitart and Stockdale, 2001; Alves *et at.*, 2004; Vialard e*t al.*, 2005; Stockdale *et al.*, 2011). The seasonal forecast is not a weather forecast: weather can be considered as a snapshot of continually changing atmospheric conditions, whereas climate is better considered as the statistical summary of the weather events occurring in a given season. Access to weather forecasting can improve farmers' ability to cope with increased variability and extreme events provided the information can be disseminated in time to those who need it. The near ubiquitous reach of mobile phones and related technology in even the poorest countries offers novel means of providing information and advice to food producers and in particular smallholders. Using the hypothesis that the seasonal forecasting predicted that our simulated future years are extremely dry and hot, as was obtained from our anomaly score tests (Chapter 4), planting of silage maize was shifted backwards by 3 (day 128), 4 (day 121) weeks with respect to the baseline year. Moreover, a third costumed planting date was selected based on the daily climate obtained from WRF simulations which corresponds to having no frost temperature and average temperature over $10^{\mathbf{o}}$C, which is the cutoff temperature for Maize (Table 6.4). The resulting planting dates are: Day 115 of Year 2020 (DOY), Day 98 of Year 2029, Day 98 of year 2040, and Day 107 of Year 2050 for RCP4.5. For RCP8.5 the DOY are: Day 110 of Year 2017, Day 86 of Year 2023, Day 95 of Year 2035, and Day 102 of Year 2050. These choices roughly corresponded to having similar air temperatures at planting for both the climate change and the baseline simulations (Tubiello *et al.*, 2000). The resulting yields are presented in Fig. 6.4 while the water balance is presented in Table 6.10 for both RCP4.5 and 8.5.
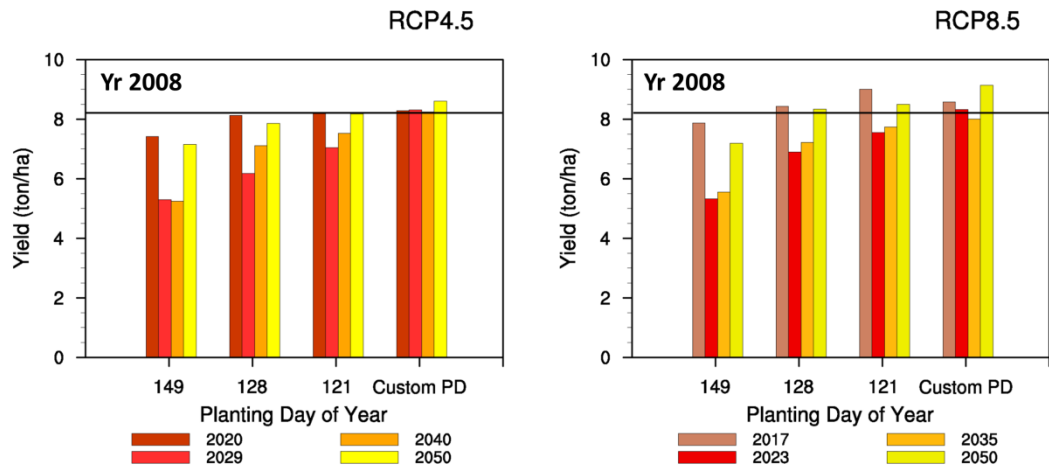
Fig. 6.4. Predicted yield (ton/ha) under different planting dates in RCP 4.5 and RCP8.5

Table 6.10. Water balance components (mm) under different planting dates in RCP 4.5 and RCP8.5

RCP 4.5												
	Planting day of year 128				Planting day of year 121				Customized planting day			
Component	2020	2029	2040	2050	2020	2029	2040	2050	2020	2029	2040	2050
Precipitation	88	15	20	11	93	25	20	11	97	44	32	18
Irrigation	485	485	485	485	485	485	485	485	485	485	485	485
Interception	0	1	1	2	2	1	1	2	1	2	2	3
Runoff	15	0	0	0	15	0	0	0	14	0	0	0
Evaporation	199	216	198	188	199	215	192	183	199	216	204	179
Transpiration	518	412	428	469	516	443	449	483	504	486	483	489
Drainage	0	0	0	0	0	0	0	0	0	0	0	0
Balance	**-159**	**-129**	**-122**	**-136**	**-153**	**-149**	**-135**	**-172**	**-137**	**-175**	**-172**	**-168**
RCP 8.5												
Component	2017	2023	2035	2050	2017	2023	2035	2050	2017	2023	2035	2050
Precipitation	70	35	31	23	73	45	39	32	128	70	75	47
Irrigation	485	485	485	485	485	485	485	485	485	485	485	485
Interception	2	0	2	0	4	0	3	0	5	5	5	2
Runoff	6	1	1	2	3	3	1	2	21	4	3	0
Evaporation	202	223	206	186	191	208	204	179	204	195	189	183
Transpiration	521	416	444	479	546	459	477	490	517	503	484	504
Drainage	0	0	0	0	0	0	0	0	0	0	0	0
Balance	**-178**	**-120**	**-137**	**-159**	**-186**	**-141**	**-161**	**-156**	**-133**	**-152**	**-120**	**-158**

Advancing the planting date by three weeks (i.e. sowing day of year 128 instead of 149) while keeping the same irrigation scheme of 485 mm per season (Table 6.3), resulted in an increase in yield for all the years in both RCPs, however only the yield in 2017 and 2050 under RCP8.5 have exceeded the baseline yield of 2008. The increment in crop yield in these years was accompanied by a soil water storage deficit (Table 6.10) indicating that we will be operating under deficit irrigation, same situation encountered while keeping the planting date to 149 (Table 6.9). The increase in the yield was also more pronounced under RCP8.5 than under RCP4.5, which can be attributed to the higher increase in CO_2 and evapotranspiration under RCP8.5.

Keeping the same irrigation schedule and amount as specified in Table 6.3 and fixing the planting date on day 121 instead of 149 of the year during RCP4.5 resulted in an increase in yield during 2020 (0.7%) and 2050 (0.5%) over the baseline yield of 2008, but the yields of 2029 and 2040 are still below that of 2008 by 13.4% and 7.6% respectively (Fig. 6.4). The same trend is observed in RCP8.5, where yield increased by 10.6% in 2017 and 4.5% in 2050 over the baseline yield of 2008 under the same irrigation and planting date, with the yields of 2023 and 2035 under that of 2008 by 7.2% and 4.9%. These yields are obtained under deficit irrigation for both RCPs as shown in Table 6.9.

Selecting the custom planting date based on the daily temperature as obtained from WRF simulations can eliminate the future decrease in yield with respect to baseline yield of 2008 during both RCPs except year 2035 in RCP8.5 which still shows a decrease of 1.6% less than 2008. Higher yields than baseline scenario of 2008 can be expected (on average 2.7% in RCP4.5 and 4.6% in RCP8.5), but unfortunately under deficient irrigation. This increase in yield can be caused by the fact that setting the

planting date earlier in the season resulted in the situation that the seedbed must have been wet enough for sowing and the water requirements for germination and emergence were met from the precipitation and irrigation occurring early in the cropping season. Prolonged dry spells were avoided during the first stage of crop development where maize is more vulnerable to water stress then. This criterion is particularly important for water-limited regions and for crops with reduced water stress resistance such as maize (Laux *et al*., 2008).

A second effective adaptation option for silage maize used for adapting the environment to suit the plant is increasing irrigation water so that yield improvement could occur under climate change conditions as reported in the literature (Döll, 2002; El Afandi *et at*., 2010; Laux *et al*., 2010; *Ouda et al*., 2015). This adaptation technique is not viable in water stressed regions, such as AREC, where the decrease in future precipitation shown in Table 6.8 will result in reduced water availability for irrigation.

Previous research indicate that, in principle, climate change impacts on silage maize can be reduced through adopting higher-yielding and heat resistant cultivars or sowing other plants that uses less water such as Sorghum (Tubiello *et al*., 2000; Tingem *et al*., 2009a & b; Díaz-Ambrona *et al*., 2013).

6.4   Conclusion

Based on high resolution (3 km) regional climate change scenarios from WRF model forced by lower resolution HiRAM (25 km) silage maize (*Zea Mays* var Oropesa) yield in a semi-arid region was simulated using the process-based Cropsyst model, and potential mitigation strategies were investigated. CropSyst model was calibrated using the soil characteristics of an experimental site, weather data of the growing seasons, and

crop data including planting and harvest dates, the date of phenological stages, and biomass yields of years 2004 and 2005. Validation runs were conducted for years 2006 to 2008 using the calibrated model. The simulated future climates focused on eight extreme hot and dry years under RCP4.5 (years 2020, 2029, 2040 and 2050) and RCP8.5 (years 2017. 2023, 2035 and 2050) scenarios that were compared to a past dry and hot year (2008) to examine the possible changes in silage maize agricultural production. Early sowing was tested and corresponding water balance components were characterized.

The results showed that CropSyst predicted crop yields and potential evapotranspiration well, with low values of RMSE and CRM, and high value of WI and R2 for both calibration and validation. Without adaptation measures, a significant decrease in crop yields in seven out of eight simulated years reached up to 23% in some particular years in comparison with the baseline yield of 2008. Selecting a sowing date based on seasonal forecasting appeared to be the most viable option to adapt to changing climates.

While CropSyst was able to simulate reasonably well the silage maize cropping system, the development of a comprehensive field database is desirable for further evaluation and improvement of the model for regional conditions. The crop parameters can be considered as an initial adaptation of the model to this particular environment and may be improved with future data. It is worth pointing out that this study does not take into account changes in the agricultural policy or the regional and global markets, which eventually are expected to decrease the negative effects of climate change. As such, the analysis provides only worst limits for what could take place as a result of climate change in a semi-arid region.

CHAPTER 7

CONCLUSION

7.1   Major Conclusions

The goal of this dissertation was to develop a methodology for downscaling the impacts of climate change on the agricultural yield and water resources over the complex terrain of Lebanon. High resolution dynamical downscaling was adopted and applied along the eastern Mediterrean basin using. The regional climate models used for downscaling was the Weather Research and Forecasting (WRF) forced by High Resolution Atmospheric Model (HiRAM), a global model. Simulations were conducted for the past under business as usual scenario and for the future (2011-2050) under RCP 4.5 and 8.5 scenarios. The output of the downscaling was then used to force a agricultural yield model (CropSyst) and assess the impact of climate change on agricultural production.

Prior to conducting these future simulations, WRF model was driven with initial and boundary condition from GFS-reanalysis (resolution 1°) for the years 2003 (a mild and wet year) and 2010 (a hot and dry year) and nested at sequential horizontal resolutions of 9, 3 and 1 km to examine its skill as a tool for climatological downscaling and its capability to capture the climatology of extreme events. Simulated near-surface hydrometeorological variables were compared at different time scales against data from an observational network over the study area comprising rain gauges, anemometers, and temperature measurements with records of daily average and/or daily maximum and minimum temperatures. The yearly precipitation from WRF's 1km and 3km domains

exhibited less than 10% bias with respect to observational data. The errors in minimum and maximum temperatures were reduced by the downscaling, along with a high-quality delineation of temperature variability and extremes for both the 1 and 3 km resolution runs. Wind speeds, on the other hand, are generally overestimated for all model resolutions, in comparison with observational data, particularly on the coast (up to 50%) compared to inland stations (up to 40%). The errors in various extreme indices (such as minimum and maximum temperatures, number of hot or frost days, and rainfall intensity) were reduced by the downscaling, marking a large improvement over GFS Reanalysis data in the description of temperature variability and extremes. Results indicated that a 3km resolution is sufficient for the downscaling, and they compared well with recent studies with other models and/or for other regions, further supporting the benefits of dynamic downscaling over complex terrain, and establishing the skill of WRF for such downscaling.

Then, a set of ten downscaling simulations at high spatial resolution (3 km horizontally) were performed using the Weather Research and Forecasting (WRF) driven with HiRAM(25 km resolution), under the conditions of two Representative Concentration Pathways (RCP) (4.5 and 8.5). Each downscaling simulation spanned one year. We simulated recent past extreme wet and dry years (2003 and 2008) as a baseline for comparison, and one future (2011–2050) extreme year per decade for each scenario: 2020, 2029, 2040 and 2050 from RCP4.5 and 2017, 2023, 2035 and 2050 from RCP8.5. Eight future years were then selected based on an anomaly score that relies on the mean annual temperature and accumulated precipitation to identify the worst year per decade from a water resources perspective. The downscaled data were in the range of recent observed climatic variability, and therefore corrected for the cold bias of HiRAM. All

WRF simulations projected a warming over the study region with different intensities depending on the year and/or RCP under consideration, with the worst case scenario occurring in the central inland and the mountainous regions. Climate indices derived from daily simulated temperature data show significant changes in daily maximum summer and minimum winter temperature extremes. The downscaling simulations provided evidence of a significantly drier climate over the whole study area by the mid of this century, with reduction in annual precipitation of about 30%. The projections show that this significant decrease in precipitation spans all geo-climatic regions and both RCPs. The mountainous areas, as well as the inland regions, will be particularly affected by these precipitation decreases (particularly in terms of snowfall), while the impacts in the coastal regions are slightly lower. The topographical complexity resulted in significant regional differences, with the most severely affected regions experiencing more than a doubling of extreme indices.

Finally, the potential impacts of climate change on silage maize (*Zea Mays* var Oropesa) production were examined at a pilot area (AREC) located in the semi-arid central inland region of Lebanon using Cropsyst model and WRF past and future simulations outputs. The results showed that CropSyst predicted crop yields and potential evapotranspiration well, with low values of Root Mean Square Error (RMSE and Residual Mass Coefficient (CRM), and high value of Willmont Index (WI) and Coefficient of Determination (R2) for both calibration and validation. Without adaptation measures, a significant decrease in crop yields in seven out of eight simulated years reached up to 23% in some particular years in comparison with the baseline yield of 2008. Selecting an earlier sowing date using seasonal forecasting appeared to be the most viable option to adapt to changing climates. As a result, yield

improvement was on the average 3% in RCP4.5 and 5% in RCP8.5 in comparison with 2008 baseline scenario.

7.2   Study Limitations and Recommendations for Future Work

The main limitations of this study are the following. First, only one set of GCM output has been used in this work. Given the uncertainties associated with GCM projections over complex terrain, ensembles of GCM simulations would give more insights on the panel of potential variations regarding climate change signals. Moreover, the selection of the critical years was based on an anomaly score related to annual precipitation and yearly median temperature. A different selection can be based on either temperature or precipitation, or running climate simulations for two different years per decade, the hottest and the driest years. Furthermore, the results presented here refer to climate trends between 2011–2050, from which trends for the remainder of the 21st century cannot be inferred. The short term period (till 2050) is preferred for the selection of the adaption measures but the higher increase for greenhouse gases is expected to be more prominent after the mid of the twenty first century (IPCC, 2013).

Finally, while CropSyst was able to simulate reasonably well the silage maize cropping system, the development of a comprehensive field database is desirable for further evaluation and improvement of the model for regional conditions. The crop parameters can be considered as an initial adaptation of the model to this particular environment and may be improved with future data.Moreover, this study provides a template for one particular crop, future work on other important crops in the study area (Lebanon) can be conducted using the procedure detailed in this work. This template can be also used to investigate crops that tolerate both drought and heat stresses, such as

157

Sorghum and Millet. The investigation can include the effect of hail and other extremes on agricultural yield, using WRF simulated hail predictions for the future. Finally, the impacts of climate change on the agricultural yield in the study area (Lebanon) can be compared with the same impact in surrounding countries, to correlate how climate change might affect the eastern meditteranean region from a food security perspective, especially with countries that are relied upon for exporting and importing agricultural goods.

APPENDIX A

Summary of recent WRF studies

Reference	Location	Driving GCM	Domain Resolution	Climate Variable Simulated	Time Slice Covered
Argüeso et al., 2011 & 2012	Spain	ERA40 reanalysis[4] , ECHAM5[1] & CCSM3.0[2]	30:10 km	Temperature & precipitation	1990-1999 1970–1999 2070–2099
Berg et al., 2013	Germany	ECHAM5[1], CCCma3[3] & ERA40 reanalysis[4]	50:7 km	Temperature & precipitation	1971-2000
Boulard et al., 2013	Southern Africa & South West Indian Ocean	ERA40 reanalysis[4] & ERA-Interim[7]	35 km	El Ninõ Southern Oscillation (ENSO) climate variability	1971-1998
Bowden et al., 2013	Eastern United States	NCEP AMIP-II reanalysis[5]	108:36 km	Temperature & precipitation	1988-2007
Bukovsky & Karoly, 2009	Eastern United States	NCEP-NCAR global reanalysis[6]	90:30 km	Precipitation	Apr 23 -Aug 31 (1991-1995)
Caldwell et al., 2009	California	CCSM3.0[2]	36:12 km	Precipitation, temperature & snowpack	1948-2008
Cardoso et al., 2012	Iberian peninsula	ERA-Interim[7]	27:9 km	Precipitation	1989-2009
Flaounas et al.,2013	Mediterranean basin	ERA-Interim[7]	50:20 km	Temperature & precipitation	1989-2008
Flaounas et al., 2013	Mediterranean basin	ERA-Interim[7] & IPSL-CM5[8]	50 km	Cyclones	1989-2005
Gao et al., 2012	Eastern United States	CESM1.0[9]	36:12:4 km	Temperature & precipitation	2001-2004 & 2057-2059
Givati et al., 2012	Jordan River	NCEP-GFS[10] analysis	36:12:4:1.3 km	Temperature & precipitation	Winter 2008-2010
Heikkilä et al., 2011	Norway	ERA40-reanalysis[4]	30:10 km	Temperature & precipitation	1961-1990
Li et al., 2013	Baltimore-Washington	NARR[11]	9:3:1 km	Temperature, wind, humidity & precipitation	21-29 Jul. 2008
Lo et al., 2008	United States	NCEP-FNL[10] Reanalysis	36 km	Pressure, temperature, wind, & precipitation	2000
Paimazumder et al., 2012	Siberia	NCEP/NCAR reanalysis[6]	50 km	Precipitation, temperature, wind & snow depth	Jul. & Dec. 2005
Pan et al., 2011	California & Nevada	NCEP-GFS[10] reanalysis & PCM[12]	36:12:4 km	Temperature & precipitation	2006-2006 1997-2006 2047-2056
Qian et al., 2010	Western United States	NCAR CAM313	15 km	Precipitation, temperature, snowpack & runoff	1993-2003 2039-2049

Reference	Location	Driving GCM	Domain Resolution	Climate Variable Simulated	Time Slice Covered
Rostkier-Edelstein *et al.*, 2014	Israel	CFS[19]	54:18:6:2 km	Temperature & precipitation	7 wet seasons 1991 to 2009
Ruby Leug & Qian, 2009	Western United States	NCEP AMIP-II reanalysis[5]	50 km	Temperature & precipitation	1980-1999
Soares *et al.*, 2012	Portugal	ERA-Interim[7]	27:9 km	Temperature & precipitation	1989-2008
Talbot *et al.*, 2012	Eastern United States	NARR[11] & GEWEX-GCIP[16]	12.15:4.05:1.35:0.45:0.15:0.05 km	Wind, humidity & temperature	24 Sept. 2007
Tursilowati *et al.*, 2012	Jakarta, Indonesia	NCEP-FNL[10] Reanalysis	27:9:3:1 km	Surface air temperature & urban heat island	2-4 Feb. 2008
Vigaud *et al.*, 2011	West Africa	ARPEGE-CLIMAT[14] & ERA40-reanalysis[4]	50 km	Temperature & precipitation	1981-1990 2032-2041
Wagner *et al.*, 2013	Germany	ECHAM5[1], & CCCma3[3]	50:7 km	Temperature & precipitation	1971-2000 2021-2050
Warrach-Sagi *et al.*, 2013	Germany	ERA-Interim[7]	36:12:4 km	Precipitation	1989-2008
White & Toumi, 2012	South Africa	ERA40-reanalysis[4] & CCSM3.0[2]	36:12 km	Precipitation, runoff, & evapotranspiration	1979-1989 2039-2059
Wi *et al.*, 2012	Colorado	HadCM3[15]	35 km	Temperature, precipitation & snowfall	1969-2079
Xu & Powell, 2012	Central & Southwest Asia	NCEP-GFS[10]	15 km	Precipitation & radiance	1-31 Jan. 2007
Yang *et al.*, 2012	Eastern China	NCEP-FNL[10] Reanalysis	25:5:1 km	Temperature, precipitation & humidity	2000-2009
Yeung *et al.*, 2011	Northern United States	NCEP Eta model analysis[17]	9:3 km	Rainfall climatology	2003-2007
Zhang *et al.*, 2009	U.S Pacific Northwest	NCEP AMIP-II reanalysis[5]	108:36:12 km	Temperature & precipitation	2003-2007
Zhang *et al.*, 2012	Western United States	ECHAM5[1] & CCSM3.0[2]	108:36 km 20 km	ENSO climate variability	1970-1999 2030-2059
Zhao *et al.*, 2009b	Western China	Chinese T213L31 model[18]	1 km	Snowmelt runoff	19 Feb.-6 Mar. 2008

[1] Max Planck Institute ECHAM5 (http://www.mpimet.mpg.de/en/wissenschaft/modelle/echam/echam5.html)

[2] NCAR Community Climate System Model (CCSM3.0) (http://www.cesm.ucar.edu/models/ccsm3.0/)

[3] Canadian Centre for Climate Modelling and Analysis (CCCma3) (http://www.cccma.ec.gc.ca/)

[4.] European Centre for Medium-Range Weather Forecasts (ECMWF) 40 Year Reanalysis (ERA-40) Data Archive (http://www.ecmwf.int/products/data/archive/descriptions/e4/)

[5] NCEP–Department of Energy Atmospheric Model Intercomparison Project reanalysis (http://www.cpc.ncep.noaa.gov/products/wesley/reanalysis2/)

[6] NCEP/NCAR Reanalysis Project (NNRP) (http://rda.ucar.edu/datasets/ds090.0/)

[7.] European Centre for Medium-Range Weather Forecasts Interim Reanalysis Data Archive (ERA) (http://www.ecmwf.int/research/era/do/get/era-interim)

[8] Institut Pierre Simon Laplace Climate Model (http://icmc.ipsl.fr/index.php/icmc-models/icmc-ipsl-cm5)

[9] NCAR Community Earth System Model (CESM1.0) (http://www.cesm.ucar.edu/models/cesm1.0/)

[10] NCEP Global Forecast System Final (FNL) Analyses data (http://rda.ucar.edu/datasets/ds083.2/)

[11] North American Regional Reanalysis (NARR) (http://www.ncl.ucar.edu/Applications/narr.shtml)

[12] Parallel Climate Model (PCM) (http://www.cgd.ucar.edu/pcm/)

[13] NCAR CCSM3.0 COMMUNITY ATMOSPHERE MODEL (CAM) (http://www.cesm.ucar.edu/models/atm-cam/)

[14] ARPEGE-CLIMAT (http://www.cnrm.meteo.fr/gmgec/arpege/arpege.html)

[15] Hadley Centre for Climate Prediction and Research/Met Office (HadCM3) (http://www.metoffice.gov.uk/research/modelling-systems/unified-model/climate-models/hadcm3)

[16] Global Energy and Water Cycle Experiment (GEWEX) Continental-Scale International Project (GCIP) (http://data.eol.ucar.edu/codiac/ds_proj?GCIP%2fGIDS-1)

[17] NCEP Eta model analysis fields (http://rda.ucar.edu/datasets/ds609.2/)

[18] Chinese fourth-generation medium-term global numerical weather prediction systems T213L31

[19] Climate Forecast System (CFS) (http://www.ncdc.noaa.gov/data-access/model-data/model-datasets/climate-forecast-system-reanalysis-and-reforecast-cfsrr)

APPENDIX B

Available stations for observation data
(temperature and precipitation)

Region / Station Name	Longitude	Latitude	Elevation (m)	Source	Temperature	Precipitation
Northern Coast						
Balamand	35.78	34.37	359	LNMS	NA	2010 (M)
El Abde	35.99	34.52	37	LNMS	not used	2003 (D) & 2010 (M)
El Qlaiat-Akkar	36.01	34.59	5	LNMS	NA	2010 (M)
El Qoubayat	36.28	34.57	497	LNMS	NA	2010 (M)
Kafar Chakhna	35.87	34.35	260	LNMS	2003 (D)	2003 (D) & 2010 (M)
Tripoli - IPCC	35.88	34.45	5	LNMS & NCDC	2003 & 2010 (D)	2003 & 2010 (D)
Central Coast						
Baakline	35.57	33.68	885	LARI	NA	2010 (M)
Beirut International Airport	35.48	33.82	12	LNMS & NCDC	2003 & 2010 (D)	2003 & 2010 (D)
Beyrouth-Golf	35.49	33.85	14	LNMS	NA	2010 (M)
Deir El Kamar	35.56	33.70	794	LNMS	NA	2010 (M)
El Meshref	35.48	33.71	395	LNMS	2003 (D)	2003 (D) & 2010 (M)
El Qoussaibah	35.65	33.87	584	LNMS	NA	2010 (M)
Fanar	35.55	33.88	90	LARI	NA	2010 (M)
Hemleya	35.71	33.94	805	LNMS	NA	2010 (M)
Lebaa	35.45	33.54	331	LNMS	2003 (D)	2010 (M)
Saida	35.38	33.55	31	LARI	2010 (D)	not used
Southern Coast						
Derdghaya	35.38	33.27	388	LARI	2010 (D)	2010 (D)
El Quasmiye	35.26	33.33	9	LNMS	2003 (D)	2010 (M)
Markaba	35.53	33.24	520	LARI	2010 (D)	2010 (D)
Tyr	35.22	33.26	4	LNMS & LARI	2010 (D)	2003 & 2010 (D)
Northern Mountain						
Ehden	35.97	34.30	1480	LARI	2010 (D)	2010 (D)
Fneidek	36.18	34.49	1212	LARI	2010 (D)	not used
Syr-Ed-Denniye	36.03	34.38	926	LNMS	2003 (D)	2003 (D)
Central Mountain						
Aamatour	35.60	33.63	702	LARI	NA	2010 (M)
Ain Al Abou	35.78	34.01	1200	LARI	2010 (D)	not used
Al Akoura	35.89-	34.12	1461	LARI	2010 (D)	2010 (D)
Barouk Fraidis	35.68	33.71	1114	LNMS	2003 (D)	not used
Bayssour	35.56	33.76	940	LNMS	not used	2003 (D) & 2010 (M)
Dahr El Baidar	35.77	33.81	1516	LNMS	2003 (D)	2003 (D) & 2010 (M)
Faqra	35.81	33.99	1655	LNMS	2003 & 2010 (D)	not used
Jezzin	35.57	33.54	1070	LNMS	NA	2010 (M)
Qartaba	35.85	34.10	1222	LNMS	NA	2010 (M)
Tarchich	35.82	33.88	1622	LARI	2010 (D)	2010 (D)

Region / Station Name	Longitude	Latitude	Elevation (m)	Source	Temperature	Precipitation
Northern Inland						
Deir El Ahmar	36.13	34.12	943	LNMS	2003 (D)	2003 (D) & 2010 (M)
El Hermel	36.41	34.40	605	LNMS	NA	2010 (M)
El Qaa	36.51	34.39	583	LARI	2010 (D)	2010 (D)
Mansoura-Hermel	36.41	34.42	682	LARI	2010 (D)	2010 (D)
Central Inland						
AREC	36.08	33.93	994	AUB	2003 (D)	2003 (D)
El Qaraoun	35.68	33.55	843	LNMS	2003 (D)	2010 (M)
Haouch Al Oumara	35.90	33.84	926	LNMS & NCDC	2003 & 2010 (D)	2003 & 2010 (D)
Kfardan	36.06	34.02	1049	LARI	NA	2003 & 2010 (D)
Khorbet Kanafar	35.72	33.64	1005	LARI	2010 (D)	2010 (D)
Talia	36.15	33.92	1185	LARI	NA	2010 (M)
Tel Amara	35.99	33.86	915	LARI	2010 (D)	2003 & 2010 (D)
Terbol	35.99	33.81	905	LARI	2010 (D)	2010 (D)
Southern Inland						
Kafar qouq/Rachaya	35.89	33.54	1205	LNMS	2003 (D)	2003 (D) & 2010 (M)
Marjeyoun	35.58	33.36	827	LNMS	NA	2010 (M)
Mimes	35.70	33.44	820	LARI	2010 (D)	not used
Rachaya El Fakhar	35.66	33.36	797	LARI	2010 (D)	2010 (D)

Where: NA= not available, D = daily data, M = monthly data

APPENDIX C

Annual precipitation distribution in Lebanon
(Source: MOA/UNDP/GTZ, 2003)

APPENDIX D

Probability density of averaged daily precipitation
2003 and 2010
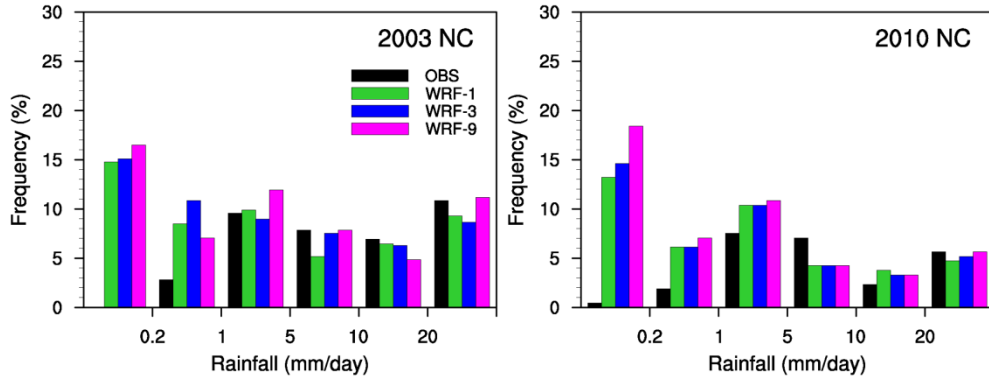
a.   Northern coastal regions
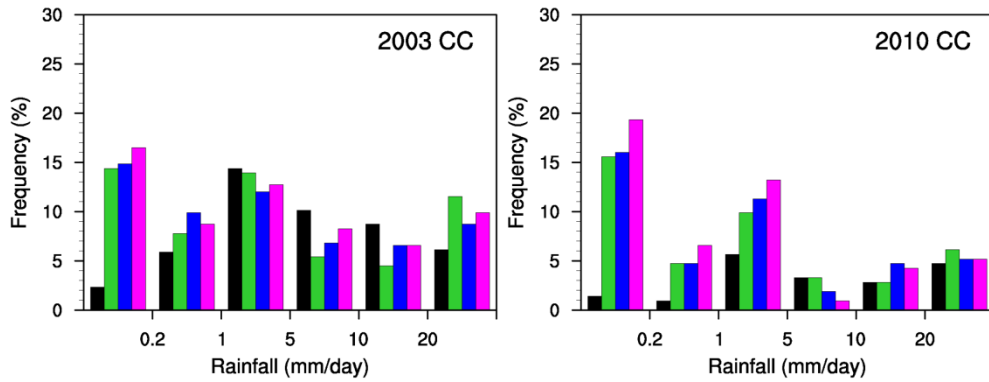
b. Central coastal regions
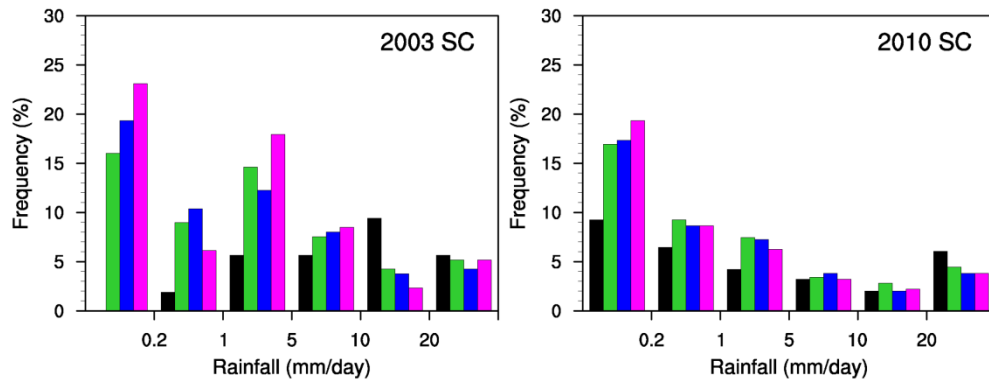
c. Southern coastal regions
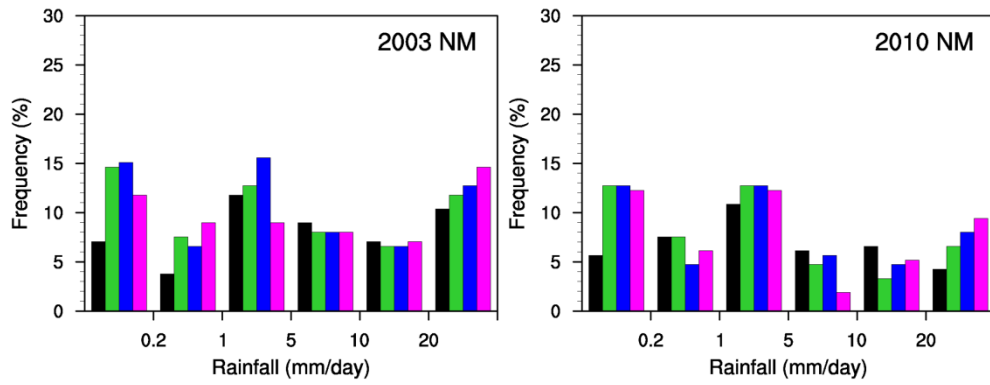
d. Northern mountainous regions
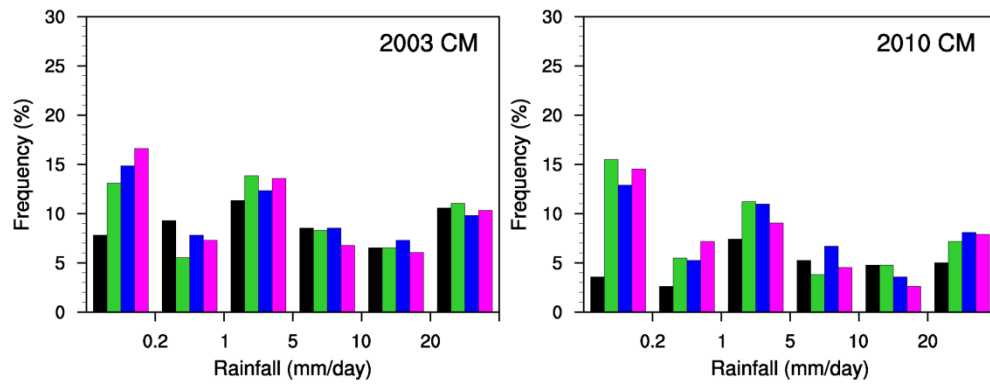
e. Central mountainous regions
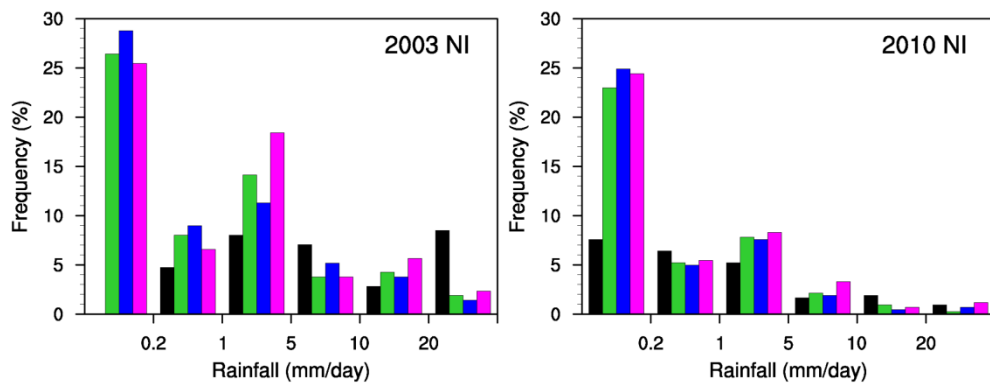
f. Northern inland regions
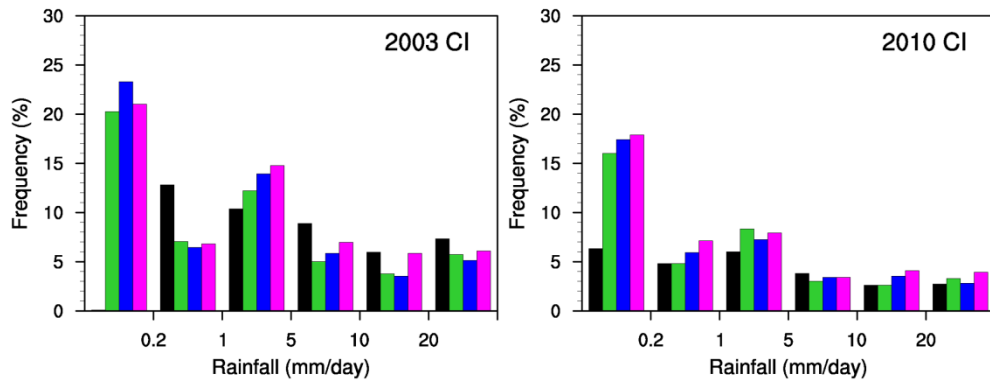
g. Central inland regions
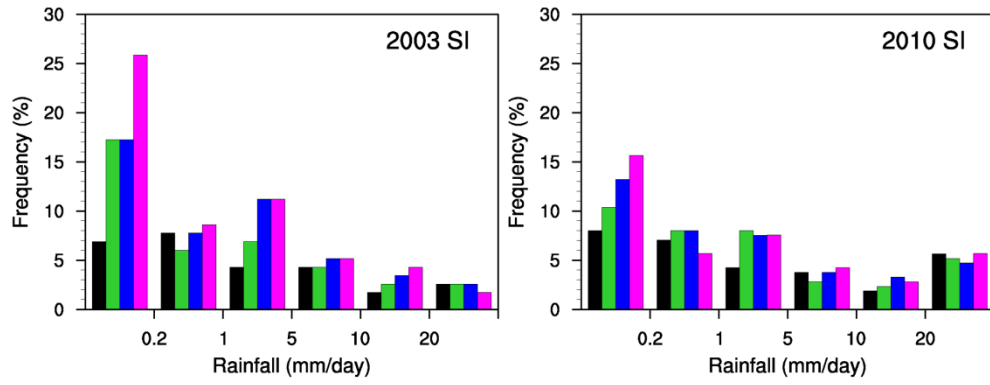
h. Southern inland regions

APPENDIX E

Wind roses for available stations for 2003

APPENDIX F

Wind speed seasonal pdf of coastal (TRP) and inland (HAO) stations for 2010
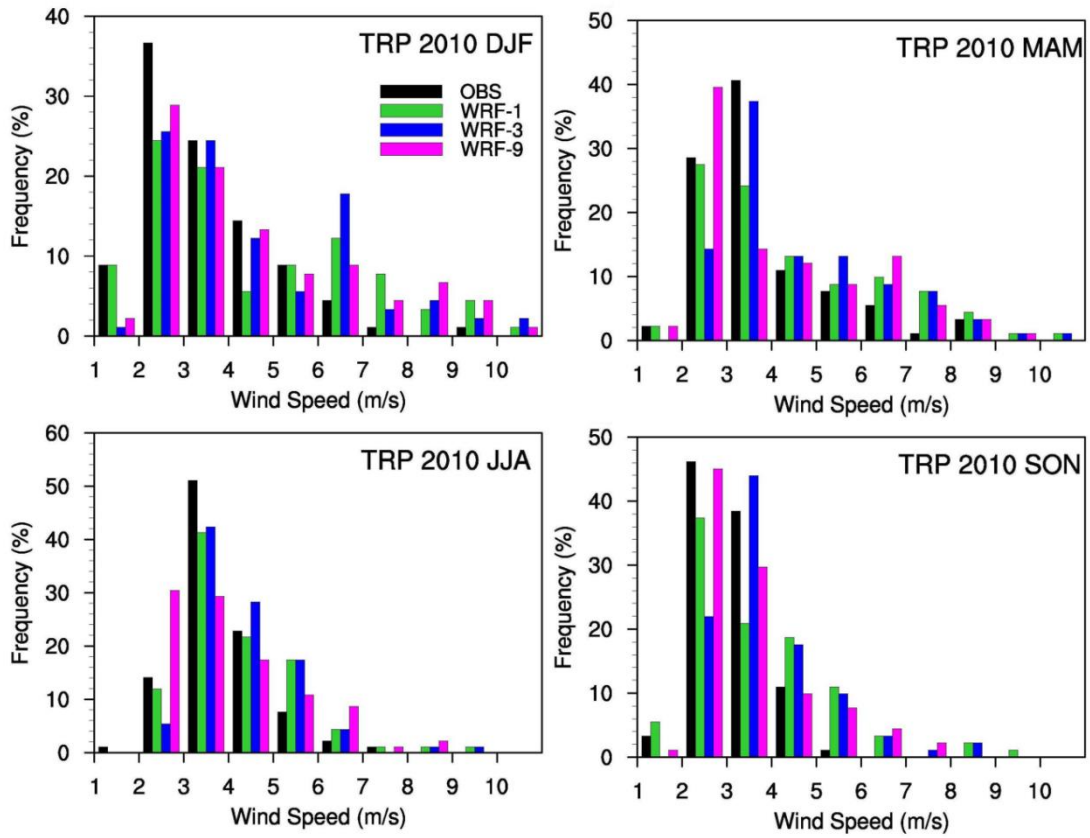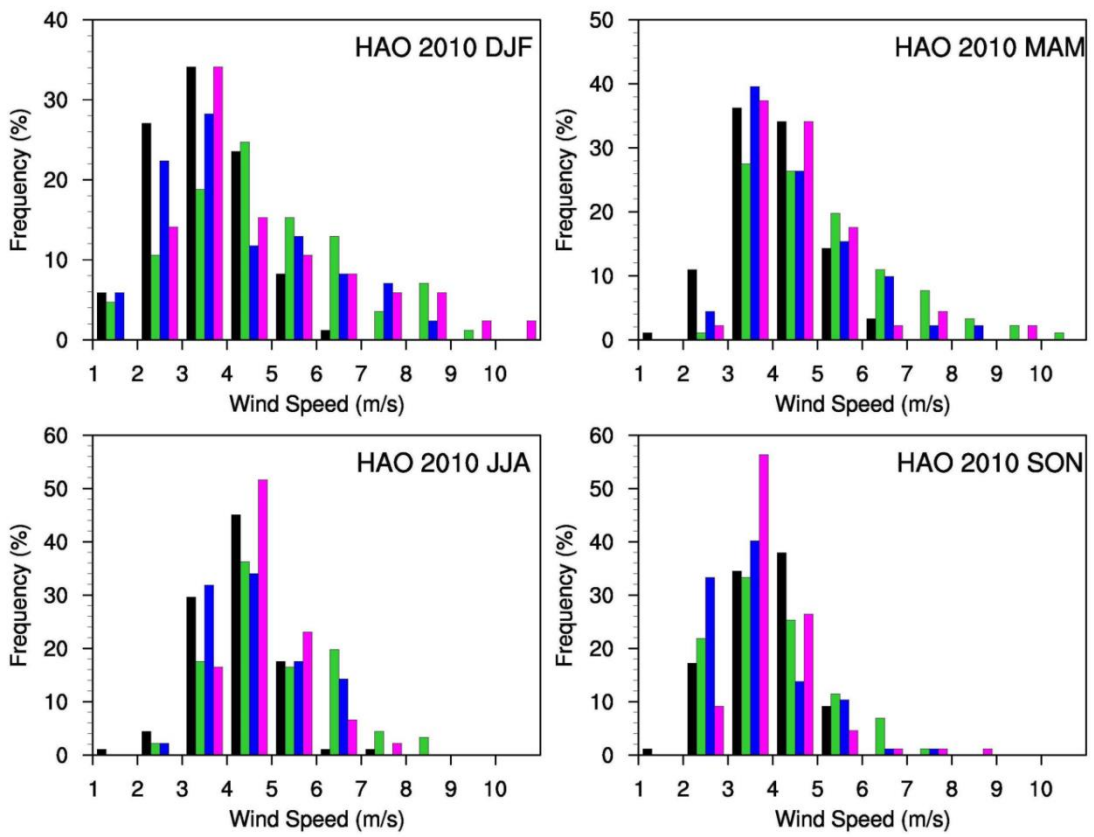
APPENDIX G

Publications to date

Refereed Journal Papers

1. El-Samra, R., Bou-Zeid, E., and El-Fadel, M. (2016a). What model resolution is required in climatological downscaling over a complex terrain? *Atmospheric Research*, "in revision"

2. El-Samra, R., Bou-Zeid, E., and El-Fadel, M. (2016b). Can high resolution dynamical downscaling improve the representation of climatic extremes over complex terrain? *Theoretical and Applied Climatology*, "in revision"

3. El-Samra, R., Bou-Zeid. E., Bangalath, H.K., Stenchikov, G., and El-Fadel, M. (2016c). Future intensification of hydro-meteorological extremes: Downscaling using the Weather Research and Forecasting model. *Climate Dynamics*, "in press"
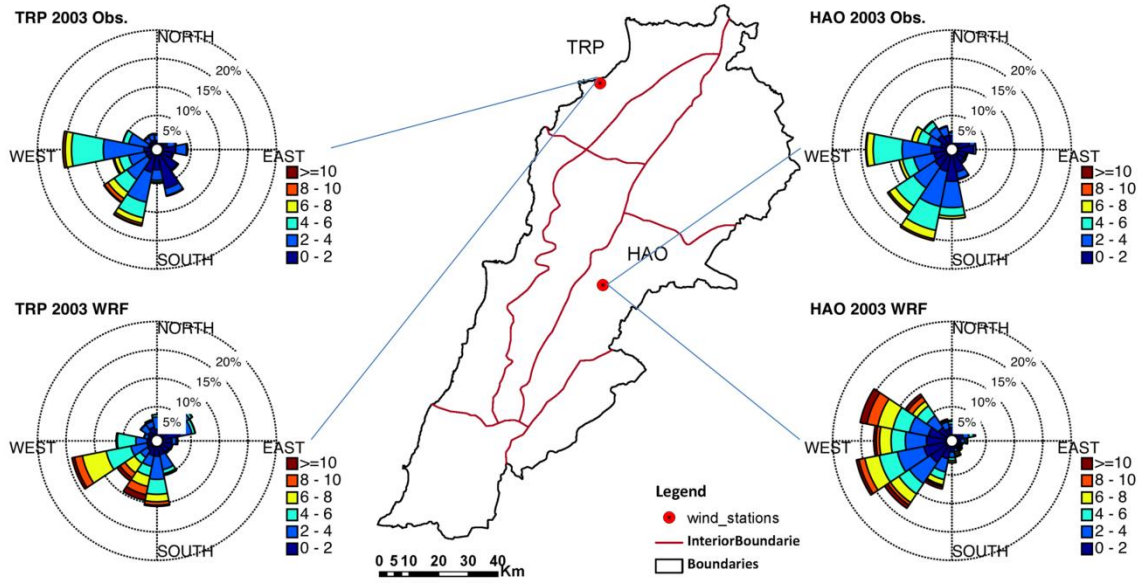
4. El-Samra, R., Bou-Zeid. E., Bangalath, H.K., Stenchikov, G., and El-Fadel, M. (2016d). Seasonal and regional patterns of intensification of future temperature extremes from high-resolution dynamic downscaling over complex terrain. *Climate Dynamics*, "under review"

5. El-Samra, R., El-Fadel, M., Zurayk, R., Bou-Zeid, E., Abou Najm, M., Alameddine, I., Bangalath, H.K., Stenchikov, G., and (2016e). Downscaling for assessing climate change impacts on silage maize yield in semi-arid regions, *Regional Environmental Change* "under review"

Conference Proceedings

1. El-Samra, R., Bou-Zeid, E., Bangalath, K.H., Stenchikov, G., and El-Fadel M. Will extremes become the norm under future climate change? *World Conference on Climate Change*, October 24-26, 2016, Valencia, Spain. (*Speaker*)

2. El-Samra, R., Bou-Zeid, E., Bangalath, K.H., Stenchikov, G., and El-Fadel M. Regional Changes under Extreme Meteorological Events. *World Academy of Science, Engineering and Technology, ICECC 2016: 18th International Conference on Environment and Climate Change*, January, 12-13, 2016, Zurich, Switzerland. (*Speaker*)

3. El-Samra, R., Bou-Zeid, E., and El-Fadel, M. Evaluation of WRF High Resolution Dynamical Downscaling Simulations over Lebanon. *American Meteorological Society, 27th Conference On Weather Analysis And Forecasting/23rd Conference On Numerical Weather Prediction*, 29 June–3 July 2015, Chicago, IL., USA. (*Speaker*)

4. El-Samra, R., Bou-Zeid, E., and El-Fadel, M. An Integrated Modeling Approach for Assessing the Impact of Climate Change on the Water, Energy, Food and Ecosystems nexus. *5th Beirut Water Week: Water, Energy, Food and Ecosystems Nexus in the Mediterranean Region*, May 22-23, 2014, Notre Dame University, Lebanon. (*Speaker*)

BIBLIOGRAPHY

Abdul-Rahman, S., Saoud, I.P., Owaied, M.K., Holail, H., Farajalla, N., Haidar M., & Ghanawi, J. (2011). Improving water use efficiency in semi-arid regions through integrated aquaculture/agriculture. *Journal of Applied Aquaculture*, 23(3), 212-230, doi: 10.1080/10454438.2011.600629

Abraha, M. G., and Savage, M. J. (2006). Potential impacts of climate change on the grain yield of maize for the midlands of KwaZulu-Natal, South Africa. *Agriculture, Ecosystems and Environment*, 115(1), 150-160. doi:10.1016/j.agee.2005.12.020

Abraha, M.G., and Savage, M.J. (2008). The soil water balance of rainfed and irrigated oats, Italian rye grass and rye using the CropSyst model. *Irrig Sci*, 26, 203. doi:10.1007/s00271-007-0086-8

Addiscott, T. M., and Whitmore, A. P. (1987). Computer simulation of changes in soil mineral nitrogen and crop nitrogen during autumn, winter and spring. *The Journal of Agricultural Science*, 109(1), 141-157. doi:10.1017/S0021859600081089

Ahn, J.B., Hong, J.Y. & Shim, K.M. (2015). Agro-climate changes over Northeast Asia in RCP scenarios simulated by WRF. *Int. J. Climatol.*, 36, 1278–1290. doi:10.1002/joc.4423

Akadan, A.R. (2008). Climatic Changes in Lebanon, Predicting Uncertain Precipitation Events — Do Climatic Cycles Exist? In Climatic changes and water resources in the Middle East and North Africa. Ed F. Zereini and H. Hötz, doi: 10.1007/978-3-540-85047-2_6

Alexandratos, N., and Bruinsma, J. (2012). *World agriculture towards 2030/2050: the 2012 revision* (No. 12-03, p. 4). Rome, FAO: ESA Working paper

Allen, G., Pereira, L.S., Raes, D., & Smith, M. (1998). Crop evapotranspiration: guidelines for computing crop water requirements. *FAO Irrigation and Drainage Paper 56*. FAO: Rome, Italy

Alpert, P., Krichak, S. O., Shafir, H., Haim, D., & Osetinsky, I. (2008). Climatic trends to extremes employing regional modeling and statistical interpretation over the E. Mediterranean. *Global and Planetary* Change*, 63*(2–3), 163-170, doi:http://dx.doi.org/10.1016/j.gloplacha.2008.03.003

Alexander, L., et al. (2006) Global Observed Changes in Daily Climate Extremes of Temperature and Precipitation. *Journal of Geophysical Research*, 111, 1-22. http://dx.doi.org/10.1029/2005JD006290

Alexander, L., and Tebaldi, C. (2012). Climate and Weather Extremes: Observations, Modelling, and Projections. *The Future of the World's Climate*. doi: 10.1016/B978-0-12-386917-3.00010-5

Alves, O., Balmaseda, M., Anderson, D., & Stockdale, T. (2004). Sensitivity of dynamical seasonal forecasts to ocean initial conditions. *Quarterly Journal Royal Meteorological Society*, 130, 647-668. doi:10.1256/qj.03.25.

Andrys, J., Lyons, T.L., & Kala, J. (2015). Multidecadal evaluation of WRF downscaling capabilities over estern Australia in simulating rainfall and temperature extremes. *Journal of Applied Meteorology and Climatology*, 54, 370-393, doi: 10.1175/JAMC-D-14-0212.1

Angström, A. (1924). Solar and terrestrial radiation. *Quarterly Journal of the Royal Meteorological Society*, 50,121–125

Antic, S., Laprise, R., Denis, B., &de Elia, R. (2004). Testing the downscaling ability of a one-way nested regional climate model in regions of complex topography. *Climate Dynamics,* 23, 473–493. doi: 10.1007/s00382-004-0438-5

Anwar, M. R., O'leary, G., McNeil, D., Hossain, H., & Nelson, R. (2007). Climate change impact on rainfed wheat in south-eastern Australia. *Field Crops Research*, 104(1), 139-147. http://dx.doi.org/10.1016/j.fcr.2007.03.020.

AQUASTAT - FAO's Information System on Water ... – Agriculture (no date). Retrieved from http://www.fao.org/nr/water/aquastat/countries_regions/LBN/index.stm

Argüeso, D., Hidalgo-Muñoz, J.M., Gámiz-Fortis, S.R., Esteban-Parra, M.J., Dudhia, J., & Castro-Díez., Y. (2011). Evaluation of WRF parameterizations for climate studies over southern Spain using a multistep regionalization. *Journal of Climate*, 24 (21), 5633

Argüeso, D., Hidalgo-Muñoz, J.M, Gámiz-Fortis, S.R., Esteban-Parra, M.J., & Castro-Díez, Y. (2012). High-resolution projections of mean and extreme precipitation over Spain using the WRF model (2070-2099 versus 1970-1999). *Journal of Geophysical Research D: Atmospheres*, 117(12), D12108, doi: 10.1029/2011JD017399

Ashley, R.O. (2001). Corn Maturity and Ensiling Corn. Agronomy Management. https://www.ag.ndsu.edu/archive/dickinso/agronomy/cornmaturity.htm

Atlas Climatique du Liban. (1977). Ministère des travaux publics et des transports, Direction de l'aviation civile, Beyrouth, République Libanaise

Bangalath, H.K., and Stenchikov, G. (2015). Role of dust direct radiative effect on the tropical rain belt over Middle East and North Africa: A high-resolution AGCM study. *J. Geophys. Res. Atmos.*, 120, 4564–4584, doi: 10.1002/2015JD023122

Barrera-Escoda, A., Gonçalves, M., Guerreiro, D., Cunillera, J., & Baldasano, J.M. (2014). Projections of temperature and precipitation extremes in the North Western Mediterranean Basin by dynamical downscaling of climate scenarios at high resolution (1971–2050). *Climatic Change*, 122, 567–582, doi: 10.1007/s10584-013-1027-6

Beniston, M., Stephenson, D. B., Christensen, O. B., Ferro, C. A. T., Frei, C., Goyette, S., & Woth, K. (2007). Future extreme events in European climate: An exploration of regional climate model projections. *Climatic Change*, 81(S1), 71-95. doi:10.1007/s10584-006-9226-z

Benli, B., Pala, M., Stockle, C., & Oweis, T. (2007). Assessment of winter wheat production under early sowing with supplemental irrigation in a cold highland environment using CropSyst simulation model. *Agricultural Water Management*, 93(1), 45-53

Berg, P., Wagner, S., Kunstmann, H., & Schädler, G. (2013). High resolution regional climate model simulations for Germany: Part I-validation. *Climate Dynamic*, 40(1-2), 401-414, doi 10.1007/s00382-012-1508-8

Blandford, T., Humes, K., Harshburger, B., Moore, B., Walden, V., & Ye, H. (2008). Seasonal and synoptic variations in near-surface air temperature lapse rates in a mountainous basin. *J. Appl. Meteorol. Climatol.*, 47(1), 249–261, doi:10.1175/2007JAMC1565.1

Black, E., Brayshaw, D. J., & Rambeau, C. M. C. (2010). Past, present and future precipitation in the middle east: Insights from models and observations. *Philosophical Transactions of the Royal Society A: Mathematical, Physical and Engineering Sciences*, 368(1931), 5173-5184

Blanchet, G. (1965). Le climat de Beyrouth. *Revue de Géographie de Lyon*, 40, 131-158

Boggia, A., Luciani, F., Massei, G., Paolotti, L., Rocchi, L., & Sediari, T. (2013). An evaluation of climate change effects on agricultural systems: the case of Trasimeno Lake. *Quaderni del Dipartimento di Economia, Finanza e Statistica 125/2013*, Università di Perugia

Bolstad, P.V., Swift, L., Collins, F., & Regniere, J. (1998). Measured and predicted air temperatures at basin to regional scales in the southern Appalachian Mountains. *Agric. For. Meteorol.*, 91(3–4), 161–176

Bonfante, A., Basile, A., Acutis, M., De Mascellis, R., Manna, P., Perego, A., & Terribile, F. (2010). SWAP, CropSyst and MACRO comparison in two contrasting soils cropped with maize in Northern Italy. *Agricultural Water Management*, 97(7), 1051-1062

Bou-Zeid, E., and El-Fadel, M. (2002). Climate change and water resources in the Middle East: a vulnerability and adaptation assessment ASCE, *Journal of Water Resources Planning and Management*, 128(5), 343-355, doi: 10.1061/(ASCE)0733-9496(2002)128:5(343)

Bouazzama, B., Mailhol, J. C., Xanthoulis, D., Bouaziz, A., Ruelle, P., & Belhouchette, H. (2013). Silage Maize Growth Simulation Using Pilote and CropSyst Model. *Irrigation and Drainage*, 62(1), 84-96

Boulard, D., Pohl, B., Cretat, J., Vigaud, N., & Pham-Xuan, T. (2013). Downscaling large-scale climate variability using a regional climate model: The case of ENSO over Southern Africa. *Climate Dynamics*, 40 (5-6), 1141-1168, doi: 10.1007/s00382-012-1400-6

Bowden, J.H., Nolte, C.G., & Otte, T.L. (2013):.Simulating the impact of the large-scale circulation on the 2-m temperature and precipitation climatology. *Climate Dynamics*, 40 (7-8), 1903-1920, doi: 10.1007/s00382-012-1440-y

Brown, S.J., Caeser, J., & Ferro, C.A.T. (2008). Global changes in extreme daily temperature since 1950. *J. Geophys. Res.*, 113, D05115, doi: 10.1029/2006JD008091

Bukovsky, M.S., and Karoly, D.J. (2009). Precipitation simulations using WRF as a nested regional climate model. *Journal of Applied Meteorology and Climatology*, 48(10), 2152-2159, doi: 10.1175/2009JAMC2186.1

Caldwell, P., Chin, H.N.S., Bader, D.C., & Bala, G. (2009). Evaluation of a WRF dynamical downscaling simulation over California. *Climatic Change*, 95(3-4), 499-521, doi: 10.1007/s10584-009-9583-5

Cardoso, R.M., Soares, P.M.M., Miranda, P.M.A., & Belo-Pereira, M. (2012). WRF high resolution simulation of Iberian mean and extreme precipitation climate. *International Journal of Climatology*, 33(11), 2591-2608, doi: 10.1002/joc.3616

Castellvi, F., and Stöckle, C.O. (2002). Comparing the performance of WGEN and ClimGen in the generation of temperature and solar radiation. *Trans. ASAE 44*: 1683-1687

Chen, F., and Dudhia, J. (2001). Coupling an advanced land-surface hydrology model with the PennState NCAR MM5 modeling system. Part I: model description and implementation. *Mon Weather Rev.*, 129, 569–585

Chen, J., and Lin, S. (2011). The remarkable predictability of inter-annual variability of Atlantic hurricanes during the past decade. *Geophysical Research Letters*, 38(11), n/a, doi:http://dx.doi.org/10.1029/2011GL047629

Christetin, J.H., and Christenin, O.B. (2007). A summary of the PRUDENCE model projections of changes in European climate by the end of this century. *Climatic Change*, 81, 7-30, doi: 10.1007/s10584-006-9210-7

Christidis, N., Stott, P.A., & Brown, S. (2011). The role of human activity in the recent warming of extremely warm daytime temperatures. *Journal of Climate*, doi:10.1175/2011JCLI4150.1

Christidis, N., Stott, P.A., Brown, S., Hegerl, G.C., & Cesars, J. (2005). Detection of changes in temperature extremes during the second half of the 20th century. *Geophys. Res. Lett.*, 32, L20716, doi: 10.1029/2005GL023885

Clarke, L., Edmonds, J., Jacoby, H., Pitcher, H., Reilly, J., & Richels, R. (2007). Scenarios of Greenhouse Gas Emissions and Atmospheric Concentrations. Sub-report 2.1A of Synthesis and Assessment Product 2.1 by the U.S. Climate Change Science Program and the Subcommittee on Global Change Research. Department of Energy, Office of Biological & Environmental Research, Washington, 7 DC., USA, pp. 154

Collins, W., Bellouin, N., Woodward, S., et al. (2011). Development and evaluation of an Earth-System model-HadGEM2. *Geoscientific Model Development*, 4(4), 1051-1075, doi: 10.5194/gmd-4-1051-2011

Confalonieri, R., & Bechini, L. (2004). A preliminary evaluation of the simulation model CropSyst for alfalfa. *European Journal of Agronomy*, 21(2), 223-237

Davies, H.C. (1976). A lateral boundary formulation for multi-level prediction models. *Q. J. R. Meteorol. Soc.*, 102, 405–418

Delworth, T.L., Broccoli, A.J., Rosati, A., Stouffer, R.J., et al. (2006). GFDL's CM2 global coupled climate models. part I: Formulation and simulation characteristics. *Journal of Climate*, 19(5), 643-669,672-674

D'Ippoliti, D., Michelozzi, P., Marino, C., et al. (2010). The impact of heat waves on mortality in 9 European cities: results from the EuroHEAT project. *Environmental Health*; 9, 37, doi:10.1186/1476-069X-9-37

Díaz-Ambrona, C. G., Pazos, R. G., & Tovar, C. O. M. (2004). Global climate change and food security for small farmers in Honduras. *In 4th International Crop Science Congress*, Australia (Vol. 26)

Díaz-Ambrona, H., Gregorio, C., Gigena, R., & Mendoza, C. O. (2013). Climate change impacts on maize and dry bean yields of smallholder farmers in Honduras. *Iberoamerican Journal of Development Studies*, 2(1), 4-22

Diaz-Nieto, J., and Wilby, R.L. (2005). A comparison of statistical downscaling and climate change factor methods: impacts on low flows in the River Thames, United Kingdom. *Climatic Change*, 69, 245–68

Di Luca, A., Elía, R., & Laprise, R. (2015). Challenges in the quest for added value of regional climate dynamical downscaling.*Current Climate Change Reports*, 1 (1), 10-21

Di Piazza, A., Di Piazza, M. C., Ragusa, A. & Vitale, G. (2010). Statistical Processing of Wind Speed Data for Energy Forecast and Planning. *International Conference on Renewable Energies and Power Quality (ICRPQ,10)*. Granada, Spain

Döll, P. (2002). Impact of climate change and variability on irrigation requirements: A global perspective. *Climatic Change*, 54(3), 269-293. doi:10.1023/A:1016124032231

Döll, P., and Siebert, S. (2002). Global modeling of irrigation water requirements. *Water Resources Research*, 38(4), 1037. doi:10.1029/2001WR000355

Donatelli, M., Stöckle, C., Ceotto, E., & Rinaldi, M. (1997). Evaluation of CropSyst for cropping systems at two locations of northern and southern Italy. European Journal of Agronomy, 6(1), 35-45. doi:10.1016/S1161-0301(96)02029-1

Donner, L.J., Wyman, B.L., Hemler, R.S., Horowitz, L.W., Ming, Y., Zhao, M., Golaz, J.C., Ginoux, P., Lin, S.J., Schwarzkopf, M.D., Austin, J., Alaka, G., Cooke, W.F., Delworth, T.L., Freidenreich, S.M., Gordon, C.T., Griffies, S.M., Held, I.M., Hurlin, W.J., Klein, S.A., Knutson, T.R., Langenhorst, A.R., Lee, H.C., Lin, Y., Magi, B.I., Malyshev, S.L., Milly, P.C.D., Naik, V., Nath, M.J., Pincus, R., Ploshay, J.J., Ramaswamy, V., Seman, C.J., Shevliakova, E., Sirutis, J.J., Stern, W.F., Stouffer, R.J., Wilson, R.J., Winton, M., Wittenberg, A.T., & Zeng, F. (2011). The dynamical core, physical parameterizations, and basic simulation characteristics of the atmospheric component AM3 of the GFDL global coupled model CM3. *Journal of Climate*, 24 (13), 3484-3519, doi: 10.1175/2011JCLI3955.1

Dudhia, J. (1989). Numerical study of convection observed during the winter monsoon experiment using a mesoscale two-dimensional model. *J Atmos Sci.*, 46, 3077–3107

Easterling, D., Meehl, G., Parmesan, C., Changnon, S., Karl, T. & Mearns, L. (2000). Climate Extremes: Observations, Modeling and Impacts. *Science*, 289, 2068-2074, http://dx.doi.org/10.1126/science.289.5487.2068

El Afandi, G., Khalil, F. A., & Ouda, S. A. (2010). Using irrigation scheduling to increase water productivity of wheat-maize rotation under climate change conditions. *Chilean Journal of Agricultural Research*, 70(3)

El-Baroudy, A. A., Ouda, S. A., & Taha, A. M. (2013). Calibration of CropSyst model for wheat grown in sandy soil under fertigation treatments. *Egypt. J. Soil Sci.*

El-Fadel M. (2010).Climate Change Research and Capacity Needs and Opportunities in the Middle East: A Scoping Study. *International Development and Research Center*, Canada pp. 83 July 2010

El-Fadel M., Maroun R. & Ghanimeh S. (2012). IWRM for Climate Change Adaptation in the MENA region. *IWA World Congress on Water, Climate and Energy*, May 13-18 2012, Dublin, Ireland

Esquivel, G., Cerano, J., Sánchez, I., López, A., & Gutiérrez, O., G. (2015). Validación del modelo ClimGen en la estimación de variables de clima ante escenarios de datos faltantes con fines de modelación de procesos/Validation of the ClimGen model to estimate climate variables when lacking data for modeling processes. *Tecnología y Ciencias Del Agua*, 6(4), 117-130

Esteban, M.A., & Chen, Y.L. (2008). The impact of trade wind strength on precipitation over the windward side of the island of Hawaii. *Mon*, 136, 913-928, doi: 10.1175/2007MWR2059.1

Evans, J. P., Smith, R. B., & Oglesby, R. J. (2004). Middle East climate simulation and dominant precipitation processes. *Int. J. Climatol., 24,* 1671–1694

Evans, J. P. (2009). 21st century climate change in the Middle East. *Climatic Change, 92*(3-4), 417-432

Evans, J., McGregor, J., & McGuffie, K. (2012). Chapter 9 - Future regional climates. In Ann Henderson-Sellers, & Kendal McGuffie (Eds.). The future of the world's climate (second edition) (pp. 223-250). Boston: Elsevier, doi: 10.1016/B978-0-12-386917-3.00009-9

Ferreira, J.A., Carvalho, A.C., Carvalheiroc, L., Rochad, A., & Castanheira, J.M. (2014). On the influence of physical parameterisations and domains configuration in the simulation of an extreme precipitation event. *Dynamics of Atmospheres and Oceans*, 68, 35–55, http://dx.doi.org/10.1016/j.dynatmoce.2014.08.001

Fischer, G., Tubiello, F. N., van Velthuizen, H., & Wiberg, D. A. (2007). Climate change impacts on irrigation water requirements: Effects of mitigation, 1990–2080. *Technological Forecasting & Social Change*, 74(7), 1083-1107. doi:10.1016/j.techfore.2006.05.021

Flaounas, E., Drobinski, P., & Bastin, S. (2013a). Dynamical downscaling of IPSL-CM5 CMIP5 historical simulations over the Mediterranean: Benefits on the representation of regional surface winds and cyclogenesis. *Climate Dynamics*, 40(9-10), 2497-2513, doi: 10.1007/s00382-012-1606-7

Flaounas, E., Drobinski, P., Vrac, M., Bastin, S., Lebeaupin-Brossier, C., Stéfanon, M., Borga, M., & Calvet, J.C. (2013b). Precipitation and temperature space-time variability and extremes in the Mediterranean region: Evaluation of dynamical and statistical downscaling methods. *Climate Dynamics*, 40(11-12), 2687-2705, doi: 10.1007/s00382-012-1558-y

Food and Agriculture Organization(FAO). (2013). http://faostat3.fao.org/browse/Q/QC/E

Fowler, H.J., Blenkinsop, S., & Tebaldi, C. (2007). Linking climate change modelling to impacts studies: recent advances in downscaling techniques for hydrological modeling. *Int. J. Climatol.*, 27, 1547–78, doi: 10.1002/joc.1556

Friedl, M. A., McIver, D. K., Zhang, X. Y., Hodges, J. C. F., Schnieder, A., Bacinni, A., ... & Liu, W., 2001. Global land cover classification results from MODIS. In *Geoscience and Remote Sensing Symposium, 2001. IGARSS'01. IEEE 2001 International* (Vol. 2), 733-735, doi:10.1109/IGARSS.2001.976618

Gall, J.S., Ginis, I., Lin, S.J., Marchok, T.P., & Chen, J.H. (2011). Experimental tropical cyclone prediction using the GFDL 25-km-resolution global atmospheric model. *Weather and Forecasting*, 26(6), 1008-1019, doi: 10.1175/WAF-D-10-05015.1

Gao, Y., Fu, J.S., Drake, J. B., Liu, Y., & Lamarque, J. F. (2012). Projected changes of extreme weather events in the eastern United States based on a high resolution climate modeling system. *Environmental Research Letters*, 7(4): 044025, doi:10.1088/1748-9326/7/4/044025

Gardner, A.S., Sharp, M.J., Koerner, R.M., Labine, C., Boon, S., Marshall, S.J., Burgess, D.O., & Lewis, D., (2009). Near-surface temperature lapse rates over Arctic glaciers and their implications for temperature downscaling. *J. Clim.*, 22(16), 4281–4298, doi:10.1175/2009JCLI2845.1

Gent, P.R., Danabasoqlu, G., Donner, L.J., Holland, M.M., Hunke, E.C. et al. (2011). The Community Climate System Model Version 4. *J. Clim.*, 24, 4973–4991, doi: 10.1175/2011JCLI4083.1

Giorgi, F. (1990). Simulation of regional climate using a limited area model nested in a general circulation model. *American Meteorological Society*, 3, 941-963

Giorgi, F. (2006). Climate change hot-spots. *Geophys. Res. Lett.*, 33, L08707, doi:10.1029/2006GL025734

Giorgi, F., Jones, F., & Asrar, G.R. (2009). Addressing climate information needs at the regional level: the CORDEX framework. *WMO Bulletin*, 58 (3) - July 2009

Giorgi, F., and Lionello, P. (2008). Climate change projections for the Mediterranean region. *Global and Planetary Change*, 63(2-3), 90-104

Giorgi, F., and Mearns, L.O. (1991). Approaches to the simulation of regional climate change: A review. *Reviews of Geophysics*, 29(2), 191-216

Giorgi, F., Whetton, P. H., Jones, R. G., Christensen, J. H., Mearns, L. O., Hewitson, B., von Storch, H., Francisco, R., & Jack, C. (2001). Emerging patterns of simulated regional climatic changes for the 21st century due to anthropogenic forcings. *Geophysical Research Letters, 28*(17), 3317-3320

Givati, A., Lynn, B., Liu, Y., & Rimmer, A. (2012). Using the WRF model in an operational streamflow forecast system for the Jordan River. *Journal of Applied Meteorology and Climatology*, 51(2), 285-299, doi: 10.1175/JAMC-D-11-082.1

Gonçalves, M., Barrera-Escoda, A., Guerreiro, D., Baldasano, J.M., & Cunillera, J. (2013). Seasonal to yearly assessment of temperature and precipitation trends in the North Western Mediterranean Basin by dynamical downscaling of climate scenarios at high resolution (1971–2050). *Climatic Change*, 122, 243–256

Gornall, J., Betts, R., Burke, E., Clark, R., Camp, J., Willett, K., & Wiltshire, A. (2010). Implications of climate change for agricultural productivity in the early twenty-first century. *Philosophical Transactions: Biological Sciences*, 365(1554), 2973-2989. doi:10.1098/rstb.2010.0158

Hadjinicolaou, P., Giannakopoulos, C., Zerefos, C., Lange, M.A., Pashiardis, S., Lelieveld, J. (2011). Mid-21st century climate and weather extremes in Cyprus as projected by six regional climate models. *Reg Environ Change*, 11, 441–457, doi 10.1007/s10113-010-0153-1

Heikkilä, U., Sandvik, A., & Sorteberg, A. (2011). Dynamical downscaling of ERA-40 in complex terrain using the WRF regional climate model. *Climate Dynamics*, 37(7-8), 1551-1564, doi: 10.1007/s00382-010-0928-6

Hofstra, N., Haylock, M., New, M., & Jones, P.D. (2009). Testing EOBS European high-resolution gridded dataset of daily precipitation and surface temperature. *J Geophys Res.*, doi: 10.1029/2009 JD011799

Holzkämper, A., Calanca, P., Honti, M., & Fuhrer, J. (2015). Projecting climate change impacts on grain maize based on three different crop model approaches. *Agricultural and Forest Meteorology*, 214-215, 219-230. doi:10.1016/j.agrformet.2015.08.263

Hong, S.Y., and Lim, J.O.J. (2006). The WRF single-moment 6-class microphysics scheme (WSM6*). J Korean Meteor Soc.*, 42(2), 129–151

Huang, J., and Bou-Zeid, E. (2013). Turbulence and vertical fluxes in the stable atmospheric boundary-layer I: A large-eddy simulation study. *Journal of the Atmospheric Sciences*, 70(6), 1513-1527, doi: 10.1175/JAS-D-12-0167.1

Huang, J., Bou-Zeid, E., and Golaz, J.C. (2013). Turbulence and vertical fluxes in the stable atmospheric boundary-layer II: A novel mixing length model. *Journal of the Atmospheric Sciences*, 70(6), 1528-1542, doi:/10.1175/JAS-D-12-0168.1

Intergovernmental Panel on Climate Change (IPCC). (2013). In: Stocker, T.F., D. Qin, G.-K. Plattner, M. Tignor, S.K. Allen, J. Boschung, A. Nauels, Y. Xia, V. Bex and P.M. Midgley (Eds.), Climate Change 2013. The Physical Science Basis. Contribution of Working Group I to the Fifth Assessment Report of the Intergovernmental Panel on Climate Change. Cambridge University Press, Cambridge, United Kingdom and New York, NY, USA

Jalota, S. K., Singh, G. B., Ray, S. S., Sood, A. N. I. L., & Panigrahy, S. U. S. H. M. A. (2006). Performance of Cropsyst model in rice–wheat cropping system. *J. Agric. Phys*, 6, 7-13

Jamieson, P.D., Porter, J. R., Goudriaan, J., Ritchie, J.T., van Keulen, H., & Stol, W. (1998). A comparison of the models AFRCWHEAT2, CERES-Wheat, Sirius, SUCROS2 and SWHEAT with measurements from wheat grown under drought. *Field Crops Res*. 55:23–44

Janjic, Z.I. (2001). Nonsingular implementation of the Mellor-Yamada level 2.5 scheme in the NCEP Meso model, *Off. Note 437*, 61, Natl. Cent. for Environ. Prot., Boulder, Colorado

Jiang, X., Waliser, D.E., Kim, D., Zhao, M., Sperber, K. R., Stern, W. F., Schubert, S. D., Zhang, G.J., Wang,W., Khairoutdinov, M., Neale, R. B., .& Lee, M. . (2012). Simulation of the intraseasonal variability over the eastern Pacific ITCZ in climate models. *Climate Dynamics*, 39(3), 617-636, doi: 10.1007/s00382-011-1098-x

Karam, F., Breidy, J., Stephan, C., & Rouphael, J. (2003). Evapotranspiration, yield and water use efficiency of drip irrigated corn in the Bekaa valley of Lebanon. *Agricultural Water Management*, 63(2), 125-137. doi:10.1016/S0378-3774(03)00179-3

Karmalkar, A., McSweeney, C., New, M., & Lizcano, G. (2012). *UNDP climate change country profiles: Lebanon*. Available online at http://country-profiles.geog.ox.ac.uk

Katsafados, P., Papadopoulos, A., Varlas, G., Papadopoulou, E., & Mavromatidis, E. (2013). Seasonal predictability of the 2010 Russian heat wave. *Nat. Hazards Earth Syst. Sci. Discuss.*, 1: 5057–5086, doi: 10.5194/nhessd-1-5057-2013

Kitoh, A., Yatagai, A. & Alpert, P. (2008). First super-high resolution model projection that the ancient 'Fertile Crescent' will disappear in this century. *Hydrol. Res. Lett. 2,* 1–4, doi:10.3178/hrl.2.1

Kobayashi, K., and Salam, M.U. (2000). Comparing simulated and measured values using mean squared deviation and its components. *Agronomy Journal*, 92 (2), 345-352

Laprise, R. (2008). Regional climate modelling. *Journal of Computational Physics*, 227(7), 3641-3666, doi:10.1016/j.jcp.2006.10.024

Laux, P., Kunstmann, H., Bárdossy, A. (2008). Predicting the regional onset of the rainy season in West Africa. *Int. J. Climatol.*, 28, 329–342. http://dx.doi.org/10.1002/joc.1542

Laux, P., Jäckel, G., Tingem, R. M., & Kunstmann, H. (2010). Impact of climate change on agricultural productivity under rainfed conditions in Cameroon—A method to improve attainable crop yields by planting date adaptations. *Agricultural and Forest Meteorology*, 150(9), 1258-1271

Lebanon FNC (First National Communications to the UNFCCC) (1999). Ministry of Environment, Republic of Lebanon

Lebanon SNC (Second National Communications to the UNFCCC). (2011). Ministry of Environment, Republic of Lebanon

Lebeaupin-Brossier, C., Béranger, K., Deltel, C., & Drobinski, P. (2011). The Mediterranean response to different space–time resolution atmospheric forcings using perpetual mode sensitivity simulations. *Ocean Modelling*, 36(1–2), 1-25, doi:10.1016/j.ocemod.2010.10.008

Lee, C.D., Herbek, J.H., Lacefield, G., & Smith, R. (2006). Producing corn for silage. Corporative Extension Services, University of Kentucky, Collage for Agriculture. AGR-79, 1-8

Lelieveld, J., Hadjinicolaou, P., Kostopoulou, E., Giannakopoulos, C., Pozzer, A., Tanarhte, M., Tyrlis, E. (2014). Model projected heat extremes and air pollution in the eastern Mediterranean and Middle East in the twenty-first century. *Reg Environ Chang*, 14, 1937. doi:10.1007/s10113-013-0444-4

Leung, L.R., and Qian, Y. (2003). The sensitivity of precipitation and snowpack simulations to model resolution via nesting in regions of complex terrain. *J Hydrometeorol.*, 4,1025–1043

Leung, L.R., Wigmosta, M.S., Ghan, S.J., Epstein, D.J., &Vail, L.W. (1996). Application of a subgrid orographic precipitation/surface hydrology scheme to a mountain watershed. *J. Geophys. Res.*, 101, 12803–17

Li, D., and Bou-Zeid, E. (2013). Synergistic interactions between urban heat islands and heat waves: the impact in cities is larger than the sum of its parts. *Journal of Applied Meteorology and Climatology*, 52 (9): 2051-2064. doi: 10.1175/JAMC-D-13-02.1

Li, D., Bou-Zeid, E., Baeck, M.L., Jessup, S., & Smith, J.A. (2013). Modeling land surface processes and heavy rainfall in urban environments: Sensitivity to urban surface representations. *Journal of Hydrometeorology*, 14(4), 1098-1118, doi: 10.1175/JHM-D-12-0154.1

Lin, S. J. (2004)., A "vertically Lagrangian" finite-volume dynamical core for global models. *Mon. Weather Rev.*, 132(10), 2293–2307, doi:10.1175/1520-0493(2004)132<2293:AVLFDC>2.0.CO;2

Lo, J.C.F., Yang, Z.L., & Pielke Sr., R.A. (2008). Assessment of three dynamical climate downscaling methods using the weather research and forecasting (WRF) model. *Journal of Geophysical Research D: Atmospheres*, 113(9), D09112, doi: 10.1029/2007JD009216

Lobell, D. B., and Field, C. B. (2007). Global scale climate–crop yield relationships and the impacts of recent warming. *Environmental Research Letters*, 2(1), 014002. doi:10.1088/1748-9326/2/1/014002

Lynch, P. (2008). The origins of computer weather prediction and climate modeling. *Journal of Computational Physics*, 227(7), 3431-3444, doi: 10.1016/j.jcp.2007.02.034

Mathews, M., Schwankl, L., & Snyder, R. (no date). Corn Irrigation in a dry year. Accessed online: http://ucce.ucdavis.edu/files/filelibrary/5049/17591.pdf

Martin, G.M., Bellouin, N., Derbyshire, S. et al. (2011). The HadGEM2 family of Met Office Unified Model climate configurations. *Geophys. Model Dev.*, 4, 723–757. doi:10.5194/gmd-4-723-2011

McKague, K., Rudra, R., Ogilvie, J., Ahmed, I., & Gharabaghi, B. (2005). Evaluation of weather generator ClimGen for southern Ontario. Canadian *Water Resources Journal*, 30(4), 315

Meehl, G., et al. (2000). An Introduction to Trends in Extreme Weather and Climate Events: Observations, Socioeconomic Impacts, Terrestrial Ecological Impacts and Model Projections. *Bulletin of the American Meteorological Society*, 81, 413-416. http://dx.doi.org/10.1175/1520-0477(2000)081<0413:AITTIE>2.3.CO;2

Meehl, G.A., Covey, C., Taylor, K.E., Delworth, T., Stouffer, R.J., Latif, M., McAvaney, B., & Mitchell, J.F.B. (2007). The WCRP CMIP3 multimodel dataset: a new era in climate change research. *Bull. Am.Meteorol. Soc*. 88: 1383–1394, doi: 10.1175/BAMS-88-9-1383

Meinshausen, M., Smith, S. J., Calvin, K. V., Daniel, J. S., Kainuma, M. L. T., Lamarque, J.-F., Matsumoto, K., Montzka, S. A., Raper, S. C. B., Riahi, K., Thomson, A. M., Velders, G. J. M., & van Vuuren, D. (2011). The RCP greenhouse gas concentrations and their extension from 1765 to 2300. *Climatic Change (Special Issue)*, doi: 10.1007/s10584-011-0156-z

Mellor, G.L., and Yamada, T. (1974). A hierarchy of turbulence closure models for planetary boundary layers. *J. Atmos. Sci.*, 31, 1791–1806

Minder, J.R., Mote, P.W., and Lundquist, J.D. (2010). Surface temperature lapse rates over complex terrain: Lessons from the Cascade Mountains. *J. Geophys. Res.*, 115, D14122, doi: 10.1029/2009JD013493

Mlawer, E.J., Taubman, S.J., Brown, P.D., Iacono, M.J., and Clough, S.A. (1997). Radiative transfer for inhomogeneous atmosphere: RRTM, a validated correlated-k model for the longwave. *J Geophys Res*, 102, 16663–16682

Mohan, M., Sati, A.P. (2016). WRF model performance analysis for a suite of simulation design. *Atmos. Res,*. 169, 280–291. doi:10.1016/j.atmosres.2015.10.013

Monteith, J. L. (1981). Climatic variation and the growth of crops. *Quarterly Journal of the Royal Meteorological Society*, 107(454), 749-774

Morari, F., Berti, A., Borin, M., Giardini, L., & Sangiorgi, F. (2001). CropSyst model in simulating cropping systems with different input levels. InTechnology transfer. *Proceedings of the 9th International Conference on the FAO ESCORENA Network on recycling of agricultural, municipal and industrial residues in agriculture*, Gargano, Italy, 6-9 September 2000. (pp. 257-262)

Murphy, J.M., Sexton, D.M.H., Barnett, D.H., Jones, G.S., Webb, M.J., Collins, M., & Stainforth, D.A. (2004). Quantification of modelling uncertainties in a large ensemble of climate change simulations. *Nature*, 430(7001), 768-772, doi: 10.1038/nature02770

National Climatic Data Center (NCDC). (2013). Billion-Dollar Weather/Climate Disasters. Accessed online at: http://www.ncdc.noaa.gov/billions/

National Centers for Environmental Prediction /National Weather Service/NOAA/U.S. Department of Commerce. (2000). NCEP FNL Operational Model Global Tropospheric Analyses, continuing from July 1999. Research Data Archive at the National Center for Atmospheric Research, Computational and Information Systems Laboratory, Boulder, CO. [Available online at http://dx.doi.org/10.5065/D6M043C6.]

Nelson, R. (2002). ClimGen for Windows, a weather generator program. Agric. Engineering Dept., Washington State University, Pullman, WA

O'Gorman, P.A. (2015). Precipitation Extremes under Climate Change. *Curr Clim Change Rep*, 1,49–59. doi 10.1007/s40641-015-0009-3

OECD/Food and Agriculture Organization of the United Nations. (2013). *OECD-FAO Agricultural Outlook 2013*, OECD Publishing. http://dx.doi.org/10.1787/agr_outlook-2013-en

Olesen, J.E., and Bindi, M. (2002). Consequences of climate change for European agricultural productivity, land use and policy. *European Journal of Agronomy*, 16(4): 239-262, http://dx.doi.org/10.1016/S1161-0301(02)00004-7

Ouda, S. A., Taha, A. M., & Ibrahim, M. M. (2015). Water management for maize grown in sandy soil under climate change conditions. *Archives of Agronomy and Soil Science*, 61(3), 299-311

Paimazumder, D., Henderson, D., & Mölders, N. (2012). Evaluation of WRF-forecasts over Siberia: Air mass formation, clouds and precipitation. *Open Atmospheric Science Journal*, 6(1), 93-110

Pala, M., Stöckle, C. O., & Harris, H. C. (1996). Simulation of durum wheat (triticum turgidum ssp. durum) growth under different water and nitrogen regimes in a Mediterranean environment using CropSyst. Agricultural Systems, 51(2), 147-163. doi:10.1016/0308-521X(95)00043-5

Pan, Z., Takle, E., Gutowski, W., &Turner, R. (1999). Long simulation of regional climate as a sequence of short segments. *Mon Weather Rev*, 127, 308–321

Pan, L.L., Chen, S.H., Cayan, D., Lin, M.Y., Hart, Q., Zhang, M.H., Liu, Y., & Wang, J. (2011). Influences of climate change on California and Nevada regions revealed by a high-resolution dynamical downscaling study. *Climate Dynamics*, 37, 2005-2020, doi: 10.1007/s00382-010-0961-5

Persson, G., Bärring, L., Kjellström, E., Strandberg, G., & Rummukainen, M. (2007). Climate indices for vulnerability assessments. *Swedish Meteorological and Hydrological Institute Meteorology and Climatology Rep. (RMK),* 111, 80 pp. Available online at http://www.smhi.se/polopoly_fs/1.805!Climate%20indices%20for%20vulnerability%20assessments.pdf

Piazza, A. Di, Piazza, M. Di, Heikkilä, U., Sandvik, A., Sorteberg, A., Giorgi, F., Mearns, L., Friedl, M. ~A., McIver, D. ~K., Zhang, X. ~Y., Hodges, J. ~C. ~F., Schnieder, A., Bacinni, A., Strahler, A. ~H., Cooper, A., Gao, F., Schaaf, Liu, W., Esteban, M.A., Chen, Y.-L., Di Luca, A., de Elía, R., Laprise, R., Chen, F., Dudhia, J., Caldwell, P., Chin, H.N.S., Bader, D.C., Bala, G., Bukovsky, M.S., Karoly, D.J., Berg, P., Wagner, S., Kunstmann, H., Schädler, G., Argüeso, D., Hidalgo-Muñoz, J.M., Gámiz-Fortis, S.R., Esteban-Parra, M.J., Dudhia, J., Castro-Díez, Y. (2009). Statistical processing of wind speed data for energy forecast and planning. *Clim. Dyn*., 33, 401–414. doi:10.1029/2011JD017399

Qian, Y., Ghan, S.J., & Leung, L.R. (2010). Downscaling hydroclimatic changes over the western US based on CAM subgrid scheme and WRF regional climate simulations. *International Journal of Climatology*, 30(5), 675-693, doi: 10.1002/joc.1928

Quintana Seguí, P., Ribes, A., Martin, E., Habets, F., & Boé, J. (2010). Comparison of three downscaling methods in simulating the impact of climate change on the hydrology of Mediterranean basins. *Journal of Hydrology*, 383(1-2), 111-124

Rahmstorf, S., and Coumou, D. (2011). Increase of extreme events in a warming world. *PNAS*, 108 (44): 17905-17909, doi: 10.1073/pnas.1101766108

Ramamurthy, P., Li, D., & Bou-Zeid, E. (2016). High-resolution Simulation of Heatwave Events in New York City. *Theoretical and Applied Climatology*, doi: 10.1007/s00704-015-1703-8

Remesan, R., Bellerby, T., Holman, I., Frostick, L. (2015). WRF model sensitivity to choice of parameterization: A study of the 'York flood 1999'.*Theoretical and Applied Climatology*, 122 (1), 229-47

Reilly, J., Tubiello, F., McCarl, B., Abler, D., Darwin, R., Fuglie, K., & Rosenzweig, C. (2003). U.S. agriculture and climate change: New results. *Climatic Change*, 57(1), 43-67. doi:10.1023/A:1022103315424

Riahi, K., Grübler, A., & Nakicenovic, N. (2007). Scenarios of long-term socio-economic and environmental development under climate stabilization. *Technological Forecasting and Social Change*, 74(7), 887-935

Robine, J., Cheung, S.L.K., Le Roy, S., Van Oyen, H., Griffiths, C., Michel, J., & Herrmann, F.R. (2008). Death toll exceeded 70,000 in Europe during the summer of 2003. *Comptes Rendus Biologies*, 331(2), 171-178, doi: http://dx.doi.org/10.1016/j.crvi.2007.12.001

Rolland, C. (2003). Spatial and seasonal variations of air temperature lapse rates in Alpine regions. *J. Clim.*, 16(7), 1032–1046

Romano, N., Brunone, B., & Santini, A. (1998). Numerical analysis of one-dimensional unsaturated flow in layered soils. *Advances in Water Resources*, 21(4), 315-324, ISSN 0309-1708, http://dx.doi.org/10.1016/S0309-1708(96)00059-0

Rostkier-Edelstein, D., Liu, Y., Wu, W., Kunin, P., Givati, A., & Ge, M. (2014). Towards a high-resolution climatography of seasonal precipitation over Israel. *Int. J. Climatol.*, 34, 1964–1979, doi: 10.1002/joc.3814

Roth, G.W., and Heinrichs, A.J. (2001). Corn Silage Production and Management. *Agronomy Facts 18*. Penn State Extension. Accessed online: http://extension.psu.edu/plants/crops/grains/corn/silage/corn-silage-production-and-management

Ruby Leung, L., and Qian, Y. (2009). Atmospheric rivers induced heavy precipitation and flooding in the western U.S. simulated by the WRF regional climate model. *Geophysical Research Letters*, 36 (3), L03820, doi: 10.1029/2008GL036445

Ruiz, J.J., Saulo, C., & Nogués-Paegle, J. (2010). WRF Model Sensitivity to Choice of Parameterization over South America: Validation against Surface Variables. *Monthly Weather Review*, 138 (8), 3342-3355

Rummukainen, M. (2010). State-of-the-art with regional climate models. *Wiley Interdisciplinary Reviews: Climate Change*, 1 (1), 82-96

Ryu, Y. H., Smith, J.A., Bou-Zeid, E., & Baeck, M.L. (2015). The influence of land-surface heterogeneities on heavy convective rainfall in the Baltimore-Washington metropolitan area. *Monthly Weather Review*, Accepted, doi: 10.1175/MWR-D-15-0192.1

Safeeq, M., and Fares, A. (2011). Accuracy evaluation of ClimGen weather generator and daily to hourly disaggregation methods in tropical conditions. *Theoretical and Applied Climatology*, 106(3), 321-341. doi:10.1007/s00704-011-0438-4

Salameh, T., Drobinski, P., Vrac, M., & Naveau, P. (2009). Statistical downscaling of near-surface wind over complex terrain in southern France. *Meteorology and Atmospheric Physics*, 103 (1), 253-65

Salathé, E. Jr, Steed, R., Mass, C.F., & Wilby, P.H. (2008) A high-resolution climate model for the U.S. Pacific Northwest: Mesoscale feedbacks and local responses to climate change. *J. Clim.*, 21, 5708–5726

Sanchez-Gomez, E., Somot, S., & Mariotti, A. (2009). Future changes in the Mediterranean water budget projected by an ensemble of regional climate models. *Geophysical Research Letters, 36*(21)

Schär, C. (2012). Numerical Modelling of Weather and Climate. http://www.iac.ethz.ch/edu/courses/master/modules/numerical_modelling_of_weather_and_climate

Schroede, J.W. (2004). Corn Silage Management, NDSU Extension Service, publication; AS-1253. Accessed online: https://www.ag.ndsu.edu/pubs/ansci/dairy/as1253.pdf

Schulzweida, U., Kornblüh, L., & Quast, R., (2009). Climate Data Operators version 1.3.2; available at http://www.mpimet.mpg.de/cdo

Seneviratne, S.I., Donat, M., Mueller, B., & Alexander, L.V. (2014). No pause in the increase of hot temperature extremes. *Nature Climate Change*, 4, 161-163

Shaban, A. (2011). Analyzing Climatic and Hydrologic Trends in Lebanon. *Journal of Environmental Science and Engineering*, 5, 483-492

Shah, S., and Bou-Zeid, E. (2014). Direct Numerical Simulations of Turbulent Ekman Layers with Increasing Static Stability: Modifications to the Bulk Structure and Second-Order Statistics. *The Journal of Fluid Mechanics*, 760, 494-539, doi: 10.1017/jfm.2014.597

Skamarock, W.C., and coauthors. (2008). A description of the Advanced Research WRF version 3, NCAR Tech. Note, NCAR/TN-475 + STR. 125pp., Natl. Cent. for Atmos. Res., Boulder, Colorado

Smith, R.B., and Barstad, I. (2004). A linear theory of orographic precipitation. *J Atmos. Sci.*, 61(12), 1377–1391

Singh, A. K., Goyal, V., Mishra, A. K., & Parihar, S. S. (2013). Validation of CropSyst simulation model for direct seeded rice–wheat cropping system. *Curr. Sci*, 104(10), 1324-1331

Smith, S. J., and Wigley, T. M. L. (2006). Multi-gas forcing stabilization with Minicam. *Energy Journal*, 373-391

Soares, P.M.M., Cardoso, R.M., Miranda, P.M.A., de Medeiros, J., Belo-Pereira, M., & Espirito-Santo, F. (2012). WRF high resolution dynamical downscaling of ERA-Interim for Portugal. *Clim Dyn*, 39,2497–2522, doi: 10.1007/s00382-012-1315-2

Sommer, R., Wall, P. C., & Govaerts, B. (2007). Model-based assessment of maize cropping under conventional and conservation agriculture in highland Mexico. *Soil and Tillage Research*, 94(1), 83-100

Souch, C., and Grimmond, C.S.B. (2004). Applied climatology: 'heat waves'. *Progress in Physical Geography*, 28(4), 599–606

Stockdale, T N. (1997). Coupled ocean atmosphere forecasts in the presence of climate drift. *Mon. Wea. Rev*., 125, 809-818.

Stockdale T. N., Anderson, D. L. T., Alves, J. O. S, & Balmaseda, M. A. (1998). Global seasonal rainfall forecasts using a coupled ocean-atmosphere model. *Nature*, 392, 370-373.

Stockdale, T. N., Anderson, D. L. T., Balmaseda, M. A., Doblas-Reyes, F., et al. (2011). ECMWF seasonal forecast system 3 and its prediction of sea surface temperature. *Clim. Dyn*. doi 10.1007/s00382-010-0947-3

Stöckle, C. O., Donatelli, M., & Nelson, R. (2003). CropSyst, a cropping systems simulation model. *European Journal of Agronomy*, 18(3), 289-307. doi:10.1016/S1161-0301(02)00109-0

Stöckle, C., Kemanian, A., Nelson, R., Adam, J., Sommer, R., & Carlson, B. (2014). CropSyst model evolution: From field to regional to global scales and from research to decision support systems. *Environmental Modelling & Software*, 62, 361-369. doi:10.1016/j.envsoft.2014.09.006

Stöckle, C. O., Martin, S. A., & Campbell, G. S. (1994). CropSyst, a cropping systems simulation model: Water/nitrogen budgets and crop yield. *Agricultural Systems*, 46(3), 335-359. doi:http://dx.doi.org/10.1016/0308-521X(94)90006-2

Stöckle, C. O., and Nelson, R. (2003). CropSyst's User Manual. Agric. Engineering Dept., Washington State University, Pullman, WA

Sun, Y., Solomon, S., Dai, A., & Portmann, R.W. (2007) How often will it rain? *J Clim*, 20, 4801–4818, doi: 10.1175/JCLI4263.1

Talbot, C., Bou-Zeid, E., & Smith, J. (2012). Nested mesoscale large-eddy simulations with WRF: Performance in real test cases. *Journal of Hydrometeorology*, 13(5), 1421-1441, doi: 10.1175/JHM-D-11-048.1

Tang, Z.Y., and Fang, J.Y. (2006). Temperature variation along the northern and southern slopes of Mt. Taibai, China. *Agric. For. Meteorol*., 139(3–4), 200–207, doi:10.1016/j.agrformet.2006.07.001

Tanner, C.B., and Sinclair, T.R. (1983). Efficient water use in crop production: research or re-search? In: Taylor, H.M., Jordan, W.R., Sinclair, T.R. (Eds.), Limitations to Efficient Water Use in Crop Production. Am. Soc. Agron. Crop Sci. Soc. and Soil Sci. Soc. Am., Madison, WI, USA, p. 154

Taplin, R. (2012). People, policy and politics in future climates. In A. Henderson-Sellers, & K. McGuffie (Eds.), The future of the world's climate (second edition) (pp. 29-46). Boston: Elsevier. doi:http://dx.doi.org/10.1016/B978-0-12-386917-3.00002-6

Tatsch, J. D., and Bindi, M. (2009). A preliminary evaluation of the CropSyst model for sugarcane in the Southeast of Brazil. *Impact of Climate Change on Agricultural and Natural Ecosystems*, 50, 75

Taylor, K.E., Stouffer, R.J., & Meehl, G.A. (2012). An overview of CMIP5 and the experiment design. *Bull. Am. Meteorol. Soc.*, 93, 485–498, doi: 10.1175/BAMS-D-11-00094.1

The World Bank. (2012). Turn Down the Heat: Why a 4°C Warmer World Must Be Avoided. www.worldbank.org

Tingem, M., Rivington, M., & Bellocchi, G. (2009a). Adaptation assessments for crop production in response to climate change in Cameroon. *Agronomy for Sustainable Development*, 29(2), 247-256. doi:10.1051/agro:2008053

Tingem, M., Rivington, M., Bellocchi, G., & Colls, J. (2009b). Crop yield model validation for Cameroon. *Theoretical and Applied Climatology*, 96(3), 275-280. doi:10.1007/s00704-008-0030-8

Torriani, D., Calanca, P., Lips, M., Ammann, H., Beniston, M., & Fuhrer, J. (2007a). Regional assessment of climate change impacts on maize productivity and associated production risk in Switzerland. *Regional Environmental Change*, 7(4), 209-221. doi:10.1007/s10113-007-0039-z

Torriani, D., Calanca, P., Schmid, S., Beniston, M., & Fuhrer, J. (2007b). Potential effects of changes in mean climate and climate variability on the yield of winter and spring crops in Switzerland. *Climate Research*, 34(1), 59-69. doi:10.3354/cr034059

Trapero, L., Bech, J., Lorente, J. (2013). Numerical modelling of heavy precipitation events over Eastern Pyrenees: Analysis of orographic effects. *Atmos. Res.*, 123, 368–383. doi:10.1016/j.atmosres.2012.09.014

Tubiello, F. N., Donatelli, M., Rosenzweig, C., & Stöckle, C. O. (2000). Effects of climate change and elevated CO2 on cropping systems: Model predictions at two Italian locations. *European Journal of Agronomy*, 13(2-3), 179-189. doi: 10.1016/S1161-0301(00)00073-3

Tubiello, F., Rosenzweig, C., Goldberg, R., Jagtap, S., & Jones, J. (2002). Effects of climate change on US crop production: Simulation results using two different GCM scenarios. Part I: Wheat, potato, maize, and citrus. *Climate Research*, 20, 259-270. doi:10.3354/cr020259

Tursilowati, L., Sumantyo, J.T.S., Kuze, H., & Adiningsih, E.S. (2012). The integrated WRF/urban modeling system and its application to monitoring Urban Heat Island in Jakarta, Indonesia. *Journal of Urban and Environmental Engineering*, 6(1), 1-9, doi: 10.4090/juee.2012.v6n1.001009

UNDP/GEF and MPWT/DGU. (2005). Climatic zoning for building in Lebanon. Republic of Lebanon, Ministry of Public Works and Transport, General Directorate of Urban Planning

Vialard, J., F. Vitart, M.A. Balmaseda, T.N. Stockdale & D.L. (2005). An ensemble generation method for seasonal forecasting with an ocean-atmosphere coupled model. *Mon. Wea. Rev*., 133, 441-453.

Vigaud, N., Roucou, P., Fontaine, B., Sijikumar, S., & Tyteca, S. (2011). WRF/ARPEGE-CLIMAT simulated climate trends over West Africa. *Climate Dynamics*, 36(5-6), 925-944, doi: 10.1007/s00382-009-0707-4

Volodin, E.M., Dianskii, N.A., & Gusev, A.V. (2010) Simulating present-day climate with the INMCM4.0 coupled model of the atmospheric and oceanic general circulations. *Izvestiya Atmos. Ocean. Phys*., 46, 414–431, doi: 10.1134/S000143381004002X

Wagner, S., Berg, P., Schädler, G., & Kunstmann, H. (2013). High resolution regional climate model simulations for Germany: Part II-projected climate changes. *Climate Dynamics*, 40(1-2), 415-427, doi: 10.1007/s00382-012-1510-1

Wang, Y., Leung, L.R., McGregor, J.L., Lee, D., Wang, W., Ding, Y., & Kimura, F. (2004). Regional climate modeling: Progress, challenges, and prospects. *Journal of the Meteorological Society of Japan*, 82(6), 1599-1628

Waongo, M., Laux, P., and Kunstmann, H. (2015). Adaptation to climate change: The impacts of optimized planting dates on attainable maize yields under rainfed conditions in Burkina Faso. *Agricultural and Forest Meteorology*, 205, 23-39, ISSN 0168-1923, http://dx.doi.org/10.1016/j.agrformet.2015.02.006

Warrach-Sagi, K., Schwitalla, T., Wulfmeyer, V., & Bauer, H. (2013). Evaluation of a climate simulation in Europe based on the WRF-NOAH model system: Precipitation in Germany. *Climate Dynamics*, 41(3-4), 755-774, doi: 10.1007/s00382-013-1727-7

Weiß, M., Floerke, M., Menzel, L., & Alcamo, J. (2007). Model-based scenarios of Mediterranean droughts. *Adv. Geosci., 12,* 145–151

Wheaton, H., Martz, F., Meinershagen, F., & Sewell, H. (1993). Corn silage, G4590. Accessed online: http://extension.missouri.edu/publications/DisplayPrinterFriendlyPub.aspx?P=G4590

White, R., and Toumi, R., 2012. A tightly bound soil-water scheme within an atmosphere-land-surface model. *Journal of Hydrology*, 452-453, 51-63, http://dx.doi.org/10.1016/j.jhydrol.2012.05.028

Wi, S., Dominguez, F., Durcik, M., Valdes, J., Diaz, H.F., & Castro, C.L. (2012). Climate change projection of snowfall in the Colorado River basin using dynamical downscaling. *Water Resources Research*, 48(5), W05504, doi: 10.1029/2011WR010674

Wilby, R.L., Wigley, T.M.L., Conway, D., Jones, P.D., Hewitson, B.C., Main, J., & Wilks, D.S. (1998) Statistical downscaling of general circulation model output: A comparison of methods. *Water Resources Research*, 34(11), 2995-3008

Willmott, C.J. (1982). Some comments on the evaluation of model performance. *Bulletin - American Meteorological Society*, 63 (11), 1309-1313

Wise, M., Calvin, K., Thomson, A., Clarke, L., Bond-Lamberty, B., Sands, R., & Edmonds, J. (2009). Implications of limiting CO_2 concentrations for land use and energy. *Science*, 324(5931), 1183-1186

Xu, J., and Powell Jr., A.M., 2012. Dynamical downscaling precipitation over southwest Asia: Impacts of radiance data assimilation on the forecasts of the WRF-ARW model. *Atmospheric Research*, 111, 90-103, doi:10.1016/j.atmosres.2012.03.005

Yang, B., Zhang, Y., & Qian, Y. (2012). Simulation of urban climate with high-resolution WRF model: A case study in Nanjing, China. *Asia-Pacific Journal of Atmospheric Sciences*, 48(3), 227-241, doi: 10.1007/s13143-012-0023-5

Yau, S. K., and Ryan, J. (2013). Differential impacts of climate variability on yields of rainfed barley and legumes in semi-arid Mediterranean conditions. *Archives of Agronomy and Soil Science*, 59(12), 1659-1674

Yeung, J.K., Smith, J.A., Villarini, G., Ntelekos, A.A., Baeck, M.L., & Krajewski, W.F. (2011). Analyses of the warm season rainfall climatology of the northeastern US using regional climate model simulations and radar rainfall fields. *Advances in Water Resources*, 34(2), 184-204, doi:10.1016/j.advwatres.2010.10.005

Yukimoto, S., Yoshimura, H., Hosaka, M. et al. (2011). Meteorological Research Institute-Earth System Model v1 (MRI-ESM1)—Model Description. Technical Report of MRI. Ibaraki, Japan, pp. 88

Zhang, Y., Dulière, V., Mote, P.W., & Salathé, E.P. (2009). Evaluation of WRF and HadRM mesoscale climate simulations over the U.S. Pacific Northwest. *Journal of Climate*, 22(20), 5511-5526, doi: 10.1175/2009JCLI2875.1

Zhang, Y., Qian, Y., Dulière, V., Salathé Jr., E.P., & Ruby Leung, L. (2012). ENSO anomalies over the Western United States: present and future patterns in regional climate simulations. *Climatic Change*, 110, 315–346, doi: 10.1007/s10584-011-0088-7

Zhao, M., Held, I.M., Lin, S.J., & Vecchi, G.A. (2009a). Simulations of global hurricane climatology, interannual variability, and response to global warming using a 50km resolution GCM. *Journal of Climate*, 22, 6653-6678

Zhao, M., and Held, I.M. (2010), An analysis of the effect of global warming on the intensity of Atlantic hurricanes using a GCM with statistical refinement. *Journal of Climate*, 23(23), 6382-6393. doi: 10.1175/2010JCLI3837.1

Zhao, M., Held, I.M., & Vecchi, G.A. (2010). Retrospective forecasts of the hurricane season using a global atmospheric model assuming persistence of SST anomalies. *Mon. Wea. Rev.*, 138, 3858–3868, doi: 10.1175/2010MWR3366.1

Zhao, Q., Liu, Z., Ye, B., Qin, Y., Wei, Z., & Fang, S. (2009b). A snowmelt runoff forecasting model coupling WRF and DHSVM. *Hydrology and Earth System Sciences*, 13(10), 1897-1906, doi: 10.5194/hess-13-1897-2009